UNIVERSITÄT BAYREUTH

Lehrstuhl für Kristallographie

Crystal Structures of Perovskite-related $Ca_n(Nb,Ti)_nO_{3n+2}$ ($n = 5$ and 6)

Von der Universität Bayreuth zur Erlangung der Würde eines Doktors der Naturwissenschaften (Dr. rer. nat.) genehmigte Abhandlung

vorgelegt von Jonathan S. Guevarra
geboren am 22. März 1970 in Sta.Cruz, Laguna, Philippinen

1. Gutachter: Prof. Dr. Sander van Smaalen
2. Gutachter: Prof. Dr. Hans Braun

Tag der Einreichung: 3. Februar 2006
Tag des Kolloquiums: 22. März 2006

Contents

1 Introduction **7**

Publication Notes 11

2 Single-Crystal X-ray Diffraction **13**

2.1 Experiment with MACH3-Nonius Diffractometer 15

2.1.1 Crystal Preparation 15

2.1.2 Crystal Testing 16

2.1.3 Lattice Parameter Determination 18

2.2 Synchrotron Experiment with CCD Detector 20

2.2.1 Diffractometer and CCD Detector at Hasylab 20

2.2.2 Data Collection using SMART 21

2.3 Experiment with MAR345 IP 24

3 Superspace Crystallography **27**

3.1 Perovskite-related Materials 27

3.2 Introduction to the Superspace Theory 30

3.2.1 Aperiodic Crystals 30

3.2.2 Reciprocal Lattice in Superspace 31

3.2.3 Atoms in Superspace 32

4 Data Processing of CCD and IP Data **37**

4.1 Treatment of CCD Data 37

4.1.1 Analyzing the Reflections 37

4.1.2 Indexing and Finding the Orientation Matrix 39

4.1.3 Data Reduction 43

4.1.4 Absorption Correction 47

4.2 Treatment of Image Plate Data 49
4.2.1 Crystal Shape Optimization and Absorption Correction 52

5 Crystal Structure of $Ca_5Nb_5O_{17}$ 55
5.1 Introduction 55
5.2 Experimental 57
5.3 Discussion 62
5.4 Conclusions 71

6 Perovskite-related $Ca(Nb,Ti)O_{3.33}$ 73
6.1 Introduction 73
6.2 Experimental 75
6.3 Discussion 79
6.4 Conclusions 85

7 Crystal Structure of Perovskite-related $Ca_5Nb_4TiO_{17}$ 87
7.1 Comment 87
7.2 Experimental 92

8 Superspace Description 95
8.1 Introduction 96
8.2 Experimental 97
8.2.1 The Layer Model 97
8.2.2 Supercell Refinements 100
8.2.3 Superspace Refinements 102
8.3 Discussion 105
8.3.1 Validation of the Superspace Refinements 105
8.3.2 Modulation Functions 107
8.4 Conclusions 110

9 Conclusions 113

10 Zusammenfassung 119

A Sample Output of SMART 125

B Sample Output of SAINT 127

C Sample Output of SADABS **133**

D Sample Output of CRYSALIS RED **137**

E Supplementary Materials for $Ca(Nb,Ti)O_{3.33}$ **141**

F Supplementary Materials for $Ca_5Nb_4TiO_{17}$ **145**

G Supplementaries for Superspace Refinements **147**

Bibliography **161**

List of Figures **165**

List of Tables **168**

Acknowledgements **169**

Erklärung **171**

Chapter 1

Introduction

Compounds of the homologous series $A_nB_nO_{3n+2}$ are a special group of perovskite-related layered materials. They comprise oxide materials with interesting physical and electronic properties (Lichtenberg et al.; 2001). The crystal structures of these compounds are derived from the ABO_3 perovskite-type structure, with a stacking of slabs of vertex-sharing BO_6 octahedra alternating with layers of additional oxygen (Fig. 1.1). The crystal structures can be characterized by the parameter n which describes the width of the slabs measured in the numbers of BO_6 octahedra, and which determines the oxygen content. Different electronic characteristics may be obtained by appropriate substitutions at the A or B site. In this thesis the crystal structures of the compounds of the series $A_nB_nO_{3n+2}$ where A = Ca and B = Nb or Ti with $n = 5$ and 6 are reported. Although the topologies of these compounds have been known for a long time (Nanot et al.; 1979), precise atomic coordinates are required for a meaningful crystal chemical analysis. Using single-crystal X-ray diffraction, the accurate crystal structures of these compounds have been obtained. The results give quantitatively correct information about bond distances and bond angles. This provides insight in the deformation and tilting of the BO_6 octahedra at the different parts of the octahedral slabs which helps improve the understanding of the structural and physical properties of these compounds. This thesis also presents an alternative description of the crystal structures of these compounds employing the superspace framework. Recently, superspace has been applied successfully in the structural description of a family of compounds exhibiting compositional changes (Elcoro et al.; 2000, 2001, 2004). This superspace approach makes use of a modulated-layer structure model, consisting of discontinuous atomic domains given by occupational crenel

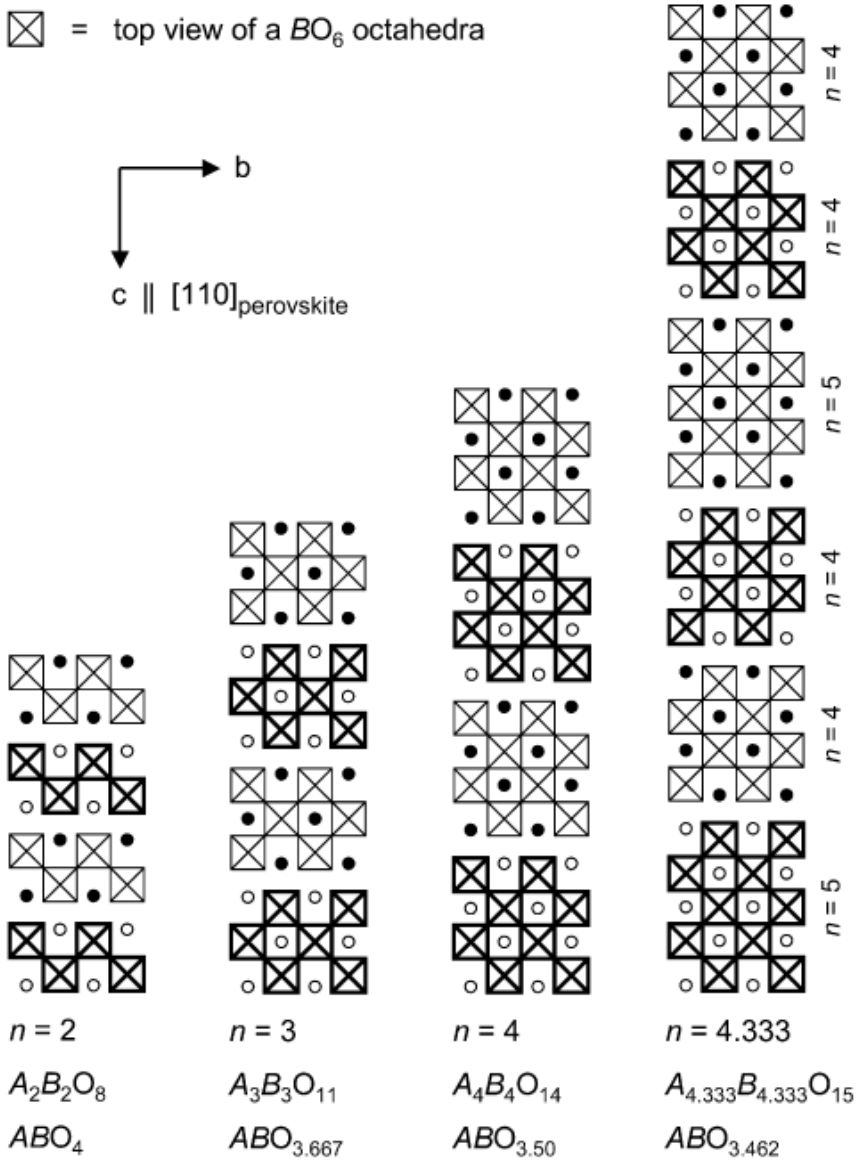

Figure 1.1: Sketch of the idealized, non-distorted crystal structure of the $n = 2, 3, 4$ and 4.33 members of the perovskite-related layers $A_nB_nO_{3n+2}$ projected along the **a**-axis. Circles represent the A cations. Light and heavy drawing of the BO_6 octahedra indicates a height difference perpendicular to the drawing plane of about one-half the octahedron body diagonal. Filled and open circles indicate A cations also differing in height by this distance perpendicular to the drawing plane. (Lichtenberg et al.; 2001)

functions. A major feature of this approach is that the crystal structures of any composition within a particular family of compounds can be described by a common superspace model while the primary modulation wave vector and the width of the atomic domains vary systematically with composition. Moreover, as the atomic displacement parameters of most atomic domains do not require modulation, structure refinements could be carried out using a smaller number of parameters than are required in the three-dimensional (3D) case. In the present work, the superspace approach has been applied to describe in a unified way the crystal structures of the $n = 5$ and $n = 6$ members of the family of compounds $Ca_n(Nb,Ti)_nO_{3n+2}$. The structure refinements for these compounds have been presented and compared with three-dimensional refinements in an effort to establish the validity and efficiency of the superspace approach.

All structure investigations were carried out using single-crystal X-ray diffraction (XRD). Single-crystal XRD has been favored over powder diffraction for more accurate structure solution because of its superior signal-to-noise ratio and higher resolution to measure different Bragg reflections. The experiments either make use of synchrotron radiation with a CCD area detector or they employ Mo-Kα radiation of a rotating anode generator with an Image Plate detector. In Chapter 2, the single-crystal XRD procedures used in the thesis are presented. The measurements including determination of lattice parameters using a Nonius MACH3 diffractometer with point detector are discussed. Because area detectors were vastly used in the data collection, corresponding discussions on measurements with different area detectors are also included. The experimental details are presented of the measurements with a MAR345 Image Plate (IP) diffractometer at the Laboratory of Crystallography in Bayreuth, and of the measurements with a CCD area detector at the synchrotron facility of Hasylab at DESY, Hamburg.

Chapter 3 presents a discussion on the topologies and crystal structures of perovskites and perovskite-related layered materials, which include the compounds investigated. The fundamental concepts of superspace crystallography are introduced to pave the way for the description of the superspace approach that has been applied in the structural description of these compounds. The application of superspace has been very effective in the structural characterization of aperiodic crystals which exhibit long-range order without 3D periodicity. Incommensurately modulated crystals, which have basic structures with 3D periodicity but which are modulated by

a wave function with a periodicity incommensurate with that of the basic structure, have benefited mostly from the superspace formalism. In this thesis, however, only commensurately modulated crystals were investigated. Within the superspace framework, the crystal structures of different compositions of $Ca_n(Nb,Ti)_nO_{3n+2}$ with $n = 5$ or 6 are described in terms of a modulated layered model using a unique superspace group.

In Chapter 4, the details of data reduction of IP data and CCD data are presented including the procedures for finding the orientation matrix and integrating the diffracted intensities. Absorption corrections are discussed including crystal shape optimization which was also applied for numerical absorption correction.

Chapter 5 reports the crystal structure of $Ca_5Nb_5O_{17}$ ($n = 5$). Using synchrotron radiation with a CCD detector, the crystal structure of this compound at room temperature was found to be monoclinic, $P2_1/c$, with the existence of pseudo-merohedrally twinning. Computed bond distances and angles reveal the variation of the distortion of NbO_6 octahedra at different parts of the slabs. Bond-valence sums (Brese and O'Keeffe; 1991) computed for different Nb sites in the slabs provide useful information about the electrical conductivity at different parts of the slabs.

Chapter 6 reports the crystal structure of perovskite-related $Ca(Nb,Ti)O_{3.33}$ ($n = 6$). The crystal structure of this compound at room temperature was determined using synchrotron radiation with a CCD detector. The crystal structure was found to be acentric, $P2_1$, and it is pseudo-merohedrally twinned. In Chapter 7, the crystal structure of $Ca_5Nb_4TiO_{17}$ ($n = 5$) is reported. This compound crystallized in the space group $P2_1/c$, and it is also pseudo-merohedrally twinned. Data collection was facilitated using a MAR345 Image Plate detector. In both Chapters 6 and 7, bond distances and angles were computed and reveal variation of the extent of NbO_6 deformation with the different sites in the slabs. Bond-valence sums (Brese and O'Keeffe; 1991) also reveal partial ordering of the Nb^{5+} and Ti^{4+} at different (Nb,Ti) sites in the slabs.

In Chapter 8 the superspace approach as applied to describing the crystal structures of perovskite-related compounds is introduced. Its validity and efficiency is demonstrated by structure refinements in (3+1)-dimensional space for the Ti-doped compounds $Ca_5Nb_4TiO_{17}$ ($n = 5$) and $Ca_6(Nb,Ti,)_6O_{20}$ ($n = 6$) and by comparing with the 3D refinements. The atomic displacive modulation parameters for the two compounds are compared to find out whether or not common modulation functions

can be used to describe the deviations of the atoms from their average positions. This provides a better understanding of the extent of the validity of the superspace approach as applied to different members of a homologous compound series.

Publications

Parts of this thesis have been published or have been submitted/ in preparation for publication in the international scientific literature.

Chapter 5, published in:
Guevarra, J., van Smaalen, S., Rotiroti, N., Paulmann, C. and Lichtenberg, F. (2005). Crystal structure of $Ca_5Nb_5O_{17}$, *Journal of Solid Sate Chemistry* **178**, 2934–2941.

Chapter 6, published in:
Guevarra, J., van Smaalen, S., Daniels, P., Rotiroti, N. and Lichtenberg, F. (2005). Perovskite-related Ca(Nb,Ti)$O_{3.33}$, *Zeitschrift für Kristallographie* **220**, 19–24.

Chapter 7, submitted as:
Guevarra, J., van Smaalen, S. and Lichtenberg, F. (2006). Crystal structure of perovskite-related $Ca_5Nb_4TiO_{17}$. Submitted to *Acta Crystallographica C.*

Chapter 8, in preparation:
Guevarra, J., van Smaalen, S. and Schönleber, A. (2006). Superspace Description of the Crystal Structures of $Ca_n(Nb,Ti)_nO_{3n+2}$ ($n = 5$ and 6). In preparation, to be submitted to *Acta Crystallographica B.*

Chapter 2

Single-Crystal X-ray Diffraction

Single-crystal X-ray diffraction (XRD) has evolved into a powerful tool in crystal structure analysis. It has been widely used for accurate crystal structure determination of a vast number of inorganic and organic compounds, because it provides a higher resolution and much better signal-to-noise ratio than powder diffraction. Experiments involving single-crystal XRD may be considered as indirect measurements of the structure factors from measurements of integrated intensities of Bragg reflections on single crystals. The experimental task for determining the crystal structure mainly consists of measuring the amplitudes of the set of structure factors. The latter are given by (Giacovazzo et al.; 2002):

$$F(\mathbf{H}) = \sum_{j=1}^{N} f_{oj}\left(\frac{\sin(\theta)}{\lambda}\right) \exp\left(-\frac{8\pi^2 U_j \sin^2(\theta)}{\lambda^2}\right) \exp\left(2\pi i \mathbf{H}\cdot\mathbf{r}_j\right) \tag{2.1}$$

where $\mathbf{r}_j$ is the position of the jth atom in the unit cell, and $f_{oj}\left(\frac{\sin(\theta)}{\lambda}\right)$ is its atomic scattering factor; N is the number of atoms in the unit cell; the factor $8\pi^2 U_j$ is the atomic temperature factor, and $\mathbf{H}$ is a reciprocal lattice vector. The modulus of the structure factor is related to the experimentally observed intensities:

$$|F(\mathbf{H})| \propto \sqrt{I(\mathbf{H})} \tag{2.2}$$

The relationship between $|F(\mathbf{H})|$ and $I(\mathbf{H})$ depends on a number of factors, primarily geometric, that are related to the individual reflection and to the apparatus used to measure the intensities (Stout and Jensen; 1989). In single-crystal diffractometry, the X-ray photons that are scattered by the crystal are usually captured

by a detector system and thus recorded as diffracted intensity. From a geometrical point of view, two types of detectors can be distinguished and both types were used for the XRD experiments reported in this thesis (Giacovazzo et al.; 2002):

- *Point detectors (or zero-dimensional detectors, or photon counters)* are devices measuring the number of photons per unit time arriving at a point where the detector is situated and returning an electrical signal with a current that is proportional to the incident photon flux. The scattering angle is determined externally by mechanically positioning the counter at pre-set points with respect to the crystallographic reference system, with the use of computer-controlled goniometers.

- *Area detectors or two-dimensional detectors* measure the number of photons arriving per unit time as a function of the position within the detector's surface. Such devices have higher sensitivity and can simultaneously scan a large portion of reciprocal space, which is very convenient when dealing with substances that have large unit cells and therefore require the recording of many reflections. Thus, a much faster data collection and high redundancy of symmetry-equivalent data may be realized. Since the entire reciprocal space is observed, and not just the regions immediately around the reciprocal lattice points, they can be helpful for special purposes like the study of incommensurate structures. Another advantage is that it is not necessary to establish the correct unit cell and crystal orientation matrix before the beginning of the data collection, because these can be found later from the recorded images. A disadvantage is that they require careful corrections for non-uniformity of both spatial response and intensity response of the detectors. Two types of area detectors were used for the experiments that are reported here. They are (Clegg et al.; 2001):

  - *Image Plates (IP).* These devices are essentially storage phosphors that store the image in the form of trapped electron color-centers. These can be subsequently 'read' by stimulation emission with laser light and then erased by strong visible light before another exposure to X-rays. They are usually available in large sizes and therefore have greater capacity to record reflections at a time. They also have high recording efficiency and high spatial resolution. Major disadvantage is the need for a separate

readout process and they are much slower than other electronic area detectors, often taking minutes rather than seconds.

– *Charge-coupled devices (CCD).* These devices are arrays of independent detector elements, each composed of a metal-oxide semiconductor (MOS) structure. A phosphor is fibre-optically coupled to the CCD chip, which is cooled to reduce its inherent electronic noise level due to thermal excitation of the electrons. Electron-hole pairs are generated within the chip by the incident X-rays. Electrons trapped in potential wells are read out as current after completion of the desired exposure time. With its highly efficient recording, high dynamic range and a low noise level, and very short read-out times (measured in seconds), CCDs have the edge over other types of area detector and have the best potential for further development.

Preparation and testing of single crystals investigated in this thesis were carried out using a MACH3 diffractometer with point detector. Data collections were performed using synchrotron radiation with a CCD detector and using a MAR345 IP diffractometer with a rotating anode generator with Mo-Kα radiation. The experimental procedures involved in these measurements are described in the following sections.

2.1 Experiment with MACH3-Nonius Diffractometer

2.1.1 Crystal Preparation

In this thesis, several single crystals of the compounds investigated were prepared by breaking them off larger aggregates of sample material. Because of the fragile nature of the structure, preparation of good single crystals is not without problem. Owing to the layered structure of the compounds, the crystals show perfect cleavage perpendicular to the $\mathbf{c}^*$ axis, leading to the production of extremely thin plates. They were visually inspected under a microscope and the single crystals selected measure no larger than 150 μm. Before mounting the crystal, the glass fiber which holds the crystal is fastened to a brass pin with sealing wax and its tip is allowed

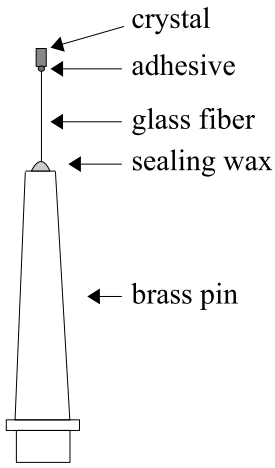

Figure 2.1: Sketch of a mounted single crystal

to protrude about 4 mm above the pin. The glass fiber is very fine (about 50 μm in diameter) and its tip is dipped into a two-component adhesive. The tip must not contain too much adhesive as this might 'flood' the crystal when the crystal is attached to it. One should avoid to 'coat' the crystal with adhesive as this might cause problems with the absorption of X-rays. Using a microscope, the crystal is mounted to the tip of the fiber such that the plane of the plate-like crystal is parallel to the fiber axis and to a well-defined edge of the crystal if possible (Fig. 2.1).

2.1.2 Crystal Testing

The mounted crystals were subsequently tested for their quality using the Nonius MACH3 diffractometer. The good crystals that were selected for data collection were measured with the same diffractometer to determine the lattice parameters more accurately. The MACH3 diffractometer is a four-circle diffractometer in κ-geometry. It is equipped with a point detector and a rotating-anode generator with Molybdenum target. Fig. 2.2 shows the MACH3 single-crystal diffractometer used at the Laboratory of Crystallography in Bayreuth. The κ-goniometer system carries the goniometer head and keeps the crystal at the center of the diffractometer throughout the measurement. The suspension provided by the MACH3 diffractometer gives enhanced flexibility over the traditional Eulerian cradle while simultaneously diminishing drastically the obscuration caused by the mount for the χ circle.

Testing of single-crystals is commenced with the automatic program routine

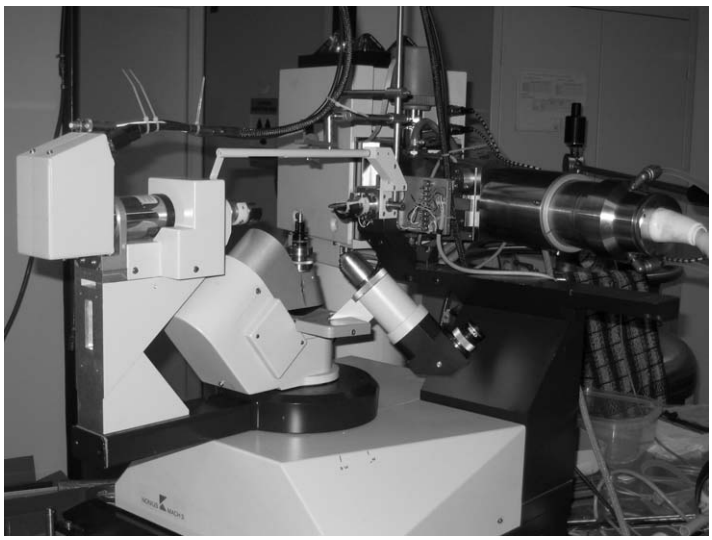

Figure 2.2: Nonius Kappa MACH3 single-crystal diffractometer at the Laboratory of Crystallography, Bayreuth, Germany

SEARCH which scans through the reciprocal space in a systematic manner to hunt and center reflections. In normal mode, a starting point in 2θ, χ and a ϕ range are specified where χ is physically limited to $\pm 100°$. A spiral around the starting values of θ and χ is stepped through where at each point the specified ϕ range is scanned. For the reported measurements, theta values of 10° and 12° were found suitable to quickly find reflections. This choice is a compromise between speed of the hunting procedure and correctness of the unit-cell parameters resulting after SEARCH (Enraf-Nonius; 1989). The scan speed and discrimination factor for peak/background discrimination are specified at the start of the SEARCH routine. One can select a speed of the ϕ-scan in the range from 1×16.48 to 12×16.48 degrees/min. Normally, a speed of 12 is used. Lower speeds can be used to search for weakly diffracting crystals. A value of 2 is usually suitable for the discrimination factor. A proper value in case of low background is 1. Higher values will decrease the sensitivity but will reduce the time spent in trying to center diffuse, weak or noisy peaks. The setting angles of the reflections found are stored in a 'crystal file'. A total of 25 reflections may be stored in the file although one may interrupt the search routine once a sufficient number of reflections have been found to find a suitable orientation matrix.

After an appropriate number of reflections has been found, the INDEX routine

produces a primitive unit cell, an orientation matrix and assigns indices to the reflections in the list. It requires at least three accurately centered reflections. In practice, seven to ten reflections are usually required to obtain an orientation matrix. In the event that the expected unit cell is not the one reported by INDEX, one may transform or reduce the cell and make a new indexing using the matrix transformation routine TRANS. This can be done by either specifying explicitly a matrix of transformation or by making an automatic search of transformations for determining the conventional cell from a reduced cell. Additional routines enable indexing of new reflections in the list or re-indexing (REIND) the entire list based on the current cell and least-squares refinement (LS) of the matrix following the addition of reflections to the list (Enraf-Nonius; 1989).

Once the correct unit cell has been found, one may further examine the reflection profile by making a one-axis or two-axes scan on selected reflections through the current goniometer position. Here, one specifies the type of scan, indices of reflection and the angle ψ about the scattering vector, as well as the number n for scan speed, $16.48/n$ degrees/minute. In this thesis, ω scans and $\omega - \theta$ scans were performed to examine the rocking curve of some reflections (particularly those reflections along the crystallographic axes) and to get an estimate of the full-width at half-maximum (FWHM) of the reflections. The character of the reflection profile, provides information about the qualtity of the crystal. Good-quality crystals normally exhibit sharp reflection profiles (FWHM$< 0.2^\circ$) and have a similar character for different values of ψ (Fig. 2.3). Accurate intensity data require a good-quality crystal. Employing this method, good quality specimens have been found amongst a larger set of crystals with broader reflection profiles.

2.1.3 Lattice Parameter Determination

The reflections stored in the 'crystal file' may be re-centered by another automatic centering routine SETANG to obtain more accurate angles and a better orientation matrix. This procedure should also be performed when new reflections have been added to the original list. SET4 is another centering routine that produces more accurate lattice parameters. The reflections are centered in four orientations: (i) position specified in the crystal file (ii) at $\bar{h}\bar{k}\bar{l}$, (iii) at negative 2θ and (iv) at $\bar{h}\bar{k}\bar{l}$ and negative 2θ. The list of reflections is usually modified to include strong reflections at higher scattering angles (usually $2\theta \geq 20^\circ$) for more accurate determination of lattice

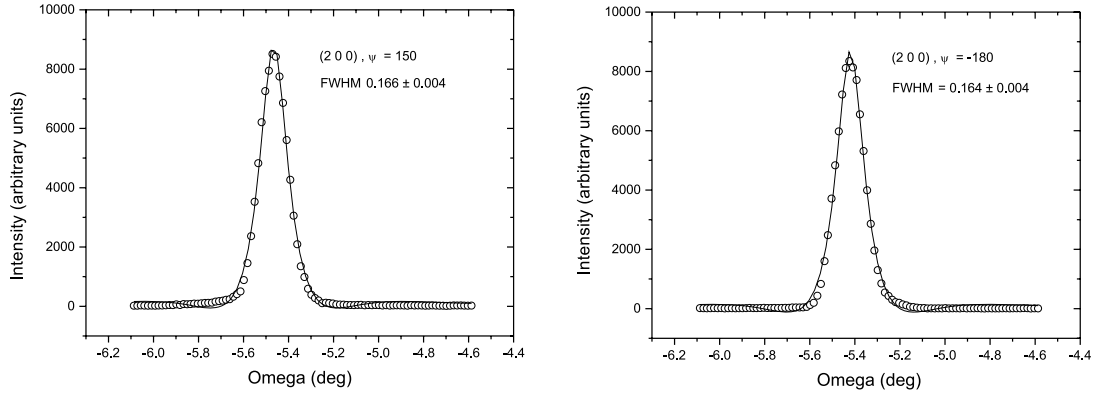

Figure 2.3: Omega scans onf the reflection (2 0 0) of $Ca_5Nb_4TiO_{17}$ ($n = 5$) for two different ψ-values.

parameters. Least-square refinement (LS) is executed after each re-centering routine. Another least-square refinement routine, CELDIM, refines the cell parameters with constraints (e.g. from the lattice type) based on the 2θ values of the reflections. In this thesis, the SET4 routine and CELDIM routine were used to obtain the most accurate lattice parameters of the compounds investigated.

Because of the mosaic spread of the crystal and the large unit cell dimension along the **c**-axis of the compounds investigated, overlap of reflections poses a serious problem for data collection with the CAD4 diffractometer with point detector. This limits the number of useful scans for obtaining integrated intensities from an actual data collection. Moreover, because of the weakness of the superlattice reflections (reflections with h=odd) and the large unit cell of the compounds, the time needed to obtain a complete dataset would be unreasonably long when a point detector would be used. The application of area detectors, such as IPs and CCDs, to record several reflections simultaneously offers much faster data collection. The brilliance and enhanced resolution of synchrotron radiation makes this an ideal tool for detecting weak superlattice reflections. In this thesis, measurements using synchrotron radiation with CCD detector were performed for the compounds $Ca_5Nb_5O_{17}$ ($n = 5$) and $Ca(Nb,Ti)O_{3.33}$ ($n = 6$) while the MAR345 desktop beamline diffractometer with IP was used to measure the compound $Ca_5Nb_4TiO_{17}$ ($n = 5$).

2.2 Synchrotron Experiment with CCD Detector

A synchrotron consists of a large-diameter ring, along which electrons or positrons travel at relativistic speeds. The closed path is enforced by a series of bending magnets. The radiation that is emitted by the charge carriers accelerated in the magnets is not only very intense but it is highly collimated and it is almost completely polarized in the horizontal plane. The radiation emission pattern covers a full range of wavelengths presenting a continuous spectrum. For monochromatic X-ray diffraction, one wavelength is selected by a monochromator, which may also provide some focusing and compression of the beam through its special shape and construction (Clegg et al.; 2001).

2.2.1 Diffractometer and CCD Detector at Hasylab

Single-crystal X-ray diffraction with monochromatic X-rays is one of the many applications of synchrotron radiation that can be performed at beamline F1 of the Hamburger Synchrotronstrahlunglabor (HASYLAB) at the Deutsches Electronen-Synchrotron (DESY) in Hamburg, Germany. The beamline has a Huber 4-circle diffractometer with κ-geometry and it is equipped with a SMART 1000 CCD system at the time the experiments were performed[1](Fig. 2.4). The instrument makes use of a wide-band double-crystal silicon monochromator, Si(111), that allows to select the wavelength between 0.4 Å and 2.5 Å. The CCD detector, which has an effective diameter of 62.5 mm, is mounted on a second detector axis (the first detector axis is the point detector). The SMART system can read images as 512×512 or 1024×1024 pixels. The pixel size in a 512×512 pixel frame is about 120 μm. Reduction of the 1024×1024 image to a 512×512 image is performed by the CCD hardware, and it is referred to as '2×2 binning'. This hardware binning is advantageous since, while 512×512 pixel has four times the area (and thus produces four times the signal) as a 1024×1024, the read noise remains the same, thus providing a signal-to-noise improvement for weak reflections. Data storage space is also four times smaller for 512×512 frames than it is for 1024×1024 frames (Bruker; 1998b). In the measurements performed, the 512×512 pixel frame has been used.

[1]At present, a MARCCD detector is installed in the diffractometer at beamline F1 of Hasylab.

Figure 2.4: Huber Kappa-diffractometer at beamline F1 of Hasylab in DESY, Hamburg, Germany

2.2.2 Data Collection using SMART

Data collection is done automatically by the SMART software (Bruker; 1998b) which reads from a user-defined sequence of runs, each containing information such as the angular settings of the detector and the goniometer, the type of scan (ω or ϕ), scan width, exposure time per frame, and the number of frames to be collected (Fig. 2.5). The wavelength of the radiation is usually pre-determined and is chosen such that the absorption effects are minimized and a reasonable portion of the reciprocal space can be measured. The software XOP (Del Rio and Dejus; 1998) has been used to compute the absorption of each compound as a function of the wavelength of radiation. In the experiments performed in this thesis, a wavelength of 0.7100(2) Å has been used. The type of scan and the number of frames to be collected for each run are usually decided with the help of an interactive graphics program called ASTRO (Bruker; 1998a). This program is useful in the determination of an efficient data collection strategy in order to optimize the data coverage and data redundancy in consideration of the coupled limits of the motors driving the circles of the diffractometer. It uses the Ewald sphere concept to visualize and calculate the volume of data in the scan. High data-redundancy with an extensive set of symmetry-equivalent reflections is necessary for subsequent absorption correction when applying multi-scan absorption correction method such as that which

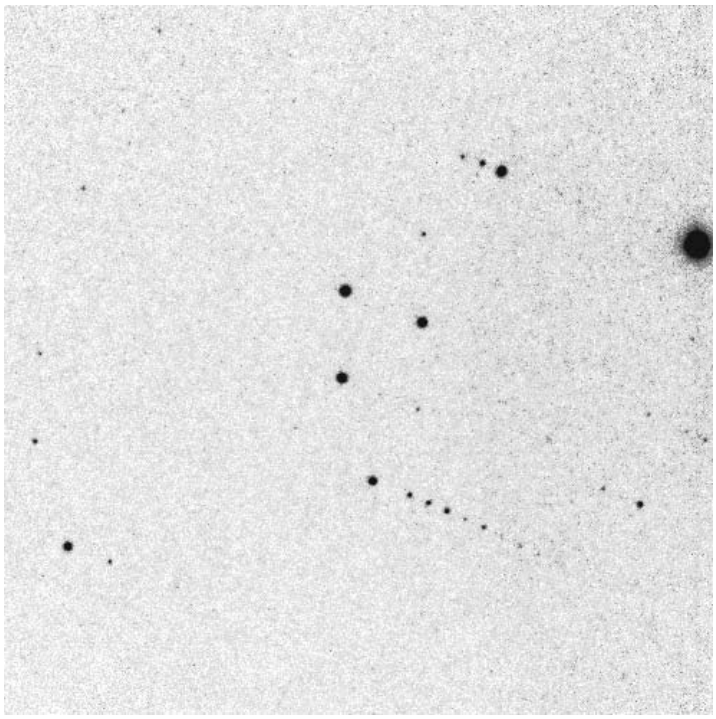

Figure 2.5: X-ray diffraction data on $Ca_5Nb_5O_{17}$ ($n = 5$) recorded using synchrotron radiation ($\lambda = 0.7100(2)$ Å) with a SMART CCD detector. This scan comprises a crystal rotation of 0.1°.

has been implemented in the computer program SADABS (Sheldrick; 2002). The exposure time, scan width and detector distance are normally optimized before the actual data collection, in consideration of the limited beam time available for the measurement. The crystal-to-detector distance is set such that it does not lead to overlap of reflections and allows one to properly resolve neighboring reflections as visualized in the images. Overlap of reflections is a serious problem in the subsequent data reduction. When this occurs, the detector needs to be moved further from the crystal. In the experiments performed a detector distance of 60 mm was sufficient to properly resolve the reflections. In order to record many reflections which are well discernable from background noise, a good exposure time is essential. Exposure time per frame is chosen sufficiently long to illuminate the reflections without overexposing them since overexposed reflections are rendered useless in the subsequent intensity integration. Exposure time depends on the 2θ-offset of the detector with the high-angle measurements requiring a longer irradiation period to

reveal the weak reflections at high Bragg angles. In conjunction with the problem of overlapping reflections, the fine-slicing technique is employed, collecting each image through a very small scan width (0.1° in the measurements conducted). The use of smaller scan widths also minimizes overexposed reflections as only thinner portions of the reflection intensities are recorded on each image.

Because of the decay of the storage ring current in the synchrotron facility, the ring needs to be injected with electrons about every 8 hours. During refill, there is no synchrotron radiation available and the experiment has to be interrupted. After the beam has been restored and the beam has stabilized, the measurement (usually given a different run name) is resumed, with some overlap of frames from the last interrupted measurement. In the subsequent data reduction, these runs which belong to an interrupted measurement are integrated separately. To correct for the decay of the primary-beam intensity during data collection, the computer program SAPRO (Paulmann; 2002) is used. The program writes in the image header the corrected beam count based on an external beam monitor file which contains information about the storage-ring current. This information is read by the computer program SAINT (Bruker; 2000) in the subsequent data reduction and the necessary primary-beam decay correction is applied.

Some corrections necessary when using CCD detectors have to be put in place before starting the actual data collection. These include (Bruker; 1998b):

- *Dark Current Correction* - Even with no light coming onto the CCD chip, the pixels accumulate electrons with time. During data collection, SMART subtracts the dark current image stored in memory from the new diffraction image. This dark current correction also eliminates any fixed bias not compensated for by overscan. The amount of dark current per pixel depends on exposure time, pixel binning, and detector gain. One should therefore either take a new dark current image (or reload one from the disk) whenever one switches to a different frame size, detector gain, or exposure time. The effect is also minimized by cooling the CCD to normal operating temperature (about -50°) before acquiring dark-current correction data.

- *Flood Field Correction* - This is an intensity-uniformity correction applied to the diffraction images because of the variations in the intensity response of the phosphor, fiber optic, and CCD chip as a function of position. The method

involves 'flooding' the entire visible field of the detector with radiation from a point source. A correction table is stored as a standard frame, allowing SMART to make a multiplicative pixel-by-pixel intensity correction as each diffraction image is acquired. Acquiring of a new flood field correction image is only necessary when one switches to different frame size.

- *Spatial Correction* - The demagnification of the diffraction image from the phosphor to the CCD chip via the fiber-optic taper is never perfectly linear. The mapping of the CCD pixels to the original face-plate positions need to be calibrated and a correction applied to every image (Clegg et al.; 2001). A brass-fiducial plate image is usually collected at a specific detector distance and the spatial correction is automatically computed and installed for data collected at the same detector distance. This correction is usually not used until the frames are thresholded prior to autoindexing. It is read in by the data reduction program SAINT (Bruker; 2000) during the integration procedure.

2.3 Experiment with MAR345 IP

As mentioned in Sectioned 2.1, image plate (IP) detectors also offer the possibility of simultaneous measurements of many reflections with sufficiently high accuracy. With improved read-out time, IPs can be very useful for faster data collection. At the Laboratory of Crystallography in the University of Bayreuth in Bayreuth, Germany, a MAR345 desktop beamline diffractometer is installed (Fig. 2.6). It is equipped with a 345 mm MAR345 IP detector with a motorized vertical 2θ arm which can reach up to 30° offset for maximum possible resolution of $d = 0.48$Å for Mo-Kα radiation and $d = 1.04$Å for Cu-Kα radiation. The crystallographic cradle includes a ϕ-circle goniometer with horizontal configuration for crystal orientation and rotation. The diffraction system provides great efficiency of read-out, minimizing the scan-erasure cycle. The X-ray source is a rotating anode generator with either Molybdenum target or Copper target depending on the application. Data collection is automatically carried out using the MAR345 dtb software (Klein; 2004) after defining the experimental parameters for each run. Each run consists of information about the goniometer settings (2θ offset, detector distance, starting ϕ), exposure settings (exposure time, scan width, number of frames) and collimator and beam settings (beam stop distance and slit width)(Fig. 2.7). It is also possible to

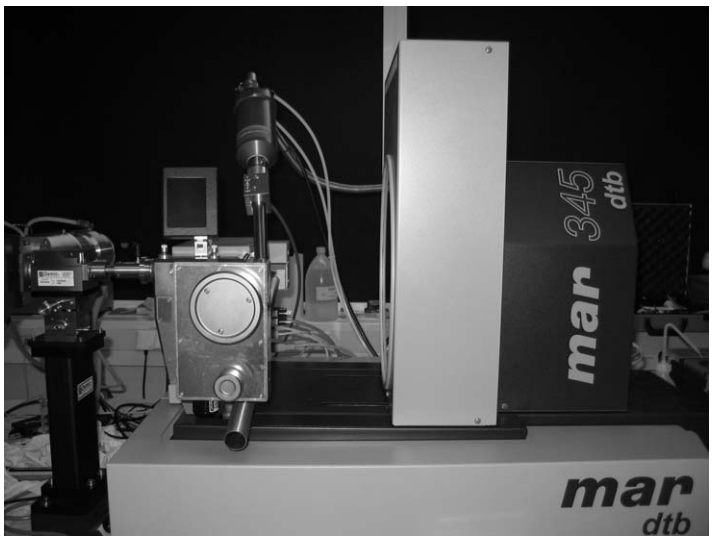

Figure 2.6: Mar345 IP desktop beam line single-crystal diffractometer at the Laboratory of Bayreuth, Bayreuth, Germany

program a batch of runs to proceed automatically during data collection. Exposure times of 1 to 3 minutes were sufficient to illuminate the crystals investigated with minimal overexposure. Diffractometers with rigid ϕ-axis like the MAR345 dtb offer only one degree of freedom for the crystal. In such diffractometers, for a given resolution and orientation of the crystal, not all reflections can be measured, since Bragg law cannot be fulfilled for reflections lying along the axis of rotation. There is a need to re-orient the crystal in order to explore these missed reflections. One may do so by remounting the crystal in another position to the glass fiber before starting the next measurement. It may be difficult to do this procedure especially for 'delicate' crystals with layered structures such as the ones investigated, that reworking the new orientation poses the danger of losing the crystal or it may damage the structure and render the crystal useless. A less risky method of reorienting the crystal is by moving the goniometer head along one of its arcs. The crystal may be brought to the extreme positions of the arc before starting the next measurement. In the measurements performed with MAR345 dtb, the hardware limit of the goniometer used allowed the crystal measured to be moved to $\pm 12^{\circ}$ from the zero position of the gonimeter arc. The same experimental parameters were used for data collection for the other two different orientations of the crystal. The datasets for different crystal orientation were later merged and scaled during data processing.

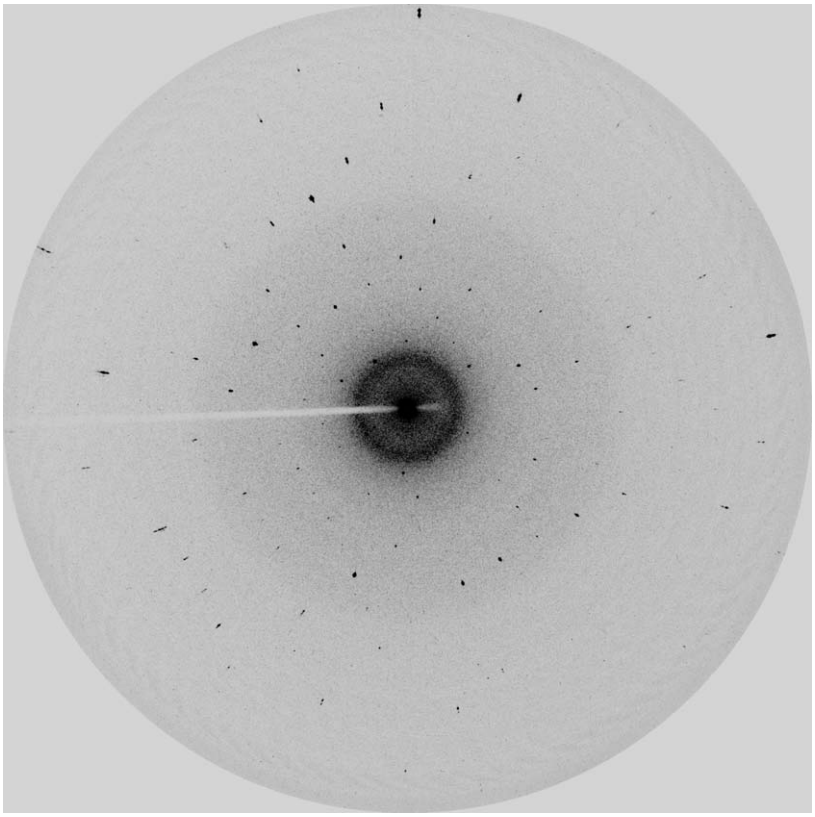

Figure 2.7: X-ray diffraction data on $Ca_5Nb_4TiO_{17}$ ($n = 5$) recorded using Mo-Kα radiation with MAR345 Image Plate Detector. This image comprises 0.3° of crystal rotation.

Chapter 3

Superspace Crystallography

3.1 Perovskite-related Materials

Materials with perovskite-related structures exhibit wide arrays of structural, chemical and physical properties. One of most widely studied compounds belong to the Ruddlesden-Popper series $A_{n+1}B_nO_{3n+1}$. They include the $n = 1$ cuprate $(La,Ba)_2CuO_4$ for which Bednorz and Müller discovered high-T_c superconductivity and the $n = 1$ ruthenate Sr_2RuO_4 which is the first Cu-free superconductor (Lichtenberg et al.; 2001). The crystal structure of these compounds are derived from the ABX_3 perovskites with BX_6 corner-shared octahedra stacked along the [100] direction of the ideal perovskite structure. Another perovskite-related compounds belong to the homologous series $A_nB_nO_{3n+2}$ and is the subject of the present work. The stoichiometry of this series may be written as ABO_X with its corresponding ideal oxygen content $x = 3 + 2/n$. The $A_nB_nO_{3n+2}$ phases possess interesting physical properties. For example, many of the fully oxidized compounds of these series are ferroelectrics with high Curie temperatures, and in some, ferroelectricity is combined with excellent piezoelectric and electrooptic properties (Nanamatsu and Kimura; 1974; Nanamatsu et al.; 1974; Kinase et al.; 1981). Many of the electrically conducting compounds exhibit a quasi-one-dimensional metallic behavior at high temperatures whereas at low temperatures a metal-to-semiconductor transition has been observed (Lichtenberg et al.; 2001; Kuntscher et al.; 2000, 2002, 2004; Weber et al.; 2001). The existence of phases of the $A_nB_nO_{3n+2}$ type was established in the Na-Ca-Nb-O and Ca-La-Ti-O systems by Carpy *et al.* in 1972 (Carpy et al.; 1972).

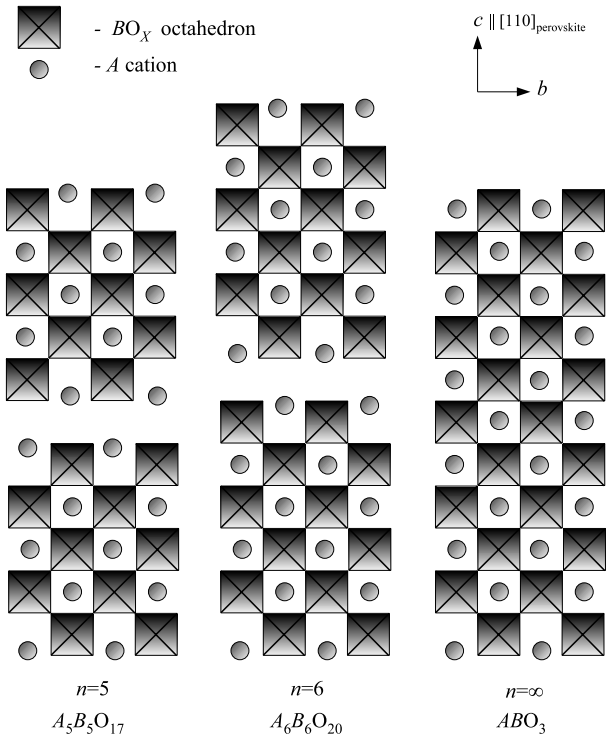

Figure 3.1: Projection along the $[101]_{perovskite}$ of the idealized, non-distorted crystal structures of the $n = 5$, 6 and ∞ members of the perovskite-related layered homologous series $A_nB_nO_{3n+2}$.

Later, related and more detailed studies were reported (Galy and Carpy; 1974). In the following years Nanot *et al.* performed comprehensive crystallographic studies on these compounds and other quarternary niobates and titanates (Nanot et al.; 1974, 1979, 1981, 1983, 1986).

Several compounds have been identified within the homologous series $A_nB_nO_{3n+2}$. The number of observed compounds decreases as the n value increases, and compounds with non-integral n are relatively rare. Different spacegroups have been associated with the crystal structures of these compounds, all of which are either orthorhombic or monoclinic. Compounds with the same value of n but different symmetries correspond to different distortions of the layers relative to the ideal cubic perovskite structure (Levin and Bendersky; 1999). The non-distorted orthorhombic structures of some members of homologous series $A_nB_nO_{3n+2}$ are shown in Fig. 3.1.

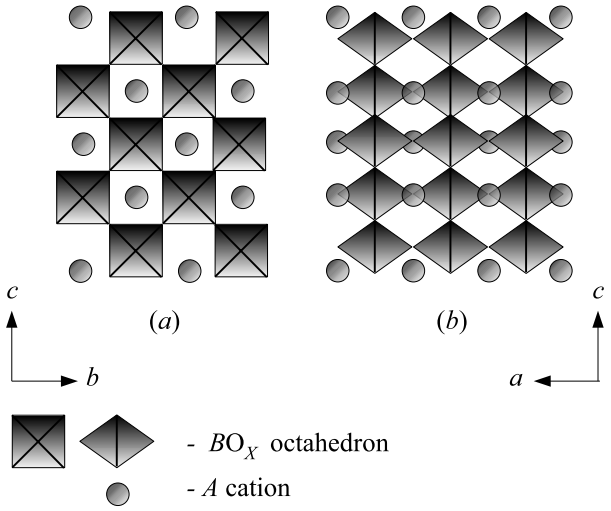

Figure 3.2: Schematic projections of the crystal structures of non-distorted $A_5B_5O_{17}$ along (a) the [100] and (b) the [010] directions.

The compounds have layered structures consisting of corner-shared BO_6 octahedra stacked in slabs along one crystallographic direction which is parallel to the [110] direction of the ideal perovskite-type structure. The slabs are interrupted by a gap such that octahedra on opposite sides of the gap do not share oxygen atoms thus leaving an 'extra' layer of oxygen atoms with respect to the ideal perovskite structure. The width of the slabs increases with n which determines the structure type. For $n = \infty$ the 3D perovskite structure ABO_3 is realized. In structures in which slabs of different width are mixed, n is non-integral and indicates the average number of octahedral layers per slab, e.g., $n = 4.5$ corresponds to alternating slabs of four and five layers wide. Consecutive slabs are displaced from each other by one-half the body diagonal of the octahedron along the [100] direction of the ideal perovskite structure, resulting in an irregular coordination of the A cation. Within the layers, the BO_6 octahedra extend zigzag-like along the **b**-axis and are arranged in chains along the **a**-axis (Fig. 3.2). The lattice parameters of the idealized $A_nB_nO_{3n+2}$ structure can be expressed in the units of the lattice parameter of a cubic perovskite, a_c. If we take the **c**-axis as the stacking direction, we can write the lattice parameters as (Levin and Bendersky; 1999): $a = a_c$, $b = a_c\sqrt{2}$, $c = (n+1)\sqrt{2}a_c$. The interslab region is approximately one octahedron in width.

3.2 Introduction to the Superspace Theory

The compounds investigated in this thesis can be considered as superstructures. Determination of the crystal structure then requires adoption of a corresponding supercell and assignment of an appropriate space group. Alternatively, this may be accomplished by interpreting the crystal structure as a commensurate modulation of a basic structure. Modulations of crystal structures are treated in crystallography within the superspace formalism. To better understand the superspace approach that was employed in the structural characterization of these compounds, a brief introduction to the fundamental concepts of superspace crystallogaphy is given here.

3.2.1 Aperiodic Crystals

The majority of crystals are *periodic* crystals, i.e., they consist of arrangements of atoms with three-dimensional (3D) periodicity or translational symmetry. One consequence of the 3D periodicity is that the scattering vectors of Bragg reflections can be expressed as linear combinations of integer multiples of three independent vectors, the reciprocal basis vectors. There are crystals, however, which lack 3D periodicity but nevertheless exhibit long-range order. As a consequence of long-range order, their diffraction patterns also comprise of sharp Bragg peaks but these cannot be indexed by 3 integers. These crystals, known as *aperiodic* crystals, possess periodic crystal deformations, called *modulations*, associated with density and/or displacive deviations from the undistorted crystal structure called *basic structure*[1]. The true atomic positions are then described by deviations from the lattice-periodic positions. The modulation may be *commensurate* or *incommensurate* depending on whether or not the modulation has an integral multiple of the periodicity of the basic structure. The compounds investigated in this thesis are commensurately modulated. The modulation gives rise to *satellite reflections* in the diffraction patterns (de Wolff; 1974). Satellite reflections are associated with peaks in the diffraction pattern that occur around the so-called *main reflections*. These peaks do not belong to a lattice and cannot be indexed by three integers. This means that the symmetry of aperiodic

[1]The *basic structure* should be distinguished from the *average structure* which refers to the crystal structure averaged over all modulations taking into account only the main reflections without the satellite reflections. The real distorted structure is obtained by structure refinement with respect to the average structure (Janner and Janseen; 1977).

crystals cannot be described by 3D space groups.

3.2.2 Reciprocal Lattice in Superspace

It is still possible, though, to ascribe periodicity to aperiodic crystals by extending the crystallographic description to higher-dimensional space (de Wolff; 1974). In this $(3+d)$D-space, called *superspace*, each Bragg reflection in the diffraction pattern of an aperiodic crystal can be uniquely indexed by $(3+d)$ integers (van Smaalen; 2004):

$$\mathbf{H} = \sum_{k=1}^{3+d} h_k \mathbf{a}_k^* \tag{3.1}$$

where $\mathbf{H}$ is the scattering vector of the Bragg reflections, d is the number of additional periodicities, h_k are integers, and $\mathbf{a}_k^*$ are the reciprocal basis vectors. The d additional vectors are called the *modulation wave vectors* or $\mathbf{q}$-vectors. They are used to index the satellite reflections. The modulation wave vectors $\mathbf{q}^j = \mathbf{a}_{3+j}^*$ $(j = 1, ..., d)$ are not linearly independent and they can be expressed as linear combination of the first three reciprocal basis vectors $(\mathbf{a}_1^*, \mathbf{a}_2^*, \mathbf{a}_3^*)$ which are used to index the main reflections (van Smaalen; 2004):

$$\mathbf{q}^j = \sum_{i=1}^{3} \sigma_{ji} \mathbf{a}_i^* \tag{3.2}$$

At least one of the components σ_{ji} for every j must be an irrational number for the indexation by $3+d$ integers to be unique. If all σ_{ji} are rational numbers, the modulation is commensurate and it is possible to index the reflections with an appropriate choice of a 3D *supercell*.

Superspace is constructed by defining a reciprocal lattice in $(3+d)$D-space, such that the observed reflection positions are the projections of the reciprocal lattice vectors in superspace (Fig. 3.3). The usual construction of the reciprocal basis Σ^* in $(3+d)$ superspace is (van Smaalen; 2004):

$$\Sigma^* : \begin{cases} \mathbf{a}_{s,i}^* & = (\mathbf{a}_i^*, \mathbf{0}) \qquad i = 1, 2, 3 \\ \mathbf{a}_{s,3+j}^* & = \left(\mathbf{q}^j, \mathbf{b}_j^*\right) \qquad j = 1, ..., d \end{cases} \tag{3.3}$$

where $\mathbf{a}_{s,i}^*$ $(i = 1, 2, 3)$ are the reciprocal basis vectors in 3D space while $\mathbf{a}_{s,3+j}^*$ $(j = 1, ..., d)$ are the additional reciprocal basis vectors in superspace. The additional

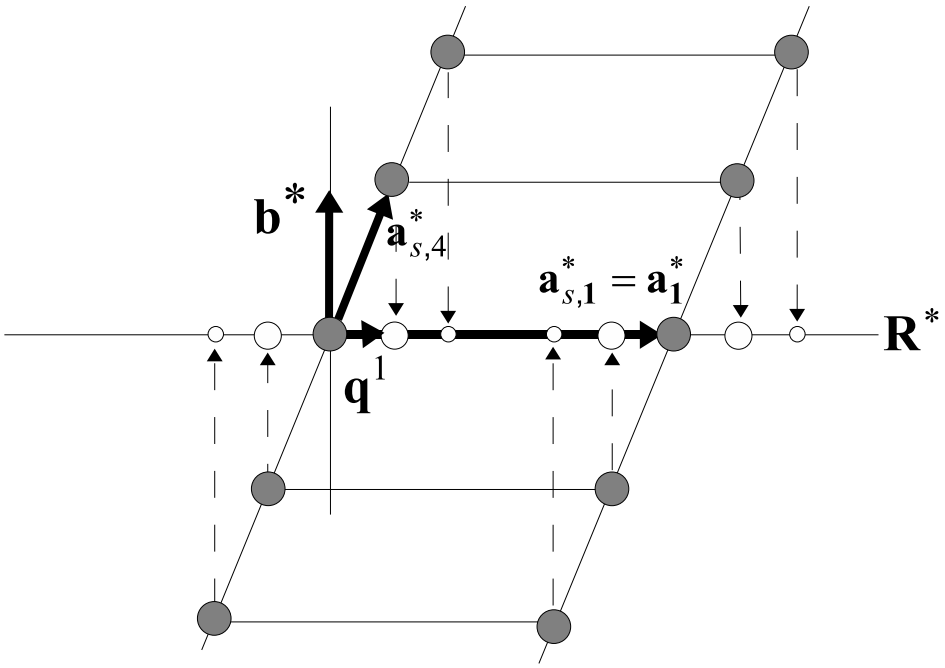

Figure 3.3: Embedding of the diffraction pattern along the reciprocal lattice line $\mathbf{R}^*$ of a modulated crystal in a (1+1)D superspace. Empty circles denote the satellite reflections obtained by projecting reciprocal lattice points of the (1+1)D space along $\mathbf{b}^*$ onto $\mathbf{R}^*$

vectors $\mathbf{b}_j^*$ are the components of the d vectors in the additional dimensions of superspace and are defined perpendicular to 3D space such that the components of the reciprocal basis vectors in 3D space are zero in these dimensions. A reciprocal vector $\mathbf{b}_j^*$ defines a direct vector $\mathbf{b}_j$ that is parallel to $\mathbf{b}_j^*$ and obeys $\mathbf{b}_j \cdot \mathbf{b}_j^* = 1$.

The direct basis vectors in superspace corresponding to the reciprocal basis (Eq. 3.3) are:

$$\Sigma : \begin{cases} \mathbf{a}_{s,i} = \left(\mathbf{a}_i, -\sum_{j=1}^{d} \sigma_{ji} \mathbf{b}_j \right) & i = 1,2,3 \\ \mathbf{a}_{s,3+j} = (\mathbf{0}, \mathbf{b}_j) & j = 1,...,d \end{cases} \tag{3.4}$$

3.2.3 Atoms in Superspace

As mentioned in Section 3.2.1, modulated crystals are characterized by periodic distortions of the basic structure. These periodic perturbations are described by *modulation wave functions* $\mathbf{u}(\bar{x}_{s,4})$ which are periodic with respect to the fourth-dimension

in superspace with period 1. The true atomic positions of one-dimensionally modulated crystals can be expressed as (van Smaalen; 2004):

$$\begin{aligned} x_i &= \bar{x}_i + u_i\left(\bar{x}_{s,4}\right) \qquad i = 1,2,3 \\ \bar{x}_{s,4} &= t + \mathbf{q}\cdot\bar{\mathbf{r}} \\ \mathbf{q}\cdot\bar{\mathbf{r}} &= \sum_{i=1}^{3}\sigma_i\bar{x}_i \end{aligned} \tag{3.5}$$

where $\bar{\mathbf{r}}$ is the vector with coordinates $\bar{x}_i$ of the basic structure, $\bar{x}_{s,4}$ is the fourth superspace coordinate of the basic structure, and t is the phase of the modulation. The modulation functions are usually expressed as Fourier series (van Smaalen; 2004):

$$\mathbf{u}\left(\bar{x}_{s,4}\right) = \sum_{n=1}^{n_{max}} \mathbf{A}^n \sin\left(2\pi\bar{x}_{s,4}\right) + \mathbf{B}^n \cos\left(2\pi\bar{x}_{s,4}\right) \tag{3.6}$$

$$p\left(\bar{x}_{s,4}\right) = p_o + \sum_{n=1}^{m} p_s^n \sin\left(2\pi\bar{x}_{s,4}\right) + p_c^n \cos\left(2\pi\bar{x}_{s,4}\right) \tag{3.7}$$

where $\mathbf{A}^n = (A_1^n, A_2^n, A_3^n)$ and $\mathbf{B}^n = (B_1^n, B_2^n, B_3^n)$ are the six independent coefficients for each harmonic of the displacement modulation, and p_s^n and p_c^n are the sine and cosine coefficients of the nth harmonic of an occupational modulation, with p_o the average site occupancy.

The positions of the atoms in (3+1)D-superspace are obtained by application of the superspace lattice translations (Eq. 3.4) to atoms in 3D space. This yields a set of points which form a *string* that is parallel to and periodic along the fourth dimension $\mathbf{a}_{s,4}$ (Fig. 3.4). These atomic strings (also plane and volume in (3+2)- and (3+3)-superspace, respectively) are collectively called *atomic domains*. They do not need to be continuous within the period along the fourth dimension but might be described by discontinuous functions, e.g. *crenel* functions or *sawtooth* functions. Conversely, the atomic structure in the physical space $\mathbf{R}$ is obtained as the 3D section of the four-dimensional periodic structure where the atomic modulation functions are represented along the fourth dimension. Although the structure is periodic in the superspace lattice spanned by the basis vectors $\mathbf{a}_{s1}$ and $\mathbf{a}_{s4}$, it is not in general periodic in the 3D section which represents the physical space. The 3D section of (3+1)D superspace results from the intersection of the line $\bar{x}_{s4} = t = t'$ with the atomic domains. Thus the value of t determines the resulting 3D structure. For *incommensurate modulation*, all 3D sections are identical and provide equivalent

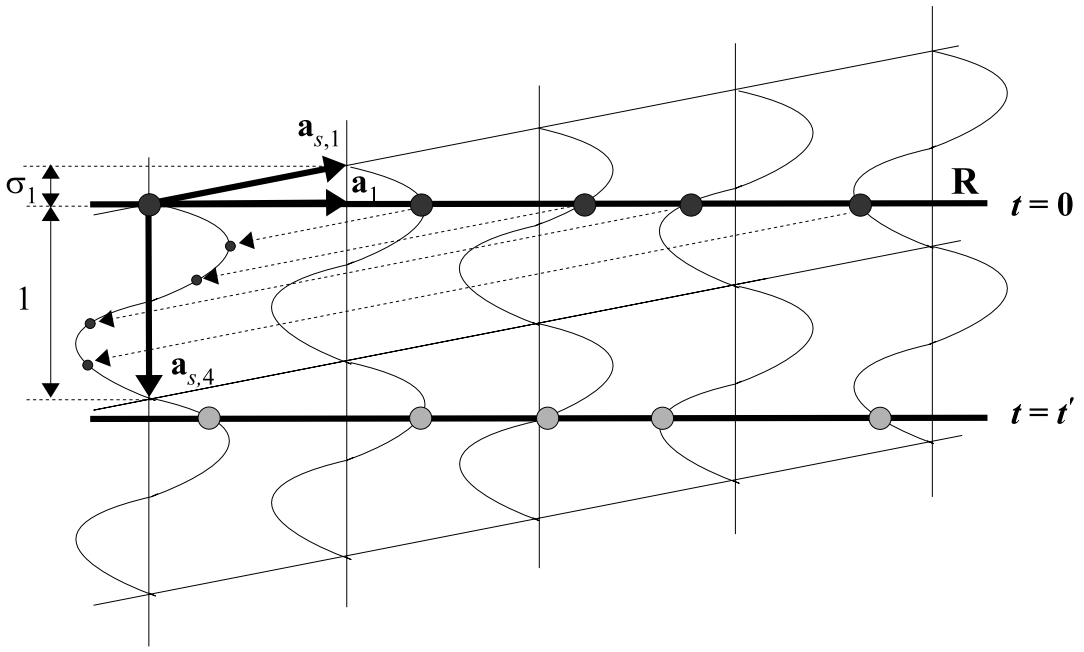

Figure 3.4: Atomic structure in direct superspace of an incommensurately modulated crystal. The superspace structure is obtained by application of superspace translations to atoms in physical space **R** resulting in a set of points (small dark circles) that define a wavy line (atomic domain) with the shape of the modulation function. The line $t = 0$ represents the 3D space **R**. Its intersection with the atomic domains gives the atoms (big dark circles) in 3D space that comprise a non-periodic structure. Other one-dimensional cut with non-zero values of t yields an equivalent but different representation of the structure in 3D space.

descriptions of physical space. The corresponding 3D section can also be interpreted as an irrational cut of (3+1)D superspace, i.e., **R** does not pass through a lattice point in 3D space and the component σ_1 of the **q**-vector is an irrational number (Schönleber; 2002).

In the case of a *commensurate modulation*, different values of t, i.e. different 3D sections, yield different structures in 3D space. For an N-fold supercell, there are only N equivalent 3D sections corresponding to $t = t_o + l/N$ where $l = 0, ..., N-1$. The 3D section in commensurate modulation, which is usually described in 3D space as *superstructure*, is a rational cut of the (3+1)D superspace in which **R** passes through a lattice point with the component σ_1 of the **q**-vector being a rational number. The atomic positions in a modulated crystal are completely characterized

by the average atomic positions and by the shape of the atomic domains. Thus the problem of determining the structures of modulated crystals in superspace concerns primarily the correct characterization of the atomic domains, and additionally in the case of commensurate modulation, the correct specification of the initial phase of modulation t_o .

Chapter 4

Data Processing of CCD and IP Data

As described in Chapter 2, area detectors offer the advantage of faster data collection with a high degree of data redundancy resulting from the measurement of many symmetry-equivalent reflections and of the same reflections in different orientations. This helps to reduce errors and also provides information on which to base corrections for effects such as absorption (Clegg et al.; 2001). Along with this effectiveness and efficiency in data collection comes the need for a careful data processing. This elaborate task usually entails accurate crystal orientation matrix determination and indexing of reflections, proper data reduction by integration of the frames, and appropriate application of absorption corrections. This chapter describes these procedures that were involved in the data processing from the measurements performed with the SMART CCD and the MAR345 IP detectors.

4.1 Treatment of CCD Data

4.1.1 Analyzing the Reflections

In this thesis, measurements using synchrotron radiation with a CCD detector were performed on the compounds $Ca_5Nb_5O_{17}$ ($n = 5$) and $Ca(Nb,Ti)O_{3.33}$ ($n = 6$). The data collection was facilitated using the SMART software (Bruker; 1998b). Before the actual data collection was carried out, initial test measurements were performed to determine the appropriate experimental parameters to be used, such

as detector distance, frame width, and exposure time in consideration of the amount of data that is desired to be collected and the limited beam time available for data collection. These considerations are discussed in Section 2.2.2. The tests were also performed to confirm the crystal quality by collecting a couple of images and examining the reflections recorded. The in-plane dimensions of a reflection may be obtained by drawing a vector on the image across the reflection, and plotting the observed intensity as a function of the position along this line (Fig. 4.1*a*). By drawing vectors in different directions across the reflection, one can tell if the reflection has uniform intensity in different directions. To measure the mosaic spread of the

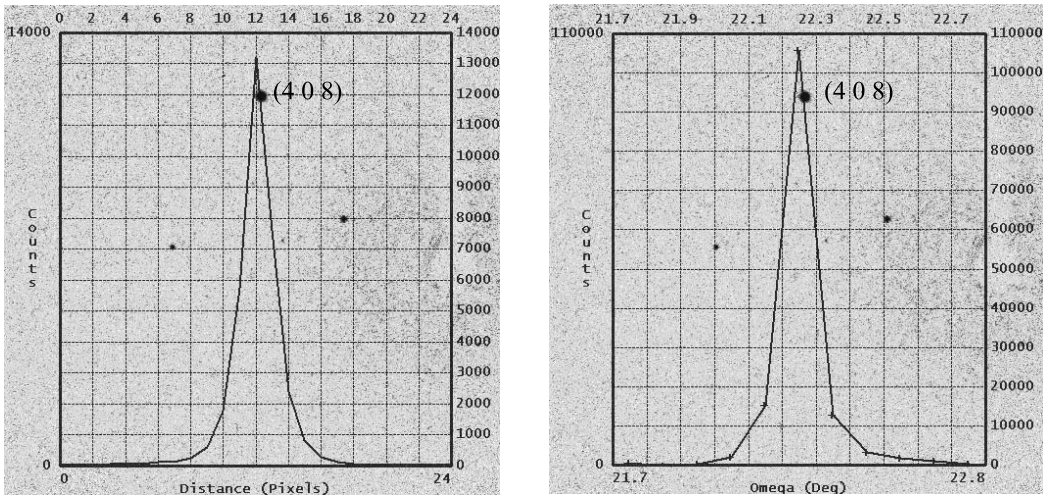

Figure 4.1: (a) Vector plot of the intensity and (b) rocking curve of the reflection (4 0 8) of $Ca(Nb,Ti)O_{3.33}$ ($n = 6$). The plots are superimposed on the measured diffraction image.

diffraction data, the rocking curves of the reflections are plotted (Fig. 4.1*b*). A central frame (from a series of frames collected) is displayed about which the rocking curve is computed. A box is defined to enclose the reflection to be analyzed and an appropriate frame half-width is entered which corresponds to the number of frames above and below the central frame. The program calculates the background-subtracted intensity for the region bounded by the box and displays the result in a plot of intensity versus scan angle. The background is computed as the average of the points on the perimeter of the box, excluding those points which are more than

3 standard deviations above the mean. The box size must be chosen sufficiently large since in most cases the X,Y centroid of the reflection may change as a function of the scan angle (Bruker; 1998b). Information from the rocking curve is useful in estimating Z-dimension (through-plane dimension) of the integration box to be used in the subsequent data reduction. Analysis of the rocking curve is also helpful in revealing possible splitting of the reflection which may not be obvious from its 'innocent' appearance within a single image. Thus by visually inspecting the rocking curves of a couple of reflections, one can obtain information about the quality of the crystal.

4.1.2 Indexing and Finding the Orientation Matrix

Once the goodness of the crystal to be used has been affirmed and the experimental parameters have been established, a series of frames (about 200) is collected to determine the orientation matrix and the unit cell. The task of finding the orientation matrix involves the following steps (Bruker; 1998b): (1) clear the reflection array; (2) threshold the frames to build a list of spots stored in the reflection array; (3) auto-index; (4)perform least-squares refinements on the primitive cell; (5) determine the Bravais lattice; (6) perform least-squares refinements on the resulting unit cell, writing the cell parameters and matrix to a '.p4p' file for subsequent use by data reduction programs. Before going through this procedure, the correct crystal-detector distance and the X,Y beam center must have been entered in the configuration file of SMART. The beam center is usually determined beforehand from a rotation photo of a strongly diffracting test crystal and by using the pixel cursor or circle cursor to measure the center. Beam center coordinates which are in error by more than half the smallest center-to-center spot spacing usually result in an increased probability of mis-indexation (Bruker; 1998b). In addition, a valid spatial correction must have been installed, preferably (although not necessarily) computed from a fiducial-plate frame taken at the same distance as the data frames.

Before searching for peaks in the images, the reflection array should be cleared of any previously stored reflection list which will not be used in obtaining the orientation of the reciprocal lattice. However in practice, for a multi-run measurement, once a reflection list is established for a certain run, the list is kept in the reflection array while a new set of reflections are added after thresholding the new set of images of the next run. This is to ensure that there is a uniform orientation

matrix describing the reflections in different runs. After the new set of reflections have been indexed, this combined list is then used for least-squares refinement of the unit cell. Reflections belonging to the previous run are then gradually removed from the list before a new least-squares refinement is performed. Eventually, in the final least-squares refinement, the list should contain only reflections belonging to the images of the current run.

PEAK SEARCH

The first frame and the number of frames where to look for reflections are specified. Depending on the number of reflections per frame, one may need to search reflections in a few or several frames to obtain a suitable orientation matrix. In the measurements reported, 200–300 frames are sufficient. During the search procedure, the frames are thresholded, i.e. only reflections whose I/σ is greater than a specified value will be stored in the reflection array. Moreover, the program considers only reflections within the resolution range and within the limits of the frame specified by the user. This option is useful when excluding reflections that lie at the frame boundaries or those which are found near the beam stop.

INDEXING

Once a new set of reflections have been added to the reflection array after thresholding, they can be indexed by an auto-indexing routine which determines the reduced primitive unit cell according to specified fractional range of axis lengths. The auto-indexing algorithm operates on difference vectors which are classified into groups based on specified input tolerances. These tolerances (with typical values as used in the measurements indicated inside the parentheses) include fractional HKL deviation from integers (0.2), minimum number of difference vectors in a group (3), length fraction criterion for grouping (0.3), and fraction of total number of difference vectors which must fit in order to accept a trial axis length (0.8). The predicted positions according to the computed orientation matrix may also be displayed in the images. The center of the reflection across the scan angle is overlayed by a square while the parts of the reflection contained in the frames above and below the central frame are overlayed by circles and crosses, respectively (Fig. 4.2). Comparison of the predicted position and observed position of the reflections provides information about the goodness of the orientation matrix.

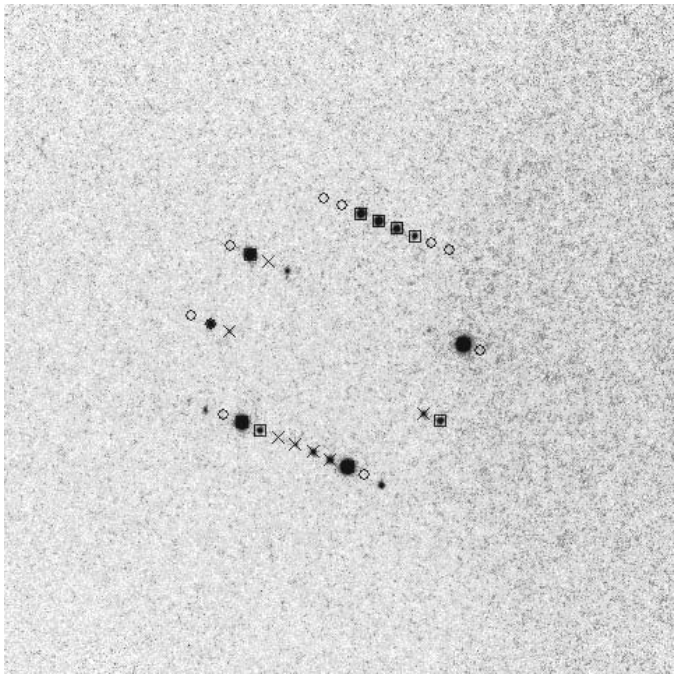

Figure 4.2: Predicted positions of the reflections of $Ca_5Nb_5O_{17}$ ($n = 5$) overlayed on a measured diffraction frame. Squares denote the centers of reflections while circles and crosses refer to parts of the reflections above and below the frame that is displayed, respectively.

LEAST-SQUARES REFINEMENT

Following indexing, least-squares (LS) refinements are performed to determine and refine the orientation matrix, unit cell parameters, and corrections to the detector position, goniometer zeros and crystal translations (Bruker; 1998b). The LS refinement is performed based on a specified crystal-system constraint. In practice the unconstrained tricilinic system is selected because it fits the diffraction data better. A quick linear LS refinement is performed to establish the unit cell parameters and orientation followed by a non-linear refinement which incorporates positional corrections and constraints. The constraints are imposed by specifying the constraint mask, which fixes certain variables during the non-linear refinement. In practice, the bit mask of 512 corresponding to crystal-translation constraint, is applied. After each execution of LS, reflections whose observed reciprocal-lattice

vector (RLV) differ from the calculated RLV by more than a specified maximum error are removed from the reflection array. In practice, the RLV error tolerance should not be too tight in the initial stage of the refinement, as not to throw away a significant number of reflections. In the reported measurements, an initial tolerance of 0.03 has been used. Smaller values have been used in the successive executions of LS after modifying the reflection array. The output of the LS refinement is an ASCII file with a '.p4p' extension [1] containing the refined orientation matrix and unit cell parameters including their standard deviations (Appendix A). Several histograms are presented showing the distribution of the unsigned differences between the observed and calculated values of H,K,L, scan angle, and detector X,Y position of each reflection in the array. In all cases, a better refinement corresponds to the differences that are more closely bunched toward the left side of the histogram. In practice, reflections with unusually high parameter differences are removed from the reflection array and a new LS is executed. These reflections are usually noisy weak reflections or those lying at the frame edges. Following the histograms are the overall average and root-mean-square (RMS) differences for the same quantities mentioned above for the histograms. The average values indicate any systematic bias in the results. If these values are substantial fraction of the corresponding RMS values, there might be mis-indexing or mis-alignment in the system due to incorrect spatial correction and incorrect estimates of the detector distance and beam center specified in the configuration file of SMART (Bruker; 1998b). The reflections contributing predominantly to the average and rms differences are presented in a list of 'worst agreements' between observed and calculated RLV. The overall refinement statistics is also reported, including the starting and ending residual, goodness-of-fit (preferably 1.0 or lower), and number of refinement cycles performed.

BRAVAIS LATTICE DETERMINATION

SMART also determines the possible Bravais lattices corresponding to the specified unit cell parameters and standard deviations based strictly on the metric symmetry. The user chooses from a set of possible solutions which are ranked according to the degree of symmetry and goodness-of-fit. The highest-symmetry solution with

[1] A file with the same name except with extension '._pr' is also produced but contains less information than the .p4p file. Both the .p4p file and ._pr file can be read by the integration program SAINT.

goodness-of-fit better than an input threshold is flagged as the most likely solution. After specifying the solution, the program re-indexes the reflections in the reflection array to correspond to the selected Bravais lattice. Subsequently, new LS refinements may be executed for this revised lattice. After the final refinement has been made, the final '.p4p' file, which contains the unit cell parameters, orientation matrix and list of reflections used in the refinement, is saved for later use in data reduction.

4.1.3 Data Reduction

The program SAINT (Bruker; 2000) reduces the image frames into files containing information about each reflection such as HKL indices, intensity, standard deviation of the intensity, setting angles, positions, and direction cosines. It integrates contiguous frames using the orientation matrix from the '.p4p' file produced by SMART. The output intensities are corrected for Lorentz factor, polarization, air absorption, and absorption due to variation in the path length through detector faceplate. SAINT determines the spot-shape profiles with concurrent refinement of the starting orientation matrix and initial background. During integration, it eliminates spots whose shapes correlate poorly with the model profile shape relative to other spots of similar I/σ. The unit cell parameters are also refined with the use of strong reflections from the whole run. SAINT determines the reflection spot shapes for nine regions of the detector of roughly equal area. These model shapes are then used for determining the area of integration for each reflection. The model profile shapes are also used to calculate the correlation coefficients for purposes of data rejection and profile fitting of weak reflections. The model spot for each region is defined on a $9 \times 9 \times 9$ grid of points space to fill the specified integration box. SAINT then sorts the reflections according to a specified point-group symmetry and writes to a specified output file, '.raw'. Only reflections within the specified resolution limit are included in the integration.

INTEGRATION BOX

Integration by SAINT is greatly influenced by the spot size used and incorrect values are the most common reason for inadequate data quality. Incorrect spot sizes lead to incorrect integration of diffracted intensities which, in turn, results in inaccuracies in the structural parameters. The size of the integration box is specified

by entering its X,Y,Z dimensions (in degree). These values are used by SAINT to determine the angular range spanned by the $9 \times 9 \times 9$ integration volume stored for the model spot profiles. The box should be small enough to contain considerable spot information and large enough to accommodate every profile with some room for positional errors. A good estimate of the box size may be obtained by measuring a couple of reflections and examining their profiles in SMART (see Section 2.2.1). It is better to make the estimate too large than too small. The box size may be fixed or it may be refined during integration. In the latter case, SAINT refines the input values for the box size and makes the corresponding optimization. The volume is considered satisfactory if the initial model profiles span 5/9 of the volume but no more than 7/9 of the volume in each dimension (Bruker; 2000). If the initial profiles do not fall within these limits, the spot size estimates are modified and the calculation of initial profiles is repeated, up to two times. If on the third try the profile size still falls outside the limits, a warning message will be displayed which indicates that the spot size refinement did not converge. In the data reduction of the reported measurements, it has been found that SAINT underestimates the size of the box and reports about 2/3 of the box size necessary to carry out a good integration. The box size may be adjusted after each integration cycle by inspecting the $9 \times 9 \times 9$ average profiles printed by SAINT. The profile is printed as nine 9×9 XY-sections averaged over nine sections of the detector with the maximum intensity scaled to 100 (Fig. 4.3). Ideally, only sections 4-6 should contain nonzero entries while the perimeter of each section should be filled with zeros. Usually some 'spot density' may exist in sections 2 and 8 especially when the reflections are ellipsoidal. The maximum intensity (100) should also be contained in section 5 if the reflection is correctly centered in the box. In the final integration cycle of the reported integration, box size refinement has been suppressed and a box size of XY-dimensions between 1.1°–1.2° and Z-dimension between 0.5°–0.6° has been found appropriate for integrating the reflections. Statistics concerning the box size are reported after integration and inspection of these values is useful in judging the success of integration. They include:

- *AVG % Profile Volume Integrated* - This is the average of the $9 \times 9 \times 9$ profile volume with model profile intensity above the 2% noise threshold. Ideally, this value is in the range 10–25% but because spots tend to be non-spherical, as in the case of the data in this thesis, they are actually lower.

```
! Averaged profile: Section 1→3
 0  0  0  0  0  0  0  0  0  0    0  0  0  0  0  0  0  0  0  0    0  0  0  0  0  0  0  0  0  0
 0  0  0  0  0  0  0  0  0  0    0  0  0  0  0  0  0  0  0  0    0  0  0  0  0  0  0  0  0  0
 0  0  0  0  0  0  0  0  0  0    0  0  0  0  0  0  0  0  0  0    0  0  0  0  0  0  0  0  0  0
 0  0  0  0  0  0  0  0  0  0    0  0  0  0  0  0  0  0  0  0    0  0  0  1  1  0  0  0  0
 0  0  0  0  0  0  0  0  0  0    0  0  0  0  0  0  0  0  0  0    0  0  0  1  2  0  0  0  0
 0  0  0  0  0  0  0  0  0  0    0  0  0  0  0  0  0  0  0  0    0  0  0  0  1  0  0  0  0
 0  0  0  0  0  0  0  0  0  0    0  0  0  0  0  0  0  0  0  0    0  0  0  0  0  0  0  0  0
 0  0  0  0  0  0  0  0  0  0    0  0  0  0  0  0  0  0  0  0    0  0  0  0  0  0  0  0  0
 0  0  0  0  0  0  0  0  0  0    0  0  0  0  0  0  0  0  0  0    0  0  0  0  0  0  0  0  0

! Averaged profile: Section 4→6
 0  0  0  0  0  0  0  0  0  0    0  0  0  0  0  0  0  0  0  0    0  0  0  0  0  0  0  0  0
 0  0  0  0  0  0  0  0  0  0    0  0  1  1  2  2  1  0  0    0  0  0  0  1  0  0  0  0
 0  0  1  1  2  1  0  0  0    0  1  3  6  9  6  2  1  0    0  0  0  1  2  1  1  0  0
 0  1  2  5  9  4  1  0  0    0  2  7 25 46 23  6  2  0    0  0  1  5 10  6  2  0  0
 0  1  2 10 19  7  2  0  0    0  2 10 44100 43  9  2  0    0  0  2 10 25 13  3  1  0
 0  0  1  5  8  4  1  0  0    0  2  7 23 43 23  7  2  0    0  0  2  6 12  8  2  1  0
 0  0  1  1  2  1  1  0  0    0  1  3  6  9  6  3  1  0    0  0  1  2  3  2  1  0  0
 0  0  0  0  0  0  0  0  0    0  0  1  2  2  2  1  0  0    0  0  0  0  1  1  0  0  0
 0  0  0  0  0  0  0  0  0    0  0  0  0  0  0  0  0  0    0  0  0  0  0  0  0  0  0

! Averaged profile: Section 7→9
 0  0  0  0  0  0  0  0  0  0    0  0  0  0  0  0  0  0  0  0    0  0  0  0  0  0  0  0  0  0
 0  0  0  0  0  0  0  0  0  0    0  0  0  0  0  0  0  0  0  0    0  0  0  0  0  0  0  0  0  0
 0  0  0  0  0  0  0  0  0  0    0  0  0  0  0  0  0  0  0  0    0  0  0  0  0  0  0  0  0  0
 0  0  0  0  1  0  0  0  0  0    0  0  0  0  0  0  0  0  0  0    0  0  0  0  0  0  0  0  0  0
 0  0  0  1  2  1  0  0  0  0    0  0  0  0  0  1  0  0  0  0    0  0  0  0  0  0  0  0  0  0
 0  0  0  1  1  1  1  0  0  0    0  0  0  0  1  1  1  0  0  0    0  0  0  0  0  0  0  0  0  0
 0  0  0  1  1  1  0  0  0  0    0  0  0  0  1  1  0  0  0  0    0  0  0  0  0  0  0  0  0  0
 0  0  0  0  0  0  0  0  0  0    0  0  0  0  0  0  0  0  0  0    0  0  0  0  0  0  0  0  0  0
 0  0  0  0  0  0  0  0  0  0    0  0  0  0  0  0  0  0  0  0    0  0  0  0  0  0  0  0  0  0
```

Figure 4.3: Spot profile of $Ca_5Nb_5O_{17}$ (n=5) averaged over nine detector regions shown as nine 9×9 XY-sections.

- *AVG % Profile Volume Populated* - Only pixels nearest the HKL being integrated are included in a reflection profile. Normally, this value should be close to 100%, if not, the spots are strongly overlapping which may be due to overestimation of the box size.

- *X,Y,Z Fraction of Prof. Volume Used* - This refers to the maximum fraction X, Y, or Z dimension used in the model profile. Ideally, these values range from 56–78%. If a value of 100 is obtained for a particular dimension, the box size along this dimension may be too small and need to be increased.

- *Max Profile % On X,Y,Z Boundaries* - This reports the largest intensity of the model profile (as a percentage of the profile maximum) appearing on the X,Y and Z borders of the model profile. A significant value (above 10%) may indicate that the box size may be too small, or that there are large positional errors.

- *Number of Overlapping Spots* - This refers to the number of spots for which

the volume corresponding to the model profile was not 100% filled from pixels with HKL indices nearest the indices of the spot being integrated. This may be due to incorrect orientation matrix or too large box size. In this case, the intensity of the spot being integrated is adjusted by the relative amount of intensity in the unfilled volume of the model profile.

ORIENTATION MATRIX

At the start of the integration routine, SAINT reads in the orientation matrix contained in the '.p4p' file generated by SMART. During integration, SAINT performs periodic updating of the orientation matrix depending on the specified frequency of refinement. A zero input for the frequency means that the original orientation matrix found in the '.p4p' file is used throughout the integration process. If a non-zero input n is entered, the matrix is updated every n frames using reflections which are above a specified I/σ threshold. This threshold is also used to update the model spot profiles. In the reported data reduction, good results have been obtained by using a threshold between 20–30 and a frequency of 200 for updating the orientation matrix. At the end of integration, SAINT reports several statistics concerning the closeness of the predicted positions from the observed positions: (Bruker; 2000):

- *ERRX ERRY ERRZ* - This refers to the average difference between the observed and the predicted positions of the reflections, measured in pixels. ERRX and ERRY are the average positional errors in the plane of the frame while ERRZ is the average difference between the observed and the predicted frame number. If any of these numbers is consistently more than about 0.2 pixels in absolute value over a range of many frames, there is a probably a significant error in the orientation matrix, in which case, the orientation matrix may need to be re-refined using SMART.

- *RMSX RMSY RMSZ* - This refers to the root-mean square (RMS) difference in observed versus predicted position (where a Z pixel is equivalent to frame number. Values consistently above about 0.3 pixels indicate that the data may be weak or there may be a problem with the orientation matrix or spatial calibration.

- *% X,Y,Z more than 0.5 pixel* - This refers to the percentage of spots with

absolute values of ERRX, ERRY, ERRZ greater than 0.5 pixel. This should be within 10%, if the orientation matrix is satisfactory.

- *% X,Y,Z more than 1 pixel* - This refers to the percentage of spots with absolute values of ERRX, ERRY, ERRZ greater than 1 pixel. For a good matrix, this should not be greater than 1%.

After the integration and output of sorted reflection files for the individual runs, SAINT performs a global cell least squares . It uses the data stored in a temporary file '._MA' which contains the reflections above the specified strong-reflection threshold. The refined orientation matrix and the refined unit cell parameters as well as the goodness-of-fit (preferably 1 or lower) are reported at the end of the integration process (Appendix B).

4.1.4 Absorption Correction

Because of the plate-like shape of the crystals investigated and their relatively high absorption of the radiation used (about 5.8/mm), it was necessary to correct the diffracted intensities for absorption effects. For this purpose, the multi-scan absorption correction program SADABS (Sheldrick; 2002) has been used. The program exploits the data redundancy achieved from measurements with CCD detectors. It reads in the '.raw' files produced by SAINT and corrects the integrated intensities for absorption effects. The reflections are averaged based on a specified Laue group. During program execution, the mean I/σ threshold (usually 3) is provided for including a group of equivalents in the subset of reflections used for parameter refinement to find a model for systematic errors. Only reflections which lie within a specified resolution limit are included in the parameter determination. The initial value for the parameter 'g' for the weighting scheme (usually 0.02) is also specified. This parameter is later determined by the program in the error analysis part of the data processing. A restraint esd for consecutive scale factors, expressed as fraction of their values (the default value of 0.02 is usually good), is also specified. Moreover, the highest orders of the even and odd harmonics to be used for the spherical harmonic absorption correction of the diffracted beam are provided. For moderate absorption (as in the case of the crystal investigated), values of 6 and 3, respectively, are suitable. Values of 4 and 1 are recommended for small absorption while 8 and 5 for strong absorption. After the required number of cycles have been performed, the

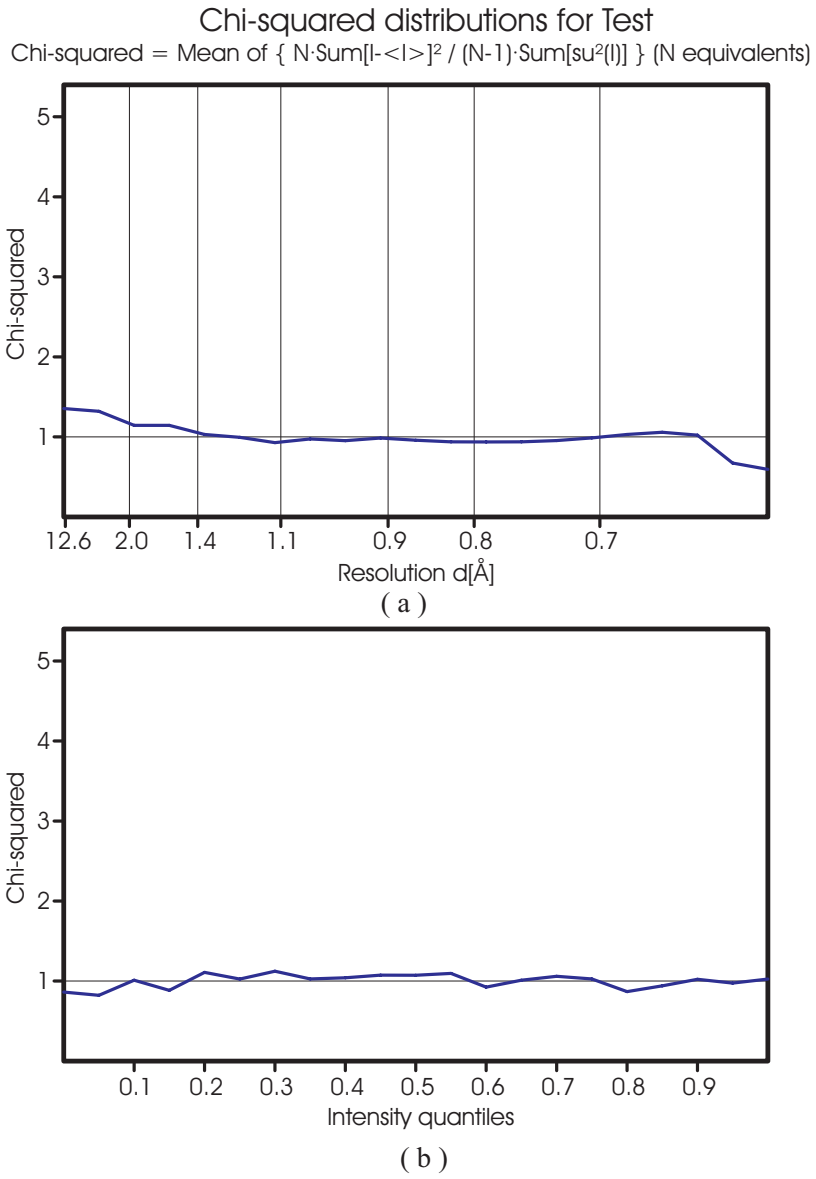

Figure 4.4: Plots of χ^2 versus (a) Resolution and (b) Intensity of $Ca_5Nb_5O_{17}$ (n=5).

R_{int} value for the reflections used for parameter refinement is printed. In the case of $Ca_5Nb_5O_{17}$ (n=5), for example, $R_{int} = 0.0773$ before parameter refinement, and after 100 cycles parameter refinement, it improved to $R_{int} = 0.0364$. During the establishment of an error model, the program retains only reflections which lie within a specified resolution limit and whose error/σ is less than some specified number. A cutoff value of 4.0 (which has been used in the reported data processing) is usually satisfactory and catches the real errors without upsetting the statistics too much. The program then tries to find the best 'g' value for the error model and establishes the appropriate weighting scheme. The best test of success in establishing a good error model is that the plots of χ^2 against intensity and against resolution should be horizontal lines, with χ^2 equal to one (Fig. 4.4). After establishing the weighting scheme, the program prints a table giving for each scan the following information: R_{int}, minimum and maximum values for the diffracted beam transmission factors, the scaling factor k, the number of reflections, and the number with intensities greater than 2σ (Appendix C).

4.2 Treatment of Image Plate Data

The image plate X-ray diffraction data collected on $Ca_5Nb_4TiO_{17}$ ($n = 5$) using MAR345 dtb was processed and reduced using the computer program CRYSALIS RED (Oxford Diffraction; 2004). The software incorporates into one package the routines for peak search, indexing of reflections and determination of the orientation matrix, integration of the frames, and absorption correction. The data processing is based on configuration parameters specified in a parameter file. This file contains the machine settings used in the experiment, such as detector distance, XY-coordinates (in pixels) of the detector center, goniometer offsets (if there is any), and the type of radiation used. A beam stop mask may also be defined by specifying its position and dimensions so that the area obscured by the shadow of the beamstop may be ignored during data processing. The different runs in the measurements performed are defined by the type of scan (ω or ϕ), starting and ending angles of the run, scan width or frame width, exposure time, goniometer angles, and the frame range to be processed.

PEAK SEARCH

As in SMART, the range of frames to be scanned for reflections is specified in the

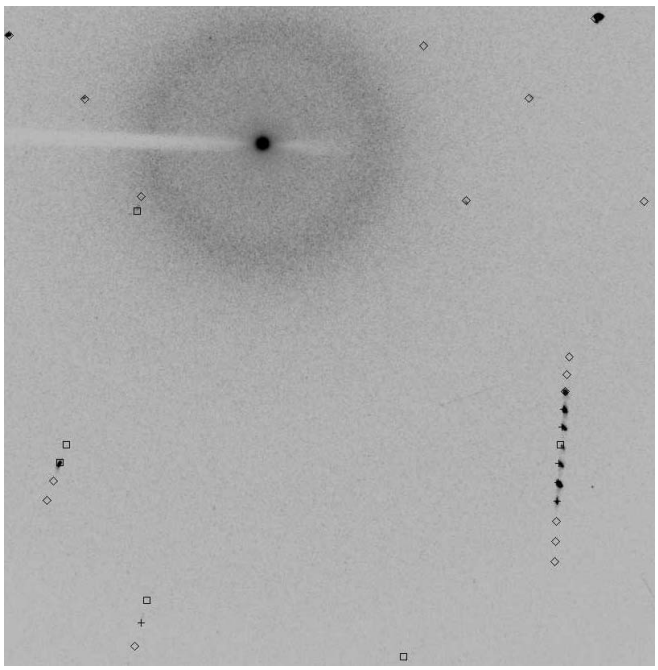

Figure 4.5: Predicted positions of the reflections of $Ca_5Nb_4TiO_{17}$ ($n = 5$) overlayed on a measured diffraction frame. The rhombus, cross, and square symbols denote that the center of the reflection is before, in , after the frame, respectively.

peak hunting procedure. In the case of the data collected, the first 100 frames were sufficient to obtain a suitable orientation matrix. By default an automatic threshold and background determination is performed during peak search although one may choose to define the parameters for peak hunting and background determination. The contents of the peak hunting table can be graphically visualized using the Ewald explorer reciprocal space visualizer.

INDEXING

CrysAlis has an auto-indexing routine which assigns indices to the reflections in the peak hunting table and produces an orientation matrix. In the case of unsuccessful indexing, the constraints applied to the unit cell lengths and angles can be relaxed. Alternatively, one may edit the peak table and remove some weak reflections or spurious reflections and then retry the auto-indexing. Once a unit cell is obtained, a reduced cell is derived. The program prints a table of all possible reduced cells along with a figure-of-merit. The cell with the highest symmetry and highest figure-of-merit is the most likely solution. The goodness of the orientation

matrix may be inspected by overlaying the predicted positions on the diffraction frames. (Fig. 4.5). The orientation matrix, unit cell parameters, goniometer parameters, and detector parameters are refined by doing a least-squares refinement.

Data Reduction

Once a suitable orientation matrix has been obtained, the raw images may be reduced to create a reflection file that contains the indices of the reflections, the intensities and their corresponding standard uncertainties, and other characteristic information like direction cosines (or Schwarzenbach psi) which can be used for absorption correction. In the data reduction, one may apply lattice extinctions which is particularly useful for larger unit cells that have overlap problems. One may also refine the 'q' vectors for data reduction in the case of incommensurate samples. The 'scan width' for the reflections is specified. This parameter does not refer to the frame width but instead is related to the mosaicity of the crystal. An estimate of the scan width may be obtained by observing in how many frames (therefore how many degrees in ϕ) a certain reflection is contained. The intrinsic reflection width is computed from the scan width value. This value resembles the normal constant scan width on conventional diffractometers which is between $0.7° - 1.0°$ for good crystals and between $1.0° - 4.0°$ for bad crystals. In the case of the crystal measured in this thesis, a scan width of 1.5° has been used. The program may also apply special corrections specified by the user, which are useful especially when the crystal quality is not good. For instance, the peak finding window may be adjusted by specifying the minimum and maximum size of the mask used in data reduction. This mask is similar to the integration box used in SAINT. By default, the program makes an automatic profile shape determination which also takes into consideration the $K_{\alpha 1}$/ $K_{\alpha 1}$ splitting, as it is present in the reported measurement. In addition, when the crystal does not diffract to high angles, it may be useful to define a resolution threshold. Only reflections which are within the specified value in the '2 Theta max threshold' field are considered in the data reduction. The reduced data set may contain outliers, which are detected by comparing symmetry equivalent reflections. If the Laue group is known, outlier rejection may be selected to eliminate these reflections. Additional information concerning the beam path, e.g. direction cosines or Schwarzenbach psi, may be included in the final '.hkl' file produced by the data reduction. At the end of data reduction, the program writes a summary file which

reports the statistics of the data reduction process including the distribution of reflections against resolution and against intensity (Appendix D). The symmetry equivalent reflections according the specified Laue group are grouped and the R_{int} values are reported with and without outlier rejection. The symmetry equivalent reflections are merged in a separate '.rint' file.

Data reduction is a time consuming process, which mainly consists of extracting reflection profile information. This information, which is stored in a '.rrp' file generated by the data reduction program can be used to repeat the process by imposing different conditions for data reduction. This final stage of data reduction is useful when testing different Laue groups, specifying different resolution limits for retaining reflections and applying different lattice extinctions. It is also used to control the standard uncertainty calculation by specifying the appropriate machine error for the experiment. Moreover, when there are overlaps of reflections, one may specify in this stage rejection criteria for overlap as well as criteria for twin rejection. It is in this stage where one may apply numeric absorption correction after the crystal shape has been given. The result of this final data reduction may be presented in alternative formats for other data processing programs, e.g. STOE '.crs', XPREP '.p4p', and SADABS '.raw'.

4.2.1 Crystal Shape Optimization and Absorption Correction

The CrysAlis Red program can perform numerical absorption correction from a given crystal shape which can be refined by an internal refinement routine or by the plug-in program STOE X-SHAPE (STOE and Cie; 1999). The latter was used for the reported crystal shape optimization. X-SHAPE performs crystal shape refinement from a set of equivalent reflections generated by CrysAlis Red. It provides a number of predefined crystal shapes which can be used to approximate an unknown crystal shape. These shapes include a cube, a dodecahedron, a dodecahedron plus cube, a cylinder plus ellipsoids. In the case of the crystal investigated, the latter shape was selected to approximate the plate-like shape of the crystal.

The selected shape creates a cylindrical crystal cupped with two half-ellipsoids on either end. The XYZ radii of the ellipsoid are specified together with the height of the cylindrical part and the number of the faces to approximate the cylindrical

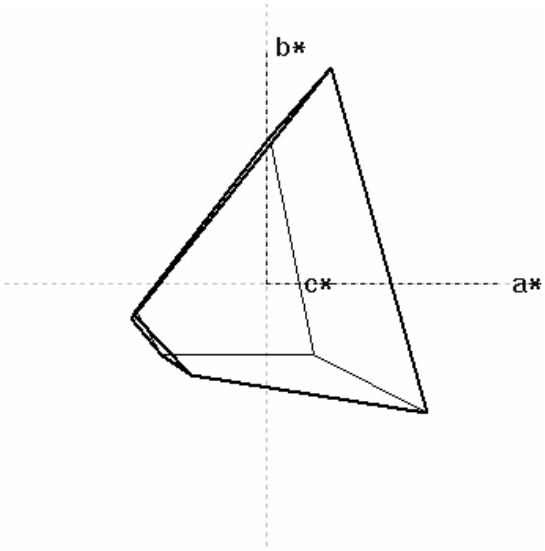

Figure 4.6: Crystal shape of $Ca_5Nb_4TiO_{17}$ ($n = 5$) refined using STOE X-SHAPE

section and the two half-ellipsoids. For the crystal investigated, the shape was approximated with 5 faces for the cylindrical part and one face each for the half-ellipsoids at the ends. During shape optimization, both the distances and the HKL indices of the facets are optimized. The orientation of a face of the crystal is modified by inclining it by a specified angle (about 10–15°), followed by a full rotation carried out in specified steps (about 20°) about the normal to the original face. For each new position, new indices are approximated by integers up to a specified maximum HKL value (usually 30). The distances are incremented by a specified fraction (initially 0.10). The refinement process is iterated in a specified number of times, reducing the increments by a factor of 2 in each iteration. When desired the optimization may be repeated (in the case when some faces have been removed, for instance), decreasing the parameter values in each process until the final optimized shape is arrived at (Fig. 4.6).

At the end of the shape optimization, the HKL indices corresponding to the faces of the crystal and their respective distances from the origin are written in the crystal parameter file '.crs'. Once the crystal shape is known, the parameter file created by X-SHAPE which contains information about the different facets of the crystal, unit cell parameters and absorption coefficient, is imported by CrysAlis Red, and the appropriate numerical absorption correction is applied. At the end of the data

reduction, the merging R-values should be inspected before and after applying the absorption correction. In one run of the reported measurement, for instance, the merging R-values without absorption correction are $R_{int} = 0.04$ and $R_{int} = 0.06$ with and without outlier rejections, respectively. After applying absorption correction, $R_{int} = 0.03$ and $R_{int} = 0.04$ with and without outlier rejections, respectively.

Chapter 5

Crystal Structure of $Ca_5Nb_5O_{17}$

Abstract

The crystal structure at room temperature of $Ca_5Nb_5O_{17}$, an $n = 5$ member of the homologous series $A_nB_nO_{3n+2}$, has been determined by single-crystal X-ray diffraction using synchrotron radiation with CCD area detector. The structure is monoclinic with spacegroup $P2_1/c$ and lattice parameters $a = 7.7494(3)$ Å, $b = 5.4928(1)$ Å, $c = 32.241(1)$ Å, and $\beta = 96.809(4)$ deg. It consists of perovskite-like slabs of corner-sharing NbO_6 octahedra separated by an interslab region, where the octahedra on opposite sides of the gap do not share oxygen atoms resulting into an extra layer of oxygen atoms with respect to the ideal perovskite structure. The slabs are five octahedra wide. Ca atoms within the slabs occupy 12-fold coordinated sites whereas those at the borders show irregular coordination environments. The distortion of the octahedra increases from the center to the borders of the slabs. The computed valences for the Nb ions are very close to 5 at the borders while smaller values were obtained for sites in the middle of the slabs, which suggests that the electrical conduction takes place predominantly in the middle of the slabs.

5.1 Introduction

Perovskite-related oxidic compounds of the series $A_nB_nO_{3n+2}$ (A = Ca, Sr or La and B = Ti or Nb) with $n = 4$, 4.33, 4.5, 5, 6 and 7 have been the subject of much research because of their interesting electronic and dielectric properties (Lichtenberg

et al.; 2001; Kuntscher et al.; 2000, 2002, 2004; Weber et al.; 2001). Depending on the oxygen stoichiometry, these niobium or titanium based oxides exhibit different physical properties. The $n = 4$ insulators display ferroelectricity with very high transition temperatures. Some of the $n = 4.5$ and $n = 5$ electrical conductors show quasi-one-dimensional (1D) metallic behavior at high temperatures whereas at low temperatures there is a metal-to-semiconductor transition (Lichtenberg et al.; 2001; Kuntscher et al.; 2000, 2002, 2004; Weber et al.; 2001). This transition is discussed in terms of a Peierls scenario but there are several open questions (Kuntscher et al.; 2000, 2002, 2004; Weber et al.; 2001).

The crystal structures of compounds $A_nB_n\mathrm{O}_{3n+2} = AB\mathrm{O}_x$ $(x = 3 + 2/n)$ are derived from the $AB\mathrm{O}_3$ perovskite-type structure with slabs of vertex-sharing $B\mathrm{O}_6$ octahedra separated by an interslab region. The octahedra on opposite sides of the interslab region do not share oxygen atoms thus leaving an extra layer of oxygen atoms with respect to the ideal perovskite structure. The crystal structure type is given by n which corresponds to the number of octahedral layers in the slab and can be tuned by adjusting the oxygen content. The ideal perovskite structure corresponds to the limiting value $n = \infty$. Non-integral values of n correspond to ordered sequences of octahedral slabs with different widths, e.g. $n = 4.5$ corresponds to alternating slabs of four and five octahedra wide. The slabs are stacked along the [110] direction of the ideal perovskite structure (along $\mathbf{c}^*$ in the present study). Consecutive slabs of octahedra are shifted with respect to each other by half of the body diagonal of the octahedron. Furthermore, in the interlayer regions the octahedra do not share oxygen atoms, resulting in an irregular coordination of the A cations in these regions.

Diffraction studies on $\mathrm{Ca}_n(\mathrm{Ti,Nb})_n\mathrm{O}_{3n+2}$ series with $n = 4.5$, 5, or 6 have demonstrated that these compounds have either an orthorhombic symmetry or a monoclinic symmetry, the latter giving rise to pseudo-merohedral twinning (Nanot et al.; 1979, 1983). In particular for the compound $\mathrm{Ca}_5(\mathrm{Nb}_4\mathrm{Ti})\mathrm{O}_{17}$ $(n = 5)$, monoclinic symmetry was established with $P2_1$ and $P2_1/c$ as possible spacegroups. Apparent orthorhombic symmetry, as revealed by precession photographs, occurs because of the relative shift of neighboring layers by $\mathbf{a}_p/2$, where a_p is the lattice constant of a hypothetical undistorted perovskite type structure. Lattice parameters for this compound were reported as: $a \approx 2a_p$, $b \approx 2^{1/2}\mathrm{a}_p$, $c \approx 2^{1/2}6\mathrm{a}_p$. Their study, however, did not involve structure refinements and a crystal structure was not reported. More re-

cently, single-crystal x-ray diffraction studies have been reported on a series of similar compounds, now involving complete structure refinements. These include $SrNbO_{3.4}$ ($n = 5$) (Abrahams et al.; 1998), $Sr(Nb_{0.8}Ti_{0.2})O_{3.4}$ ($n = 5$) (Drews et al.; 1996), $SrNbO_{3.5}$ ($n = 4$) (Daniels et al.; 2002), $LaTiO_{3.4}$ ($n = 5$) (Daniels et al.; 2003), $(Na_{0.2}Ca_{0.8})NbO_{3.4}$ ($n = 5$) (Zuniga and Darriet; 2003), and $Ca(Nb_{0.76}Ti_{0.24})O_{3.33}$ ($n = 6$) (Guevarra et al.; 2005a).

A general description and classification of symmetries of the $A_nB_nO_{3n+2}$ type of compounds has been reported by Levin and Bendersky (1999). They discussed a classification scheme that relates the stacking sequences and octahedral tilt to the symmetry of these structures. They suggested that in most of these structures the displacive transition from a high-temperature untilted structure to a low-temperature tilted structure occurs in two stages: untilted $\rightarrow$ $\mathbf{a}^+ \rightarrow$ $\mathbf{a}^+\mathbf{b}$ or $\mathbf{a}^+\mathbf{c}$, with doubling of the a lattice parameter at the final transition. More recently a structural study by transmission electron microscopy on the $Sr_n(Nb,Ti)_nO_{3n+2}$ series with $n = 4$, 4.5, 5, 6, and 7 has been published by Levin et al. (2000). These compounds were reported to undergo commensurate $\rightarrow$ incommensurate phase transitions at temperatures ranging from 150 to 250 °C, with the modulation vector close to $\mathbf{a}^*/2$. A lock-in phase to $\mathbf{a}^*/2$ was only found for the compound with $n = 5$, and the following sequence of phase transitions was established from high temperature to room temperature: $Immm(untilted) \rightarrow Pmnn \rightarrow incommensurate\ phase \rightarrow P2_1/c$. The final monoclinic structure was found to have $a \approx 2a_p$ (7.7Å).

In the present study we report the crystal structure of $Ca_5Nb_5O_{17}$ ($n = 5$) which is a diamagnetic, electrically conducting compound (formal valence $Nb^{4.8+}$, $4d^{0.2}$) (Lichtenberg et al.; 2001). The crystal structure is monoclinic, $P2_1/c$, with the existence of pseudo-merohedral twinning. A twofold superstructure along [100] was found. A detailed description of the deformation of NbO_6 octahedra at different positions in the slab and its possible relation to the electrical properties of the compound is given.

5.2 Experimental

Crystals of $Ca_5Nb_5O_{17}$ were prepared from $CaCO_3$, Nb_2O_5, and Nb as starting materials and by subsequent floating-zone melting in argon as reported by Lichtenberg et al. (2001). The actual composition determined by thermogravimetric oxidation

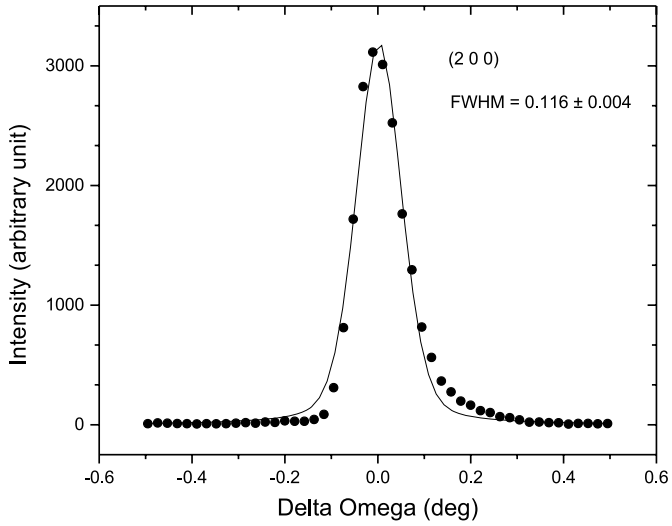

Figure 5.1: Sample rocking curve for the 2 0 0 reflection. The data points were fitted by using the computer program Microcal Origin (Microcal Software; 1997).

was found to be $Ca_5Nb_5O_{17.05} = CaNbO_{3.41}$. This is within one standard uncertainty of the nominal composition since the accuracy of the oxygen content was found to be about 0.3% (Lichtenberg et al.; 2001). It was reported that for this compound the structure type ($n = 5$) remains unchanged in the homogeneity range $3.40 \leq x \leq 3.42$, as revealed by X-ray powder difraction, transmission electron microscopy, and thermogravimetry (Lichtenberg et al.; 2001).

Several crystals were prepared for X-ray diffraction by breaking them off a large aggregate and gluing them to glass fibers. Because of its layered structure, very thin plates of the sample were obtained by this method. The crystals were tested for quality on a MAR345 IP diffractometer and the better ones were subsequently tested on a Nonius MACH3 diffractometer with rotating-anode generator using molybdenum radiation. Several good-quality single-crystals were found, the best one having relatively sharp reflection profiles with a full-width at half-maximum (FWHM) less than 0.2° in ω-scans, which is still larger than the instrumental resolution of about 0.1°(Fig. 5.1). Omega scans for different psi values showed that the profiles for each reflection are almost the same, thus confirming the good quality of the crystal.

Lattice parameters were determined from the setting angles of 25 reflections,

with $40.0° \leq 2\Theta \leq 52.2°$, in four orientations as measured on the Nonius MACH3 diffractometer using the SET4 centering routine (Enraf-Nonius; 1989)(Table 5.1). Owing to the weakness of the superstructure reflections (h = odd) and the long time required for data collection due to the large unit cell of the compound, measurements using the MACH3 diffractometer were deemed ineffective to produce the information necessary to carry out structure determination. Therefore an X-ray diffraction experiment at room temperature was carried out using synchrotron radiation at beamline F1 of Hasylab at DESY in Hamburg, Germany. The experiment used a Huber diffractometer with Kappa geometry and a CCD area detector (Bruker SMART 1000). Data collection was performed using the SMART (v.5.618) software (Bruker; 1998b). A wavelength of $\lambda = 0.7100(2)$Å was chosen in order to minimize absorption and to allow a reasonable portion of the reciprocal space to be measured. The detector was set to a distance of 60 mm from the crystal, while the fine-slicing technique was employed to collect the images with a step-size of 0.1° for omega scans and phi scans. The data collection was strategized using the computer program ASTRO (v.5.0.07) (Bruker; 1998a) for optimal coverage and redundancy in consideration of the coupled limits of the motors driving the circles of the diffractometer. A total of 16 runs were measured with detector offsets of 20° and 45° for measurement of the low-angle and high-angle reflections, respectively, plus an intermediate detector offset of 30° to complete the coverage. Exposure times per frame were 4 s and 8 s, for the low-angle and high-angle measurements, respectively. A data coverage of 100% in the point group $2/m$ was achieved for a resolution of 0.67Å with maximum 2θ of 71.05 °. The minimum and maximum redundancy were 1 and 17, respectively, with a mean of 8.0. The decay of the primary-beam intensity was corrected using SAPRO (v.1.5.50) (Paulmann; 2002). Diffraction intensities were integrated using SAINT (v.6.2) (Bruker; 2000). An integration box with dimensions $1.1° \times 1.1° \times 0.5°$ was used for the integration using orientation matrices found with the SMART software. Refinement of the orientation matrix was performed during the integration procedure every 200 to 300 frames and global refinement of the cell parameters was done after each integration. Absorption correction and scaling were applied using SADABS (v.2.03) (Sheldrick; 2002) with point symmetry $2/m$. SADABS relies on a sufficiently high redundancy of the data, as was achieved indeed (see above). Before parameter refinement in SADABS, $R_{int} = 0.0773$ and after parameter refinement, $R_{int} = 0.0364$.

Table 5.1: Experimental Details

Crystal Data	
Chemical Formula	$Ca_5Nb_5O_{17}$
Molecular Weight	936.91
Cell Setting, Spacegroup	Monoclinic, $P2_1/c$ (No. 14)
a, b, c (Å)	7.7494(3), 5.4928(1), 32.241(1)
β (°)	96.809(4)
V (Å^3), Z	1362.7(1), 4
D_{calc} (Mg/mm^3), μ (mm^{-1})	4.5653(3), 5.836
Crystal Size (mm^3)	$0.13 \times 0.08 \times 0.03$
Crystal Color, Shape	Dark-blue, irregular plate-like
Data Collection	
Radiation	Synchrotron
Wavelength (Å)	0.7100(2)
Temperature (K)	295
Diffractometer	Huber Kappa Diffractometer
Detector	CCD: Bruker SMART1000
Range of h, k, l	$-11 \rightarrow 11, -8 \rightarrow 8, -52 \rightarrow 52$
Maximum 2θ	71.05°
No. of Reflections (obs/all)	25839/ 31864
Criterion for Observed	$I > 3\sigma$
No. of Unique Reflections (obs/all)	4719/ 5427
R_{int} (obs/all)	0.0352/ 0.0355
Absorption Correction	Multi-scan(SADABS 2.03) Sheldrick (2002)
Refinement	
Refinement on	F
Weighting Scheme	$w = 1/[\sigma^2(\|F\|) + (0.01\ \|F\|)^2]$
$(\Delta/\sigma)_{max}$	0.001
No. of Parameters	249
R_F (obs/all)	0.0247/ 0.0296
wR_{F^2} (obs/all)	0.0318/ 0.0330
Goodness of Fit (obs/all)	1.76/ 1.70
Twinvol(II)	0.0272(3)
Extinction Correction	Isotropic, Gaussian Becker and Coppens (1974)
Extinction Coefficient	0.014(2)
$\Delta\rho_{min}/\Delta\rho_{max}$ (e/Å^3)	-1.98/2.95

The diffraction patterns reveals weak h = odd reflections. Analysis of the systematic absences in the reflections using SIR2002 (Burla et al.; 2003) led to $P2_1$ and $P2_1/c$ as possible spacegroups. Reflections at different psi-values were averaged together with symmetry equivalent reflections (point group $2/m$) employing JANA2000 (Petricek et al.; 2000). A good agreement with R_{int} = 0.0352 for 4719 unique observed reflections was obtained (Table 5.1). The diffraction pattern also shows an apparent orthorhombic symmetry. In fact, the transformation $\mathbf{a}_o = \mathbf{a}_m$, $\mathbf{b}_o = \mathbf{b}_m$, $\mathbf{c}_o = \mathbf{a}_m + \mathbf{2c}_m$ of the primitive monoclinic unit cell results in a B-centered unit cell that is orthorhombic within experimental resolution. Orthorhombic symmetry was considered by an additional run of SADABS employing point symmetry mmm. After parameter refinement, R_{int} = 0.1010 was obtained. Averaging in mmm led to R_{int} = 0.0377, slightly but clearly higher than R_{int} for Laue symmetry $2/m$. The deviation from orthorhombic symmetry is mainly due to the superlattice formation: R_{int} = 0.179 for reflections h = odd, while R_{int} = 0.036 for reflections with h = even. In the case of $2/m$, R_{int} = 0.045 for reflections h = odd, while R_{int} = 0.034 for reflections with h = even.

The structure of $LaTiO_{3.41}$ was used as starting model (Daniels et al.; 2003). The structure was refined using JANA2000. Initial refinements in $P2_1/c$ converged at R_F=0.0318 and wR_{F^2}=0.0542 for observed reflections. However, there were reflections violating the systematic absences for the c-glide plane. An improved fit to the diffraction data was obtained by the introduction of pseudo-merohedral twinning, assuming a twin law corresponding to a 2-fold axis along **a**, resulting in the superposition of reflections $(h\ k\ l)_I$ and $(h\ \text{-}k\ \text{-}(h + l))_{II}$ of the respective twin domains (Fig. 5.2). Levin and Bendersky (1999) in a transmission electron microscope study have reported the presence of twin-related monoclinic variants for the n = 5 type of the $Sr_n(Nb,Ti)_nO_{3n+2}$ series while complete structure refinements using this twin model have also been been reported in similar perovskite-related compounds (Zuniga and Darriet; 2003; Guevarra et al.; 2005a). Using this twin model, reflections of type $(h0l)$ where h=odd and l=odd which were found to violate the c-glide plane are now accounted for by the second twin domain (h=odd,0,l=even). The final refinement with all atoms refined anisotropically converged at R_F=0.0247 and wR_{F^2}=0.0318 (Table 5.1). Further details of the crystal structure investigation(s) can be obtained from the Fachinformationszentrum Karlsruhe, 76344 Eggenstein-Leopoldshafen, Germany, (fax: (49) 7247-808-666; e-mail:

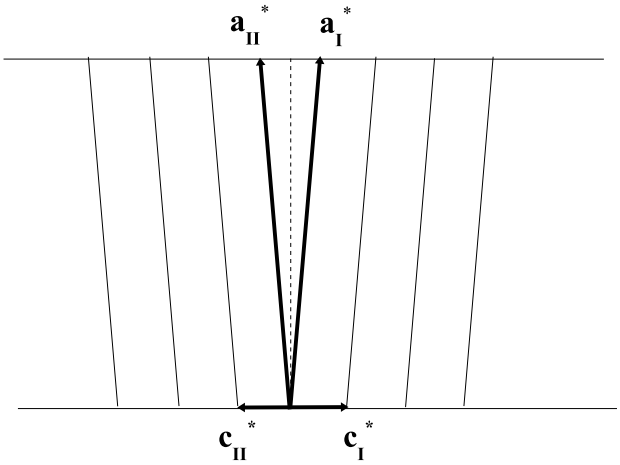

Figure 5.2: Orientation of the two twin domains in reciprocal space in the case of pseudo-merohedral twinning of the crystal: $(h\ \ k\ \ l)_I = (h\ \text{-}k\ \text{-}(h+l))_{II}$.

crysdata@fiz.karlsruhe.de) on quoting the depository number CSD 415450.

5.3 Discussion

The accurate crystal structure of $Ca_5Nb_5O_{17}$ has been determined from single-crystal x-ray diffraction. Only an accurate crystal structure provides quantitatively correct information on the tilting and deformations of the octahedra at different sites in the slabs. As we show below, this information provides insight in the structural and physical properties of the compound.

Fractional atomic coordinates and equivalent isotropic displacement parameters are summarized in Table 5.2. Projections of the structure along the **a** and **b** directions are shown in Fig. 5.3. Successive slabs of octahedra stacked along the **c**-axis are shown to be shifted by $\mathbf{a}/2$. The tilt pattern of the NbO_6 octahedra with respect to the untilted orthorhombic structure is described in Fig. 5.4. It is clear that the octahedra exhibit tilting about the **a**-axis (about $\mathbf{a}^*$ in the present study)(Fig. 5.4*a*). This kind of tilt is described as an $\mathbf{a}^+$ tilt as the octahedra *along* the rotation axis are tilted in the same sense (Levin and Bendersky; 1999). Neighboring octahedra along the **a**-axis also exhibit antiphase tilts *about* the **c**-axis (about $\mathbf{c}^*$ in the present study), i.e. consecutive octahedra are rotated clockwise and anticlockwise along the

Table 5.2: Fractional Atomic Coordinates and Equivalent Isotropic Atomic Displacement Parameters (Å^2) of $Ca_5Nb_5O_{17}$

Atom[a]	x	y	z	U_{eq}
Ca1	0.25442(4)	0.50567(6)	0.00643(7)	0.0063(1)
Ca2	0.29938(4)	0.99595(6)	0.09547(8)	0.0045(0)
Ca3	0.79172(5)	0.00012(7)	0.08310(1)	0.0088(1)
Ca4	0.31644(5)	0.52001(7)	0.20820(1)	0.0103(1)
Ca5	0.13777(4)	0.08703(6)	0.27833(1)	0.0053(0)
Nb1	0.5	0	0	0.0018(0)
Nb2	0	0	0	0.0017(0)
Nb3	0.54317(2)	0.50348(2)	0.09191(0)	0.0021(0)
Nb4	0.04897(2)	0.50462(2)	0.09114(0)	0.0019(0)
Nb5	0.08599(2)	0.02596(3)	0.17709(0)	0.0027(0)
Nb6	0.59517(2)	0.03031(3)	0.17815(0)	0.0027(0)
O1	0.5559(1)	0.2934(2)	0.0343(0)	0.0057(3)
O2	0.9784(1)	0.2942(2)	0.0344(0)	0.0062(3)
O3	0.4867(1)	0.7895(2)	0.0514(0)	0.0056(3)
O4	0.0650(1)	0.7900(2)	0.0512(0)	0.0059(3)
O5	0.0772(1)	0.2952(2)	0.2103(0)	0.0065(3)
O6	0.6365(1)	0.3189(2)	0.2032(0)	0.0077(3)
O7	0.1352(1)	0.8046(2)	0.2198(0)	0.0053(3)
O8	0.5930(1)	0.8238(2)	0.2242(0)	0.0060(3)
O9	0.0350(1)	0.1869(2)	0.1183(0)	0.0053(3)
O10	0.5827(1)	0.1836(2)	0.1175(0)	0.0045(3)
O11	0.3358(1)	0.0900(2)	0.1693(0)	0.0064(3)
O12	0.1649(1)	0.4280(2)	0.3309(0)	0.0064(3)
O13	0.1247(1)	0.7050(2)	0.1354(0)	0.0068(3)
O14	0.5115(1)	0.7019(2)	0.1366(0)	0.0067(3)
O15	0.7941(1)	0.5631(2)	0.0888(0)	0.0084(3)
O16	0.2897(1)	0.4140(2)	0.0792(0)	0.0043(3)
O17	0.7517(1)	0.9206(2)	0.0039(0)	0.0064(3)

[a]All atoms are in general positions except Nb1 and Nb2, which are in special positions with multiplicity 0.5

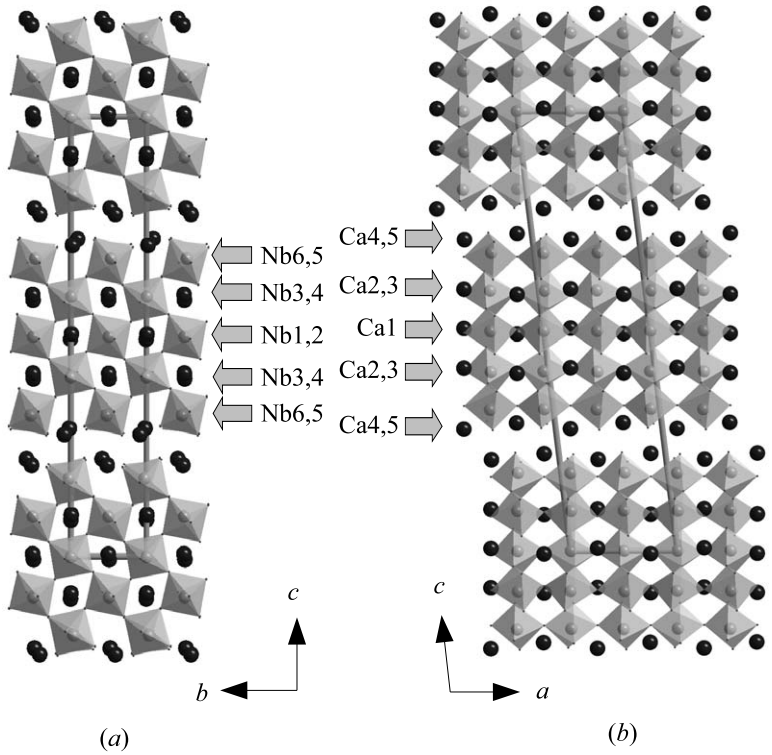

Figure 5.3: Projections of the structure of $Ca_5Nb_5O_{17}$ along (*a*) the **a** and (*b*) the **b** directions. Large dark spheres represent Ca atoms while the NbO_6 octahedra are outlined.

a-axis (Fig. 5.4*b*). It was reported that the effect of a **c** tilt leads to a doubling of the *a* lattice parameter (Levin and Bendersky; 1999; Glazer; 1975). Thus the tilt pattern observed in the present case is a combination of tilts, $\mathbf{a}^+\mathbf{c}$. Such tilting modes have also been registered for the $n = 5$ member of the $Sr_n(Nb,Ti)_nO_{3n+2}$ series and have been attributed to the sequence of symmetry transformations: $Immm(untilted) \rightarrow Pmnn \rightarrow \ incommensurate \ \ phase \rightarrow \ P2_1/c$ (Levin et al.; 2000). The topology of the structure and the tilt system of the octahedra for the present compound indeed corresponds to that expected for a structural motif composed of an odd number of layers of octahedra. Similar topology has been reported for other perovskite-related $n = 5$ type compounds (Daniels et al.; 2003; Zuniga and Darriet; 2003).

The interatomic distances show that the Ca atoms at the borders of the slabs (Ca4,Ca5) are less than 12-fold coordinated by oxygen, while the coordination of Ca atoms embedded within the slabs (Ca1,Ca2,Ca3) can be described by a distorted cuboctahedron, as it would be expected for a perovskite-type structure, in agreement

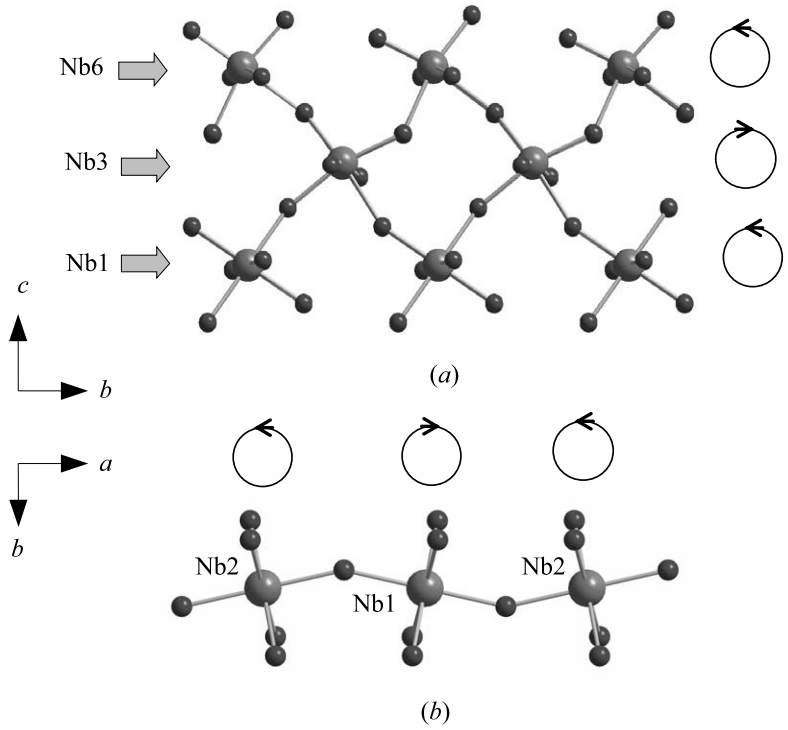

Figure 5.4: NbO_6 octahedra tilting about (*a*) $\mathbf{a}^*$ and (*b*) $\mathbf{c}^*$ in $Ca_5Nb_5O_{17}$. Also shown are the sense of tilt of the octahedra.

with coordinations in similar layered perovskites (Drews et al.; 1996; Daniels et al.; 2002, 2003; Zuniga and Darriet; 2003; Guevarra et al.; 2005a). Ca4 is coordinated by 10 oxygen atoms with Ca–O bond distances ranging from 2.411(1) Å to 3.369(1) Å, while Ca5 has 7 coordinating oxygen atoms with bond distances from 2.309(1) Å to 2.518(1) Å. Ca1, Ca2, and Ca3 are bonded to 12 oxygen atoms with bond lengths ranging from 2.302(1) Å to 3.403(1) Å. As shown in Fig. 5.5, Ca5, which is located at the borders of the slabs, is displaced out of the center of the coordinating polyhedra towards the neighboring slab, while Ca1 and Ca3, which are embedded within the slabs, exhibit a distorted cuboctahedron coordination. The deviation of Ca5 from the center of its coordinating polyhedra toward the interlayer regions is consistent with local charge neutrality as there are excess oxygen atoms in these regions. For the Ca atoms within the slabs, the distortion follows from the slight shift of the Ca atoms from the centers of the coordinating cuboctahedra.

The distortions of the NbO_6 octahedra can be described in terms of the Nb–O

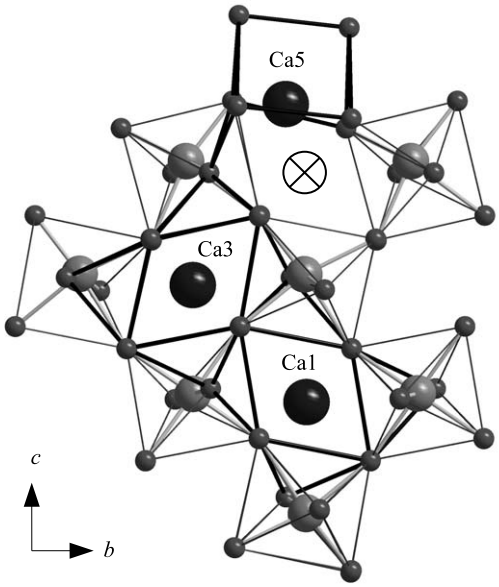

Figure 5.5: Coordination of Ca atoms. Ca1 is in the middle of the slabs while Ca5 is at the border. The dark lines between the O atoms are only a means to clarify the coordination geometries and do not represent chemical bonds. The symbol ⊗ marks the position that Ca5 would occupy in a 12-fold coordination.

bond lengths and the O–Nb–O bond angles. Fig. 5.6 shows that different Nb sites have different ranges of Nb–O bond lengths. It is clear that the spread in bond lengths around Nb and the deviation of each Nb–O distance from the mean value per Nb site, which is about 2Å, increases from the center to the borders of the slabs. This variation in bond lengths represents a variation of distortion of NbO_6 octahedra. A measure for the size of the octahedral distortion is the distortion index, $[\max(d[\mathrm{Nb}-\mathrm{O}]) - \min(d[\mathrm{Nb}-\mathrm{O}])]/\mathrm{ave}(d[\mathrm{Nb}–\mathrm{O}])$ (Lichtenberg et al.; 2001), which is large at the borders and small in the middle of the slabs (Fig. 5.7). The large distortion of octahedra at the borders of the slabs (Nb5,Nb6) can be attributed to the elongation of some Nb–O distances (e.g. d[Nb5–O13]=2.256(1) Å and d[Nb6–O14]=2.293(1) Å). This is also reflected by the relatively large displacement parameters of Nb5 and Nb6 as compared to other Nb sites in the slabs, which manifests a stretching of the octahedra into the interlayer regions. With respect to the mean O–Nb–O bond angles, there are no significant differences among the different Nb sites (Table 5.3). The standard uncertainty of the mean, however, increases from

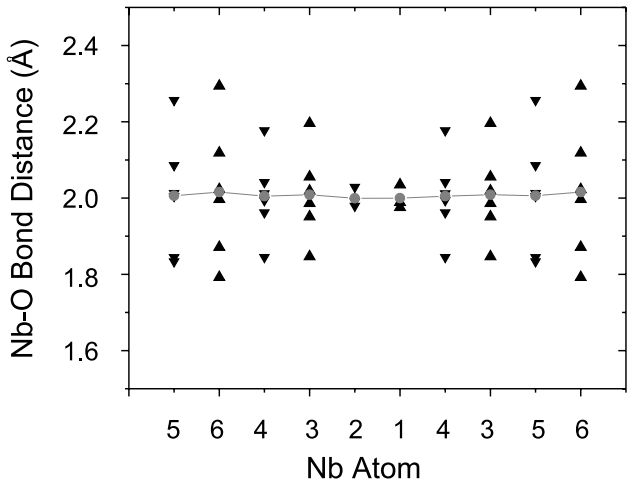

Figure 5.6: Bond distances between different Nb atoms and their coordinating O atoms. The Nb atoms are arranged such that the center of the horizontal axis of the graph corresponds to the center of the slab. The symbol ▲ corresponds to Nb atoms on one row along the **c**-axis while the symbol ▼ refers to a second row displaced by **a**/2. The symbol • denotes the mean Nb–O distance.

the center to the borders of the slab. Thus, the distortion of the NbO_6 octahedra in terms of bond-length and bond-angle grows from the center to the borders of the slabs in agreement with previous studies on related layered perovskites (Drews et al.; 1996; Daniels et al.; 2002, 2003; Zuniga and Darriet; 2003; Guevarra et al.; 2005a).

Bond-valence sums (Brese and O'Keeffe; 1991) were computed for all different Nb sites in the slab (Fig. 5.8). The valence of Nb is close to 5.0 v.u.(valence units) [4.953(1)–4.984(1) v.u.] at the borders of the slabs, and it decreases towards the center of the slabs. The smaller valence at the center of the slabs [4.730(1)–4.733(1) v.u.] indicates that the extra electrons in the $4d$ orbitals of Nb are most probably accommodated at Nb sites in the middle of the slabs. This implies that the electrical conduction in this compound takes place in the middle of the slabs where the NbO_6 octahedra are least distorted. Angle-resolved photoemission studies (ARPES) and band-structure calculations on $Sr_5Nb_5O_{17}$ ($n = 5$) have concluded that the predominant contribution to the occupied electron density of states at the Fermi energy comes from the least distorted octahedra which are found in the middle of the

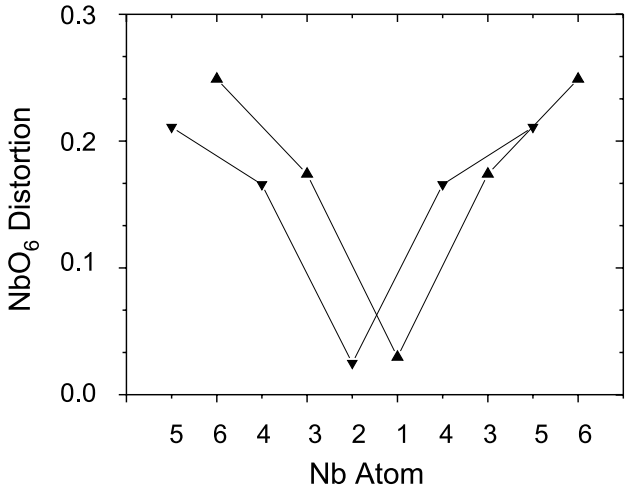

Figure 5.7: NbO_6 octahedral distortion. The Nb atoms are arranged such that the center of the horizontal axis of the graph corresponds to the center of the slab. The symbol ▲ corresponds to Nb atoms on one row along the **c**-axis while the symbol ▼ refers to a second row displaced by **a**/2.

slabs (Kuntscher et al.; 2000, 2002, 2004). In the insulator $Ca(Nb,Ti)O_{3.33}$ of type $n = 6$ with exclusively Nb^{5+} and Ti^{4+}, there is a similar trend of charge distribution as indicated by the experimentally determined site occupancies of the B cations, Nb and Ti (Guevarra et al.; 2005a). In this compound, the borders of the slab are filled almost entirely by Nb^{5+} while at the center of the slab, the largest amount of substitution of Nb^{5+} by Ti^{4+} is found. On the other hand, in $Ca_5Nb_5O_{17}$, the borders of the slabs are also occupied by Nb^{5+} but in the center of the slab the Nb ions have smaller fractional charge. It is interesting to note that on the basis of a crystal structure analysis, one is able to obtain information about the charge distribution of the B cations along the slabs of the octahedra.

The unit cell volume of monoclinic $Ca_5Nb_5O_{17}$ is approximately twice as large as that of $Sr_5Nb_5O_{17}$ which was reported to have orthorhombic symmetry (Abrahams et al.; 1998). With respect to the distortions of the NbO_6 octahedra, there are no fundamental differences between the two structures for similar Nb sites (Table 5.4). The differences between the two structures are in the tilting of the NbO_6 octahedra and concomitantly in the coordinations of the Ca and Sr atoms, respectively. Fig. 5.9 shows the coordination of Ca2 in $Ca_5Nb_5O_{17}$ and Sr3 in $Sr_5Nb_5O_{17}$, both are located

Table 5.3: Mean O–Nb–O Bond Angles (°) in $Ca_5Nb_5O_{17}$ ($n = 5$)

O–Nb1–O	90.00 (47)
O–Nb2–O	90.00 (46)
O–Nb3–O	89.64 (200)
O–Nb4–O	89.70 (184)
O–Nb5–O	89.69 (210)
O–Nb6–O	89.57 (222)

Table 5.4: Range of Nb–O Bond Distances (Å) and Mean O–Nb–O Bond Angles (°) in $Sr_5Nb_5O_{17}$ Abrahams et al. (1998)[b]

Nb1–O	1.973 (3) − 2.034(3)
Nb3–O	1.842 (3) − 2.170(3)
Nb2–O	1.815 (3) − 2.280(3)
O–Nb1–O	90.00 (36)
O–Nb3–O	89.73 (176)
O–Nb2–O	89.63 (201)

[a]The Nb atoms are arranged from the center (Nb1) to the border (Nb2) of the slabs.

[b]The Nb atoms are arranged from the center (Nb1) to the border (Nb2) of the slabs.

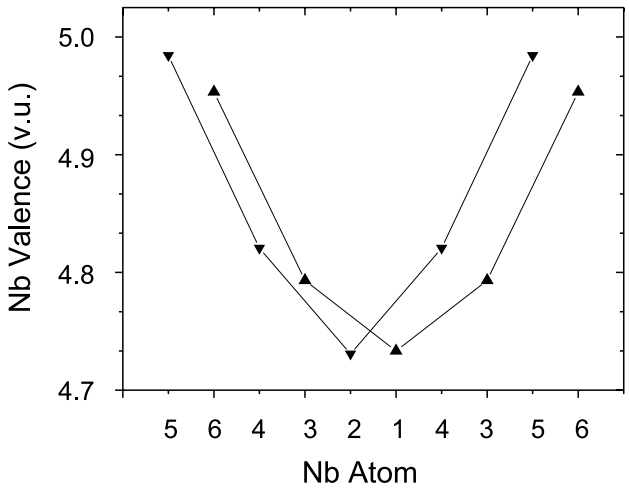

Figure 5.8: Nb valence for the different Nb sites in the octahedral slab. The Nb atoms are arranged such that the center of the horizontal axis of the graph corresponds to the center of the slab. The symbol ▲ corresponds to Nb atoms on one row along the **c**-axis while the symbol ▼ refers to a second row displaced by **a**/2.

intermediate between the center and the borders of their respective slabs. While in $Sr_5Nb_5O_{17}$ Sr3 occupies the center of the coordinating cuboctahedron, Ca2 in $Ca_5Nb_5O_{17}$ is shifted away from the center of the coordinating polyhedra. The shift of Ca2 is accompanied by rotations of the octahedra as allowed by the lower monoclinic symmetry found for $Ca_5Nb_5O_{17}$. The superstructure, which was not found in $Sr_5Nb_5O_{17}$, is manifested in an unusually high valence of Ca2 (2.236(1) v.u.) in $Ca_5Nb_5O_{17}$ which suggests a residual compressive strain. This local strain, in turn, is relieved by a commensurate modulation of the structure leading to a twofold superstructure along [100], as presently found for $Ca_5Nb_5O_{17}$. The different sizes and strengths of interactions of Ca versus Sr may result in the superstructure to appear in $Ca_5Nb_5O_{17}$ and not to appear in $Sr_5Nb_5O_{17}$. But it may also be that a similar superstructure does indeed exist in $Sr_5Nb_5O_{17}$, and that this was not detected (Abrahams et al.; 1998). An investigation is in progress to clarify this issue.

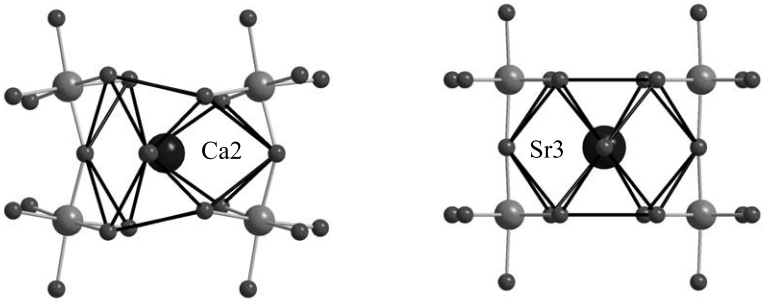

(*a*) (*b*)

Figure 5.9: Coordination of (*a*) Ca2 in $Ca_5Nb_5O_{17}$ viewed along $\mathbf{c}^*$, and (*b*) Sr3 in $Sr_5Nb_5O_{17}$ viewed along $\mathbf{a}^*$. The view directions relative to the topology are the same in both cases; only the unit-cell settings are different.

5.4 Conclusions

The crystal structure at room temperature of $Ca_5Nb_5O_{17}$ has been successfully determined by single-crystal X-ray diffraction with synchrotron radiation. This compound is an $n = 5$ member of the series $A_nB_nO_{3n+2}$ (A = Ca, Sr or La and B = Ti or Nb). It consists of perovskite-like slabs, which are five NbO_6 octahedra wide separated by an interslab region, where the octahedra on opposite sides of the gap do not share oxygen atoms resulting into an extra layer of oxygen atoms with respect to the ideal perovskite structure. The topology of the structure and the tilt system of the octahedra corresponds to that expected for a structural motif with $n = 5$ layers of octahedra. The structure is monoclinic ($P2_1/c$) with a twofold superstructure along [100]. The Ca atoms near the borders of the slabs have irregular coordination geometry with 7 coordinating oxygen atoms, while the coordination of Ca atoms within the slabs can be described by a distorted cuboctahedron. The NbO_6 octahedra at the center of the slabs are much less distorted than those at the borders of the slabs. The computed valences for Nb suggests that the electrical conduction in this compound takes place predominantly in the middle of the slabs.

Chapter 6

Perovskite-related $Ca(Nb,Ti)O_{3.33}$

Abstract

Crystals of nominal composition $Ca(Nb_{0.8}Ti_{0.2})O_{3.4}$, an $n = 5$ member of the homologous series $A_nB_nO_{3n+2}$, have been synthesized by floating-zone melting (Lichtenberg et al.; 2001). The material was found to be multiphase consisting also of the $n = 6$ type. A good single crystal of this $n = 6$ type was found and the crystal structure at room temperature was determined by X-ray diffraction using synchrotron radiation. Structure refinements indicate a composition of $Ca(Nb_{0.76}Ti_{0.24})O_{3.33}$. The crystal structure is monoclinic $P2_1$ and consists of slabs of corner-sharing $(Nb,Ti)O_6$ octahedra interrupted by layers of oxygen atoms. Ca atoms within the slabs are 12-fold coordinated whereas those at the borders show irregular coordination geometries. The octahedral distortion is greatest near the borders of the slabs and least near the middle of the slabs. Ti^{4+} preferentially occupy octahedral sites in the middle of slabs. The non-stoichiometry in the refined composition and the insulating character of the material may be explained in terms of extra oxygen, vacancies on the cation sites, or by localization of the electrons in the $4d$ orbitals of Nb at the borders of slabs.

6.1 Introduction

The homologous series $A_nB_nO_{3n+2}$ (A = Ca, La or Sr and B = Ti or Nb) with n = 4, 4.33, 4.5, 5, and 6 is interesting, because these compounds exhibit special

physical and electronic properties. Some of these materials are high-T_c ferroelectrics, while others are quasi-1D metals, which show a metal-semiconductor transition at low temperatures (Lichtenberg et al.; 2001; Kuntscher et al.; 2002, 2004). The latter is discussed in terms of a Peierls transition and charge-density wave but their occurrence has not yet been definitely established (Kuntscher et al.; 2002, 2004; Weber et al.; 2001). Another interesting feature in some of these compounds is given by the possibility to realize an intrinsic coexistence of a high dielectric polarizability and a metallic conductivity (Lichtenberg et al.; 2001; Kuntscher et al.; 2002, 2004).

The basic crystal structures of compounds $A_nB_nO_{3n+2} = ABO_{3+x}$ ($x = 2/n$) can be described as the alternate stacking of slabs of ABO_3, with the perovskite structure type, and layers of additional oxygen (Fig. 6.1) (Levin and Bendersky; 1999). The slabs are n octahedra thick and they are stacked along [110] of the perovskite structure type (along $\mathbf{c}^*$ in the present study). Neighboring slabs are displaced with respect to each other over half the body diagonal of an octahedron, resulting in an irregular coordination of the A cations at the borders of the slabs. Non-integral values of n indicate ordered sequences of octahedral slabs with alternating thicknesses, e.g. $n = 4.5$ corresponds to alternating slabs of four and five octahedra thick layers.

Single-crystals of $A_nB_nO_{3n+2}$ type compounds are difficult to grow, while powder diffraction does not provide sufficient resolution for structure refinements. Therefore, initial structural studies of these compounds mainly reported the building principles without atomic positions or the tilting of the octahedra (Nanot et al.; 1979, 1983). More recently complete structure refinements have been made for several compounds at various levels of accuracy. They include $SrNbO_{3.4}$ ($n = 5$) (Abrahams et al.; 1998), $Sr(Nb_{0.8}Ti_{0.2})O_{3.4}$ ($n = 5$) (Drews et al.; 1996), $SrNbO_{3.5}$ ($n = 4$) (Daniels et al.; 2002), $LaTiO_{3.4}$ ($n = 5$) (Daniels et al.; 2003) and $(Na_{0.2}Ca_{0.8})NbO_{3.4}$ ($n = 5$) (Zuniga and Darriet; 2003). In the present study we report the crystal structure of $Ca(Nb_{0.76}Ti_{0.24})O_{3.33}$ ($n = 6$), including a detailed description of the deformations of the octahedra, the Ca environments and the Nb,Ti ordering.

Based on x-ray powder diffraction, $Ca(Nb_{0.8}Ti_{0.2})O_{3.33}$ ($n = 6$) was previously proposed to be orthorhombic (Lichtenberg et al.; 2001). However, an earlier study had already found that the Ca-based niobates and titanates are monoclinic, despite a pseudo-orthorhombic lattice (Nanot et al.; 1979, 1981). Space groups $P2_1$ and $P2_1/c$ were proposed as possible symmetries for the compounds $Ca(Nb_{0.8}Ti_{0.2})O_{3.4}$ ($n = 5$) and $Ca(Nb_{0.67}Ti_{0.33})O_{3.33}$ ($n = 6$), but structure refinements were not

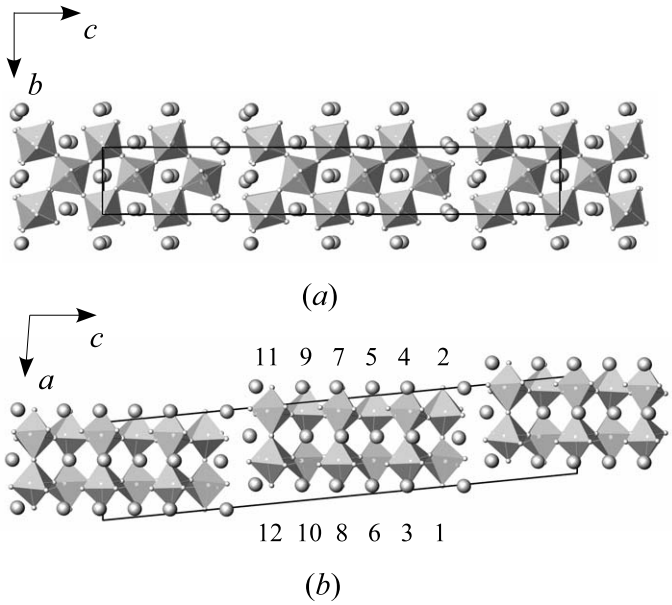

Figure 6.1: Projections of the structure of $Ca(Nb_{0.76}Ti_{0.24})O_{3.33}$ along (*a*) the [100] and (b) the [010] direction. Large spheres represent Ca atoms while small spheres represent O atoms. The $(Nb,Ti)O_6$ octahedra are outlined. Neighboring slabs of octahedra are displaced with respect to each other by about half of the octahedron body diagonal. The numbering of (Nb,Ti) sites in (*b*) corresponds to those in in Figures 4, 5, 6 and 7.

presented (Nanot et al.; 1979, 1981). The apparent orthorhombic symmetry was attributed to pseudo-merohedral twinning. In the present study $Ca(Nb_{0.76}Ti_{0.24})O_{3.33}$ ($n = 6$) is found to be monoclinic $P2_1$, and the crystal appeared to be twinned indeed. The accurate crystal structure of $Ca(Nb_{0.76}Ti_{0.24})O_{3.33}$ reveals a clear correlation between Nb,Ti site occupancies, deformations of the $(Nb,Ti)O_6$ octahedra, and the relative positions of the octahedra within the slab.

6.2 Experimental

Crystals of nominal composition $Ca(Nb_{0.8}Ti_{0.2})O_{3.4}$ were prepared by using $CaCO_3$, Nb_2O_5 and TiO_2 as starting materials and by subsequent floating-zone melting in air as reported by Lichtenberg et al. (2001). Several crystals were prepared for X-ray diffraction by breaking them off a large aggregate and gluing them to glass fibers. The crystals were tested for quality on a MAR345 IP diffractometer and the better

ones subsequently on a Nonius MACH3 diffractometer with rotating-anode generator. In the course of crystal testing, it was found that the as-grown compositions $Ca(Nb_{0.8}Ti_{0.2})O_{3.4}$ consists of more than one phase including an $n = 6$ type compound which has an ideal oxygen content of $x = 1/3$ in $Ca(Nb,Ti)O_{3+x}$. Multiple phases in some compositions of $A_nB_nO_{3n+2}$ were already reported by Lichtenberg *et al.* (Lichtenberg et al.; 2001). Several good quality single crystals from the $n = 6$ type phase were found. The best crystal had relatively narrow reflection profiles with a full-width at half-maximum (FWHM) less than 0.2 ° in an ω-scan which is still larger than the instrumental resolution of about 0.1 °.

Lattice parameters were determined from the setting angles of 25 reflections in four orientations as measured on the Nonius MACH3 diffractometer (Table 6.1). Owing to the weakness of the superstructure reflections (h = odd) and the long time required for data collection due to the large unit cell of the compound, measurements using the MACH3 diffractometer were deemed ineffective to produce the information necessary to carry out structure determination. Therefore an X-ray diffraction experiment at room temperature was performed using synchrotron radiation at beamline F1 of Hasylab at DESY in Hamburg, Germany. The experiment used a Huber diffractometer with Kappa geometry and a CCD area detector (Bruker SMART 1000). The data collection was done with the SMART (v.5.618) software (Bruker; 1998b) and was strategized using the computer program ASTRO (v.5.0.07) (Bruker; 1998a) for optimal coverage and redundancy. The diffraction intensities were integrated using the computer program SAINT (v.6.2) (Bruker; 2000). Absorption correction and scaling were applied using the computer program SADABS (v.2.03) (Sheldrick; 2002) with point symmetry 2. The result was a reflection file containing the integrated intensities of 24459 reflections (Table 5.1).

Reflections at different psi-values were averaged together with symmetry equivalent reflections (point group 2) employing the computer program JANA2000 (Petricek et al.; 2000). A good agreement with $R_{int} = 0.031$ for 5577 unique observed reflections was obtained (Table 5.1). The transformation $\boldsymbol{a_o} = \boldsymbol{a_m}$, $\boldsymbol{b_o} = \boldsymbol{b_m}$, $\boldsymbol{c_o} = \boldsymbol{a_m} + 2\boldsymbol{c_m}$ of the primitive monoclinic unit cell results in a B-centered unit cell that is orthorhombic within experimental resolution. Orthorhombic symmetry was considered by an additional run of SADABS employing point symmetry mmm. However the diffraction data favor Laue symmetry $2/m$, as is shown by $R_{int} = 0.042$ for averaging reflections in mmm. The deviation from orthorhombic symmetry is

Table 6.1: Experimental Details

Crystal Data	
Chemical Formula	$Ca(Nb_{0.76}Ti_{0.24})O_{3.33}$
Cell Setting, Spacegroup	Monoclinic, $P2_1$
a, b, c (Å), $\beta(^\circ)$	7.681(2), 5.465(1), 37.747(6), 95.875(14)
V (Å^3)	1576.1
Z	24
Crystal Size (mm^3)	0.100 x 0.030 x 0.015
Crystal Color	transparent, colorless
Data Collection	
Radiation	Synchrotron
Wavelength(Å)	0.7100(2)
Temperature(K)	295
Diffractometer	Huber Kappa Diffractometer
Detector	CCD: Bruker SMART1000
Range of h, k, l	$-10 \rightarrow 10, -7 \rightarrow 7, 0 \rightarrow 50$
Maximum 2θ	58.14°
No. of Reflections (obs/all)	15639/ 24459
Criterion for Observed	$I > 3\sigma$
No. of Unique Reflections (obs/all)	5577/ 7800
R_{int}(obs/all)	0.0307/ 0.0326
Absorption Correction	Semi-Empirical (SADABS 2.03) (Sheldrick; 2002)
Refinement	
Refinement on	F
Weighting Scheme	$w = 1/[\sigma^2(\|F\|) + (0.01\ \|F\|)^2]$
No. of Parameters	292
R_F(obs/all)	0.0545/ 0.0755
wR_{F^2}(obs/all)	0.0605/ 0.0638
Goodness of Fit(obs/all)	2.45/ 2.17
Twinvol(II)	0.6713(12)
Extinction Correction	Isotropic, Gaussian
Extinction Coefficient	0.0511(36)
Difference Fourier ($\Delta\rho$(min/max))	-1.91/1.79

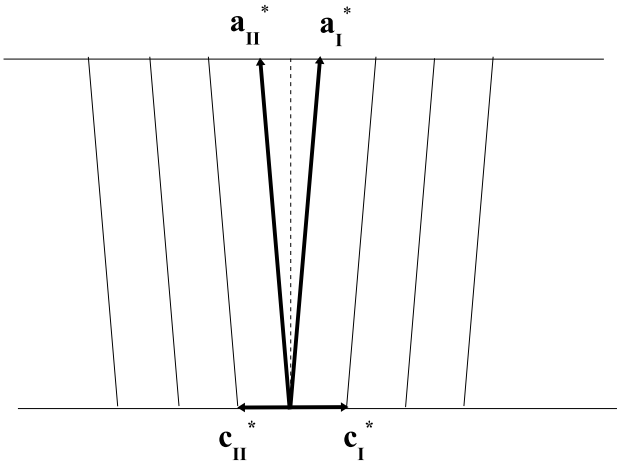

Figure 6.2: Orientation of the two twin domains in reciprocal space in the case of pseudo-merohedral twinning of the crystal: $(h\ \ k\ \ l)_I = (h\ \text{-}k\ \text{-}(h+l))_{II}$.

mainly due to the superlattice formation: $R_{int} = 0.217$ for reflections h = odd, while $R_{int} = 0.035$ for reflections with h = even.

The structure was solved by direct methods employing the computer program SIR2002 (Burla et al.; 2003). Structure refinements were performed with JANA2000 (Petricek et al.; 2000). Nb and Ti atoms disorderly occupy the same sites. Therefore their positional and thermal parameters were constrained to be equal in all refinements. Initial refinements in $P2_1$ converged at R_F=0.0875 and wR_{F^2}=0.1292 for observed reflections but with several atoms having non-positive definite temperature factors. An improved fit to the diffraction data was obtained by the introduction of pseudo-merohedral twinning, assuming a twin law corresponding to a 2-fold axis along **a**, resulting in the superposition of reflections $(h\ k\ l)_I$ and $(h-k-(h+l))_{II}$ of the respective twin domains (Fig. 6.2). The R-values dropped to R_F=0.0500 and wR_{F^2}=0.0541 but non-positive definite values remained for the temperature tensors of several atoms. Examination of the atomic coordinates and site occupancies revealed the presence of a pseudo-inversion center in the structure although all attempts to refine the structure in a centrosymmetric space group had failed. The problems related to correlated parameters and non-positive definite temperature tensors could be resolved by introduction of additional restrictions on the site occupancies and temperature tensors of all atoms according to the pseudo-inversion center. The final structure model, with isotropic temperature parameters for oxy-

gen, resulted in R_F=0.0545 and wR_{F^2}=0.0605, that is only slightly worse than the fit of the free refinement (with all atoms refined anisotropically, R_F= 0.0539 and wR_{F^2}=0.0590 but having several O-atoms with physically meaningless temperature factors). Each Nb site was constrained to be fully occupied by a mixture of Nb and Ti, with amounts of Ti being varied in the refinements. The sum of site occupancies of Nb and Ti then resulted in a chemical composition $Ca(Nb_{0.76}Ti_{0.24})O_{3.33}$. The atomic coordinates and displacement parameters can be found in Appendix E

6.3 Discussion

We have determined the crystal structure of $Ca(Nb_{0.76}Ti_{0.24})O_{3.33}$, an $n = 6$ member of the homologous series $Ca_n(Nb,Ti)_nO_{3n+2}$. Although the topologies of these structures have been known for a long time (Nanot et al.; 1979), precise atomic coordinates are required for a meaningful crystal chemical analysis. As we show below, such an analysis provides clues towards understanding the structural stability of $Ca(Nb_{0.76}Ti_{0.24})O_{3.33}$.

Our study reveals that the Ca atoms have different coordination geometries at different positions in the slab. Interatomic distances show that the Ca atoms near the borders of the slabs (Ca1/Ca12 and Ca2/Ca11) have a coordination number less than the regular 12-fold coordination of a perovskite-type structure. Ca1 and Ca12, are coordinated by 7 oxygen atoms with Ca-O bond distances ranging from 2.278(8) Å to 2.552(8) Å, while Ca2 and Ca11 are coordinated by 10 oxygen atoms with Ca-O bond distances from 2.355(9) Å to 3.453(9) Å. Calcium atoms embedded within the slabs (Ca3 – Ca10) obey the 12-fold coordination with bond lengths from 2.214(9) Å to 3.442(9) Å. Previous studies on similar layered perovskites have shown that the cations (Sr, La, or Ca/Na) in the interlayer sites have less than the 12-fold coordination expected for perovskites, while the coordinations of cations found within the slabs can be described by a distorted cubooctahedron (Drews et al.; 1996; Daniels et al.; 2002, 2003; Zuniga and Darriet; 2003). The atoms Ca1 and Ca12, which are located at the borders of the slabs at $x \approx 0.14$, are displaced towards the neighboring slab out of the 'square' of four nearest O atoms (Fig. 6.3*a* and 6.3*b*), while the atoms Ca2 and Ca11, which are situated at the borders of the slabs at $x \approx 0.63$, are displaced towards the centers of the distorted cubooctahedra

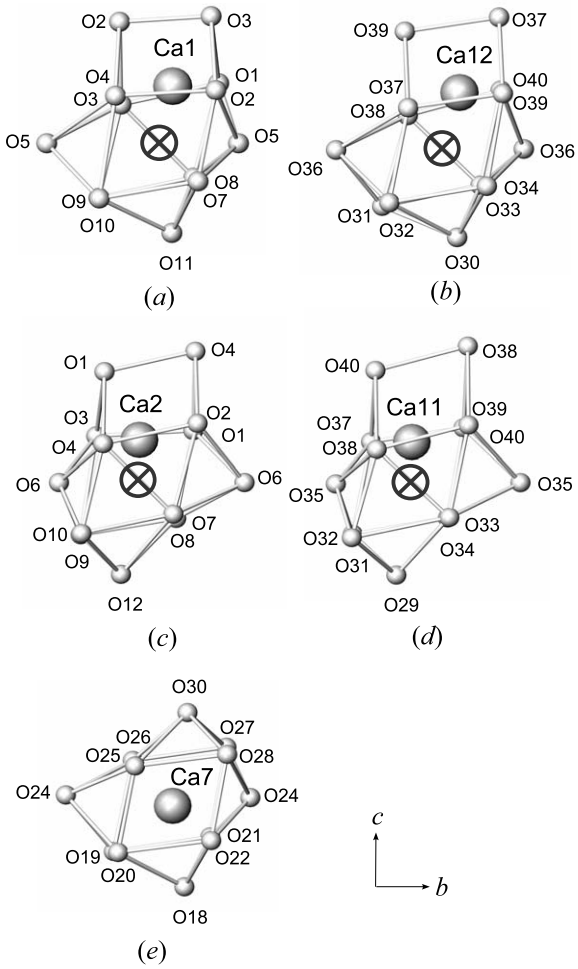

Figure 6.3: Coordination spheres of (*a*) Ca1 and (*b*) Ca12 (Ca atoms near the border of the octahedral slab in one row), (*c*) Ca2 and (*d*) Ca11 (Ca atoms near the border of the octahedral slab in another row) and (*e*) Ca7 (Ca atom at the middle of the octahedral slab). The lines between the O atoms are only a means to clarify the coordination geometries and do not represent chemical bonds. The symbol ⊗ marks the position that Ca would occupy in a 12-fold coordination that corresponds to the situation of Ca7.

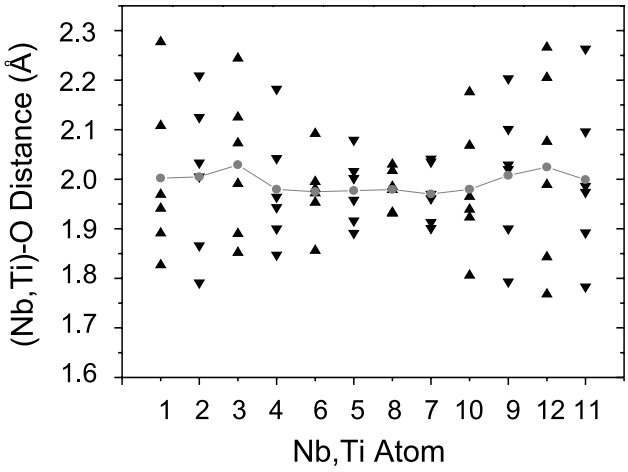

Figure 6.4: Distances between Nb,Ti atom and its surrounding O atoms. The Nb,Ti atoms are arranged according to their positions in the octahedral slab with the center of the graph corresponding to the center of the slab. The symbol ▲ corresponds to Nb,Ti atoms on one row along the c-axis while the symbol ▼ corresponds to those on the other row. The symbol • denotes the mean (Nb,Ti)-O distance.

of the slab they belong to (Fig. 6.3*c* and 6.3*d*). The two situations described above correspond to the two extreme positions at $t = 0$ and at $t = 0.5$, respectively, of the incommensurate modulation of Sr atoms located at the border of the slab of the compound $SrNbO_{3.5}$ ($n = 4$) as reported by Daniels et al. (2002). Fig. 6.3*e* shows that Ca7 (one of the Ca atoms within the slab) has the distorted cubooctahedron coordination, as expected for a perovskite-type structure. For $SrNbO_{3.5}$ there seemed to be no obvious reason for an incommensurate structure to develop. Apparently, the different sizes and strengths of interactions of Sr versus Ca, and Nb versus (Nb,Ti) lead to an incommensurately modulated structure of $SrNbO_{3.5}$, while in $Ca(Nb_{0.76}Ti_{0.24})O_{3.33}$ the strain at the layers separating the slabs is resolved by a commensurate ($2a_0$) superstructure. As we have shown here, the mode of the displacement of the atoms is very similar in the two structures (Fig. 6.3).

The coordinations of (Nb,Ti) show different ranges of (Nb,Ti)–O bond lengths at different sites in the slabs. The spread in bond lengths around a single metal atom increases from the center to the borders of the slabs (Fig. 6.4). This variation in bond lengths represents a variation of distortion of $(Nb,Ti)O_6$ octahedra. A measure for the size of the octahedral distortion is the distortion index, $[\max(d[(\mathrm{Nb,Ti}) - \mathrm{O}]) -$

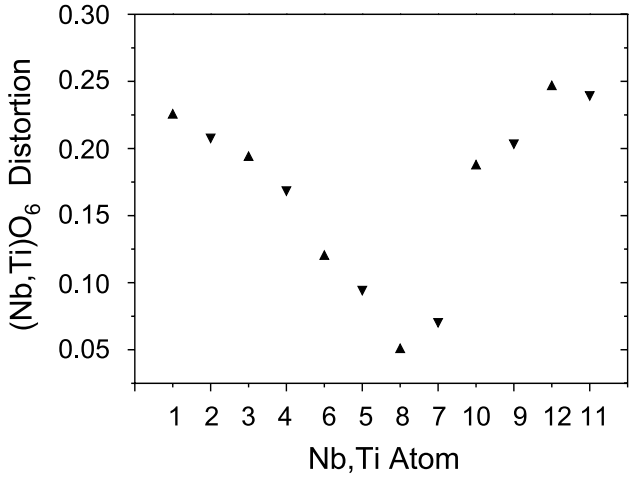

Figure 6.5: (Nb,Ti)O_6 octahedral distortion, here defined as [max(d[(Nb, Ti) − O]) − min(d[(Nb, Ti) − O])]/ave(d[(Nb,Ti) – O]). The Nb,Ti atoms are arranged according to their positions in the octahedral slab with the center of the graph corresponding to the center of the slab. The symbol ▲ corresponds to Nb,Ti atoms on one row along the c-axis while the symbol ▼ corresponds to those on the other row.

min(d[(Nb, Ti) − O])]/ave(d[(Nb,Ti) – O]) (Lichtenberg et al.; 2001), which is large at the borders and small near the middle of the slabs (Fig. 6.5). The large distortions for (Nb,Ti)O_6 octahedra at the borders of the slabs can be attributed to the elongation of some (Nb,Ti)-O distances, that reflects a stretching of the octahedra into the interlayer regions. Previous studies on related layered perovskites have also shown that the octahedra located at the slab borders are more deformed than those embedded within the slabs (Drews et al.; 1996; Daniels et al.; 2002, 2003; Zuniga and Darriet; 2003).

Refined atomic site occupancies indicate that there is preferential occupancy of Ti^{4+} at sites within the slabs over those sites at the borders of the slabs. The highest Ti occupancy was found in a region close to the centers of the slabs with 50% occupancy (0.508(7) − 0.530(7)), while lowest Ti occupancy of 0% was found at the borders of the slabs (Fig. 6.6). By comparing with Figure 6.4, the distribution of Ti appears to be inversely correlated with the mean (Nb,Ti)–O distance and the spread in (Nb,Ti)–O bond lengths. Thus Ti^{4+} prefer octahedral environments with the least distortion. This is consistent with the smaller ionic radius in a 6-fold coordination of Ti^{4+} (0.605 Å) compared to that of Nb^{5+} (0.64 Å) (Shannon; 1976). Kunz and Brown

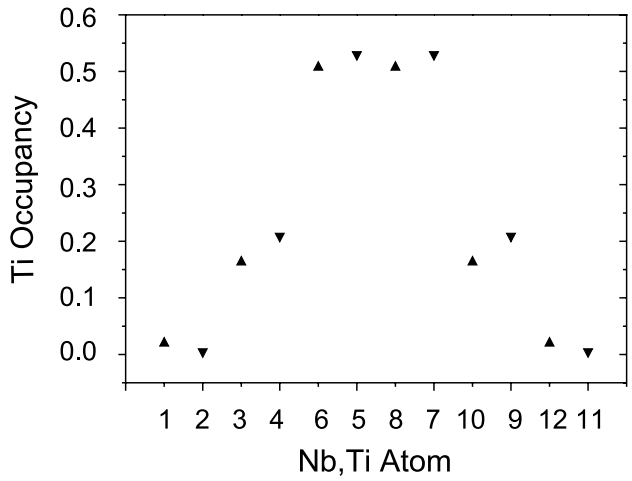

Figure 6.6: Ti atomic site occupancy. The Nb,Ti atoms are arranged according to their positions in the octahedral slab with the center of the graph corresponding to the center of the slab. The symbol ▲ corresponds to Nb,Ti atoms on one row along the *c*-axis while the symbol ▼ corresponds to those on the other row.

(1995) have shown that Nb^{5+} is associated with more highly distorted octahedral environment than Ti^{4+}. This preferential ordering of Ti^{4+} is consistent with the local charge distribution within the $Ca(Nb_{0.76}Ti_{0.24})O_{3.33}$ structure. Within the slabs, the presence of Ti^{4+} favors electroneutrality of the $CaTiO_3$ structural subunit. Substitution of Ti^{4+} by Nb^{5+} tends to build up positive charges in this region. The Nb^{5+} are therefore driven away from the interior of the slab and are more concentrated at the borders where there are unshared O^{2-} in other octahedra in the adjacent slab. A similar situation was observed in a study on the compound $Sr(Nb_{0.8}Ti_{0.2})O_{3.4}$ (Drews et al.; 1996).

Valences for Nb and Ti have been calculated by the bond-valence method using the parameters given by Brese and O'Keeffe (1991), assuming the (Nb,Ti) site to be fully occupied by either Nb or Ti (Fig. 6.7). Values of almost 5.0 and 4.0 were obtained for Nb and Ti, respectively, in accordance with the respective formal valences of 5+ and 4+. The good agreement with the formal valences suggests that Nb^{5+} and Ti^{4+} are equally well accommodated by all of the different oxygen environments as they are found in $Ca(Nb_{0.76}Ti_{0.24})O_{3.33}$. Thus the different occupancies (Fig. 6.6) can only be the result of more or less distorted environments or of band-structure

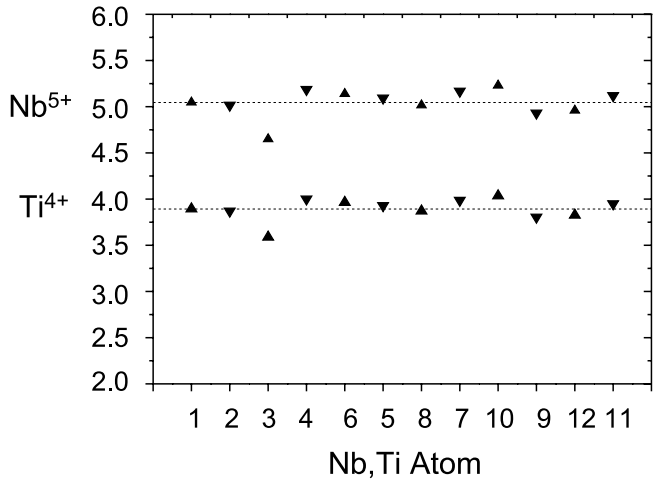

Figure 6.7: Nb and Ti valence for the different Nb,Ti atomic sites in the octahedral slab. The Nb,Ti atoms are arranged according to their positions in the slab with the center of the graph corresponding to the center of the slab. The symbol ▲ corresponds to Nb,Ti atoms on one row along the *c*-axis while the symbol ▼ corresponds to those on the other row. The dashed lines refer to the average valences.

effects.

The ideal chemical composition of insulating $Ca(Nb,Ti)O_{3.33}$ is $Ca(Nb_{0.67}Ti_{0.33})O_{3.33}$ (Lichtenberg et al.; 2001). Deviations from this stoichiometry towards the Nb-rich side result in extra electrons as compared to the formal valences Nb^{5+}/Ti^{4+}. The crystal investigated here is transparent and therefore insulating. Nevertheless, the refined composition of $Ca(Nb_{0.76}Ti_{0.24})O_{3.33}$ indicates an additional 0.1 electron / (Nb,Ti) site. Several explanations can be given for the insulating behavior, as we discuss below.

One explanation for the insulating behavior is that a wrong composition ($Nb_{1-z}Ti_z$) was obtained and that the actual composition is the ideal composition mentioned above, i.e. ($Nb_{0.67}Ti_{0.33}$). However, based on the refined occupancies, which gives proportion of Nb to Ti significantly different from the ideal proportion, the actual crystal investigated is likely to have a composition different from this ideal composition. Since the standard uncertainties for the refined occupancies are very small (± 0.007), we believe that the real composition of the crystal is close to the refined composition, which already contains less niobium atom than the nominal composition $Ca(Nb_{0.8}Ti_{0.2})O_{3.4}$.

Secondly, charge neutrality can be achieved by additional oxygen atoms. Given the Nb/Ti ratio, the composition corresponding to a fully oxidized state is $Ca(Nb_{0.76}Ti_{0.24})O_{3.38}$. This may be achieved by the presence of 0.05 interstitial oxygen atoms per formula unit. More likely, additional oxygen may be realized by vacancies at the metal sites. Normalizing to the ideal oxygen content (fully occupied oxygen sites), $x = 1/3$ for the $n = 6$ type of phase, the composition can be expressed as $Ca_{1-y}(Nb_{0.76}Ti_{0.24})_{1-y}O_{3.33}$ with $y \approx 0.015$. This means that there are about 1.5% vacancies at the metal sites. Structure refinements are not sufficiently accurate to discover such a small amount of vacancies.

A third explanation maintains partially filled d orbitals on Nb, but assumes that the extra electrons are in localized states. The computed valences for Nb and Ti, which are slightly smaller at the borders of the slabs (Fig. 6.7), suggest that these extra electrons are most likely found in the $4d$ orbitals of Nb at the borders of the slabs. Because of the large distortions of the octahedra, these electrons are localized, and the material is insulating. This is consistent with the refined occupancies for Nb and Ti. As Ti^{4+} preferentially enters into sites in the middle of the slabs, the effective charge at these sites is already substantially reduced with respect to 5+ and smaller than the charges at the sites near the border of the slabs. Extra electrons might thus more favorably be found at the border sites in $Ca(Nb_{0.76}Ti_{0.24})O_{3.33}$. At present based on our experimental results, we cannot decide definitely which among these above-mentioned possibilities is the appropriate explanation for the stoichiometry of the material.

6.4 Conclusions

The crystal structure at room temperature of $Ca(Nb_{0.76}Ti_{0.24})O_{3.33}$ has been successfully determined by single-crystal X-ray diffraction with synchrotron radiation. The structure is monoclinic $P2_1$ and consists of slabs of vertex-sharing (Nb,Ti)O_6 octahedra. The Ca atoms bordering the gap between slabs are coordinated by 7 oxygen atoms, while those within the slabs have the regular 12-fold coordination. Partial ordering of Nb^{5+} and Ti^{4+} has been observed over the twelve 6-fold coordinated (Nb,Ti) atomic sites, with the middle of the slab as the most preferred site for Ti^{4+}, while those at the borders of the slabs have zero Ti occupancy. This preferential occupancy of Ti^{4+} has been found to be correlated with the distortion of

the $(Nb,Ti)O_6$ octahedra with Ti^{4+} preferring the least distorted octahedral environment. The computed valences for Nb^{5+} and Ti^{4+} agree well with their formal valences and do not provide a driving force for Nb/Ti order. The non-stoichiometry in the refined composition and the insulating character of the material may be explained in terms of extra oxygen, vacancies on the cation sites, or by localization of the electrons in the $4d$ orbitals of Nb at the borders of the slabs.

Chapter 7

Crystal Structure of Perovskite-related $Ca_5Nb_4TiO_{17}$

Abstract

The crystal structure of perovskite-related $Ca_5Nb_4TiO_{17}$ has been determined by means of single-crystal X-ray diffraction. The compound is a $n = 5$ member of the homologous series $A_nB_nO_{3n+2}$. The crystal structure is monoclinic, $P2_1/c$, and comprises of slabs of corner-sharing (Nb,Ti)O_6 octahedra that are five layers wide. The slabs are separated by additional layers of oxygen atoms. The distortion of the octahedra is minimal in the middle of the slabs and increases towards the borders of the slabs. Ti ions preferentially occupy the sites in the middle of the slabs. Computed valences for Nb and Ti ions indicate that both Nb^{5+} and Ti^{4+} ions are equally well accommodated by the different oxygen environments at different (Nb,Ti) sites of the slabs.

7.1 Comment

Compounds of the homologous series $A_nB_nO_{3n+2}$ where A = Ca, Sr, or La and B = Ti or Nb with n = 4, 4.33, 4.5, 5, 6, and 7 are a special group of perovkite-related compounds with interesting electronic and dielectric properties (Lichtenberg et al.; 2001; Bobnar et al.; 2002; Kuntscher et al.; 2004). The crystal structures within this family of compounds can be derived from the ideal ABO_3 perovskite structure

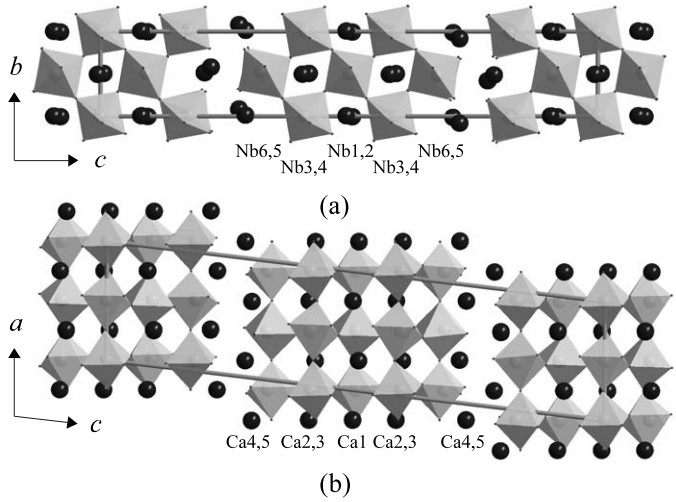

Figure 7.1: Projections of the crystal structure of $Ca_5Nb_4TiO_{17}$ along (a) the [100] and (b) the [010] directions. Large dark spheres represent Ca atoms while the (Nb,Ti)O_6 are outlined.

type. Slabs of n octahedra wide with the perovskite-type structure are separated by additional layers of O atoms. The slabs are stacked along the [110] direction of the ideal perovskite-type structure which corresponds to the c*-axis in the present study (Fig. 7.1). Neighboring slabs are shifted with respect to each other by half of the body diagonal of the octahedron. In structures in which slabs of different widths are mixed, n is non-integral and indicates the average number of octahedral layers per slab, e.g., $n = 4.5$ corresponds to the alternation of slabs of four and five layers wide. Note that the limiting case $n = \infty$ corresponds to the ideal perovskite structure.

Initial structural studies on the $Ca_n(Ti,Nb)_nO_{3n+2}$ series have reported either monoclinic or orthorhombic symmetries for these compounds (Nanot et al.; 1979, 1981, 1983). For the compound $Ca_5Nb_4TiO_{17}$ ($n = 5$), in particular, they suggested $P2_1$ and $P2_1/c$ as possible spacegroups. The atomic positions and displacement parameters, however, have not been reported. In another study, Drews et al. (1996) proposed an orthorhombic structure with $a \simeq a_p$ (a_p being the lattice constant of the ideal undistorted perovskite-type structure) for the compound $Sr_5Nb_4TiO_{17}$ ($n = 5$). In the present work we report an accurate crystal structure of $Ca_5Nb_4TiO_{17}$ ($n = 5$) which is a fully-oxidized insulator. The crystal structure is monoclinic with $a \simeq$

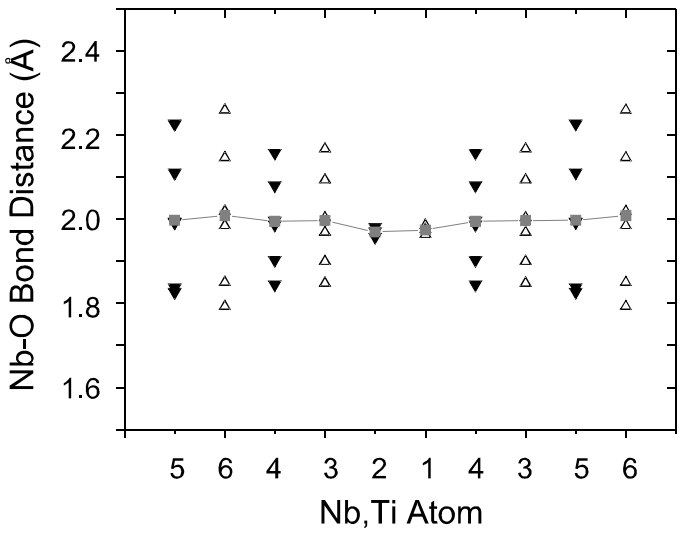

Figure 7.2: Distances between different (Nb,Ti) atoms and their coordinating O atoms. The (Nb,Ti) atoms are arranged such that the center of the horizontal axis of the graph corresponds to the center of the slab. The symbol △ corresponds to Nb atoms on one row along the **c**-axis while the symbol ▼ refers to a second row displaced by **a**/2. The symbol • denotes the mean (Nb,Ti)–O distance.

$2a_p$. Within the octahedral layers the corner-shared (Nb,Ti)O_6 octahedra extend zigzag-like along the **b** axis and chain-like along the **a** axis (Fig. 7.1).

Ca atoms possess different coordination environments. Atoms Ca1, Ca2, Ca3, which are embedded within the octahedral slabs, have a distorted cubooctahedron coordination, while the atoms Ca4 and Ca5, which are positioned near the borders of the slabs, have less than 12-fold coordination. Interatomic distances reveal that for Ca atoms within the slabs (Ca1, Ca2, Ca3), the Ca–O bond lengths range from 2.314(4) Å to 3.334(4) Å. Ca4 is 10-fold coordinated by O-atoms with bond lengths in the range 2.383(4) Å– 3.414(5) Å, while Ca5 are coordinated by 7 O-atoms with bond lengths in the range 2.309(4) Å– 2.538(4) Å.

The (Nb,Ti)O_6 octahedra have different degrees of distortion for different (Nb,Ti) sites in the slabs (Fig. 7.2). The six (Nb,Ti)–O bond distances around (Nb,Ti) exhibit the largest variation for sites near the borders and the smallest variation for sites in the middle of the slabs. Refined atomic occupancies reveal an ordering of Nb^{5+} and Ti^{4+} ions across the slabs. The highest Ti occupancy was found in the middle of the slabs (46.4%), while at the borders of the slabs, sites are almost

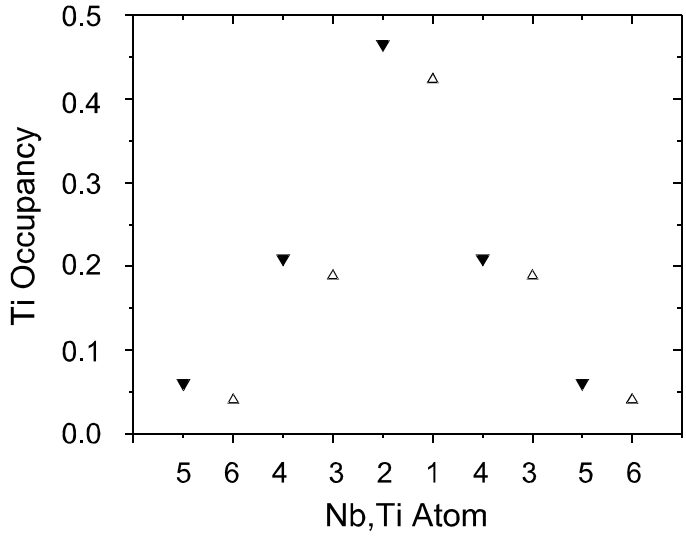

Figure 7.3: Ti site occupancies for the different (Nb,Ti) sites in the octahedral slab. The atom arrangement and symbols have the same meaning as in Fig. 7.2.

exclusively occupied by Nb (4% occupancy by Ti) (Fig. 7.3). Thus Ti^{4+} prefers oxygen environments with the least octahedral distortion. A similar trend of partial ordering has been observed for $Ca_6(Nb,Ti)_6O_{20}$ ($n = 6$) (Guevarra et al.; 2005a). In a systematic study of the out-of-center distortions around octahedrally coordinated d^0 transition metals, Kunz and Brown (1995) have shown that Nb^{5+} is associated with more highly distorted environment than Ti^{4+}. This preferential ordering is consistent with local charge neutrality within the $Ca_5Nb_4TiO_{17}$ substructure. Nb^{5+} tends to be more concentrated at the borders of the slabs where there are unshared bonds of O^{2-} while the presence of Ti^{4+} favors electroneutrality of the $CaTiO_3$ subunit within the slabs.

Bond-valence sums (Brese and O'Keeffe; 1991) have been computed for all crystallographically independent (Nb,Ti) sites, assuming the site to be fully occupied by either Nb^{5+} or Ti^{4+}, because the compound, being fully oxidized, has exclusively Nb^{5+} and Ti^{4+} (Fig. 7.4). The valences obtained for Nb^{5+} and Ti^{4+} ions for different (Nb,Ti) sites are close to their formal valences of 5+ and 4+, respectively. The good agreement indicates that Nb^{5+} and Ti^{4+} are equally well accommodated by all the different oxygen environments in the octahedral slabs, and that the observed partial ordering of Nb and Ti over the six crystallographically independent sites can only be the result of the different distortions of the octahedral environment.

Table 7.1: Experimental Details

Crystal Data	
$Ca_5Nb_4TiO_{17}$	Mo $K\alpha$ radiation
$M_r = 891.9$	λ=0.71069 Å
Monoclinic	Cell parameters from 25 reflections
$P2_1/c$	$\theta = 19.4 - 22.9°$
$a = 7.6889(3)$Å	$\mu = 5.867$ mm^{-1}
$b = 5.4763(1)$Å	$T = 293(2)$K
$c = 32.253(1)$Å	Irregular plate
$V = 226.4(2)$Å^3	Colorless
$Z = 4$	$0.15 \times 0.10 \times 0.025$ mm
$D_x = 4.3912$ Mg m^{-3}	
Data Collection	
MAR345 dtb diffractometer	3231 independent reflections
ψ-scans	2731 reflections with $I > 3\sigma(I)$
Absorption correction	$R_{int} = 0.0212$
numerical CrysAlis Red (Oxford Diffraction; 2004)	$\theta_{max} = 27.53°$
and X-Shape (STOE and Cie; 1999)	$h = -9 \rightarrow 9$
$T_{min} = 0.52411$, $T_{max} = 0.83390$	$k = -7 \rightarrow 7$
54795 measured reflections	$l = -41 \rightarrow 41$
Refinement	
Refinement on F	$(\Delta/\sigma)_{max} = 0.0005$
$R = 0.0504$	$\Delta\rho_{max} = 2.88$ eÅ^{-3}
$wR = 0.0596$	$\Delta\rho_{min} = -2.12$ eÅ^{-3}
$S = 2.60$	Extinction correction: none
3231 reflections	Scattering factors from International Tables
254 parameters	Vol C Tables 4.2.6.8 and 6.1.1.1
$w = 1/(\sigma^2(F) + 0.0001F^2)$	

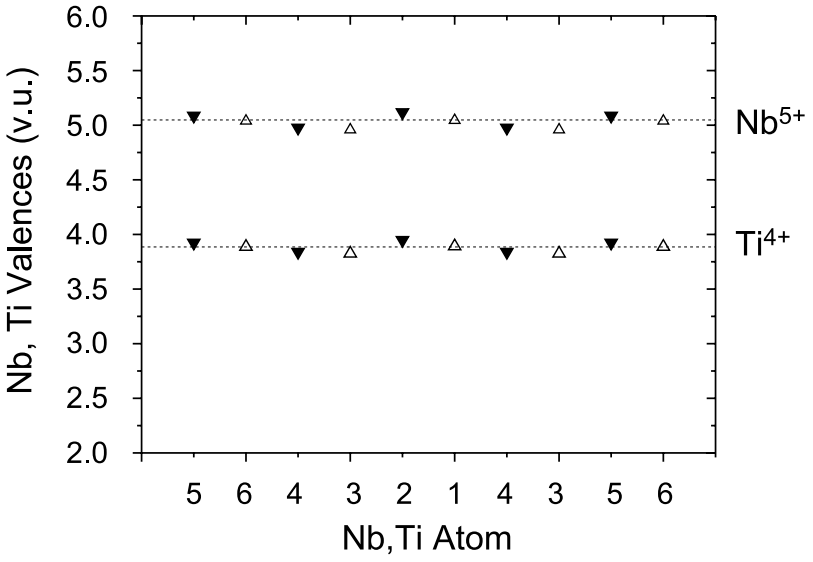

Figure 7.4: Nb and Ti valences for the different (Nb,Ti) sites in the octahedral slab. The atom arrangement and symbols have the same meaning as in Fig. 7.2. The horizontal dashed line corresponds to the average valences.

7.2 Experimental

Single crystals of $Ca_5Nb_4TiO_{17}$ were prepared by floating-zone melting in air using $CaCO_3$, Nb_2O_5, and TiO_2 as starting materials (Lichtenberg et al.; 2001). X-ray diffraction was measured on a single-axis MAR345 dtb diffractometer. In order to explore reflections lying along the rotation axis of the diffractometer, the crystal was oriented in three different ways. One data set was measured at the zero position of the arc of the goniometer head and two other data sets were measured at its two extreme positions of $\pm 12°$. The three data sets were processed separately using CrysAlis Red (Oxford Diffraction; 2004) and they were subsequently merged and scaled in JANA2000 (Petricek et al.; 2000).

Structural parameters of $Ca_5Nb_5O_{17}$ (Guevarra et al.; 2005b) were used as starting stuctural model. Since Nb and Ti atoms disorderly occupy the same sites, their positional and thermal parameters were constrained to be equal. Initial refinements, employing 54795 reflections merged towards a set of unique reflections, were not entirely satisfactory, resulting in non-positive temperature factors for several O atoms. Therefore we used intensity data as obtained by extracting the intensities

of the unique reflections for each of the three runs separately, employing CrysAlis Red. The three data sets were subsequently merged into a single data set of unique reflections employing JANA2000. Refinement resulted in a fit with $R_F = 0.0699$ and $S = 4.89$, but still with non-positive definite temperature parameters for some O atoms. An improved fit was obtained by the introduction of pseudo-merohedral twinning with a twin law corresponding to a 2-fold axis along the [100] direction, resulting in the superposition of reflections $(h\ k\ l)_I$ and $(h\ \text{-}k\ \text{-}(h+l))_{II}$ of the respective twin domains. The final refinement, with all atoms refined anisotropically, converged towards $R_F = 0.0504$ and S = 2.60, with a twin volume fraction of the second domain of 0.094(1). Temperature factors of all atoms were found to be positive definite. The atomic coordinates and displacement parameters can be found in Appendix F

Data collection: MAR345 dtb (Klein; 2004). Cell refinement: CAD-4 (Enraf-Nonius; 1989). Data reduction: CrysAlis Red (Oxford Diffraction; 2004). Program(s) used to refine structure: JANA2000 (Petricek et al.; 2000). Molecular graphics: Diamond (Brandenburg; 2005). Software used to prepare material for publication: JANA2000 (Petricek et al.; 2000).

Chapter 8

Superspace Description of the Crystal Structures of $Ca_n(Nb,Ti)_nO_{3n+2}$ ($n = 5$ and 6)

Abstract

Crystal structures of two members of the homologous series $Ca_n(Nb,Ti)_nO_{3n+2}$ with $n = 5$ and 6 are presented within the superspace formalism. The superspace description is based on the proposition that a common superspace model can be used to describe the crystal structures of all compositions within a particular homologous series, while the primary modulation wave vector and the width of the atomic domains vary with composition (Elcoro et al.; 2000). The crystal structures are characterized as commensurately modulated structures consisting of discontinuous atomic domains described by occupational crenel functions. The displacive modulation functions for the two compounds exhibit similarities, but they also show that the idea of a unified superspace model does not extend towards the precise atomic positions. For $n = 6$, the centrosymmetric superspace symmetry provides a natural explanation for the pseudo-symmetries that are present in the acentric supercell structure of this compound. The efficiency of the superspace approach is demonstrated by structure refinements in (3+1) dimensional space and by comparing these results with the 3-dimensional refinements in their supercells for the two compounds.

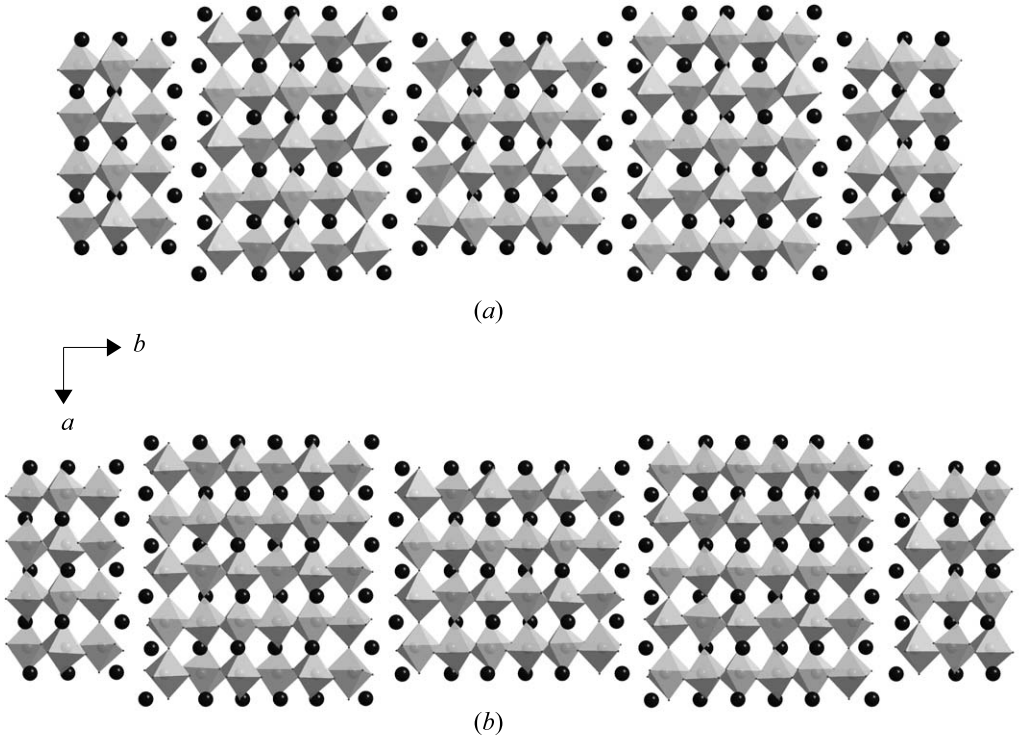

Figure 8.1: Projections of the structures along **c** of (*a*) $Ca_5Nb_4TiO_{17}$ ($n = 5$) and (*b*) $Ca_6(Nb,Ti)_6O_{20}$ ($n = 6$). Dark circles represent Ca atoms while $(Nb,Ti)O_6$ octahedra are outlined.

8.1 Introduction

The crystal structures of $Ca_5Nb_4TiO_{17}$ ($n = 5$) and $Ca_6(Nb,Ti)_6O_{20}$ ($n = 6$) at room temperature have recently been determined employing different unit cells and different space groups for the two compounds (Guevarra et al.; 2005a, 2006). These compounds belong to the homologous series $A_nB_nO_{3n+2}$ with A = Ca and B = Nb or Ti. The crystal structures of these compounds can be described as layered structures comprising of slabs of corner-sharing ABO_3 octahedra which are stacked along the [110] direction of the cubic perovskite structure (Fig. 8.1). The width of the slabs is determined by the composition and it is given directly by the parameter n. Neighboring slabs are separated by additional layers of oxygen atoms, and they are displaced with respect to each other by half the body diagonal of an octahedron along **a**.

Perez-Mato et al. (1999) have proposed that different compounds within a homologous series can be described by a unified structure model employing the superspace approach. The crystal structures of different compounds (different n) are obtained from systematic variation of the modulation wave vectors and of the widths of the block-wave functions that are used to describe the occupational modulations of the atoms. The basic structure and the symmetry — as specified by a superspace group — are common to all compounds of a homologous series. The efficiency of the superspace approach has been demonstrated for several compounds belonging to different homologous series (Zakhour-Nakhl et al.; 2000; Dariet et al.; 2002; Boullay et al.; 2002).

A superspace model for the homologous series $A_nB_nO_{3n+2}$ has been proposed by Elcoro et al. (2001). It was successfully applied to the structure refinement of the $n = 5$ member $NaCa_4Nb_5O_{17}$ of the series $(Na,Ca)_nNb_nO_{3n+2}$ (Elcoro et al.; 2004). In the present work we have applied the superspace model of Elcoro et al. (2004) to the $n = 5$ and $n = 6$ members of the homologous series $Ca_n(Nb,Ti)_nO_{3n+2}$. It is shown that the unified superspace approach applies to these two compounds indeed. Their structures are described by a unique superspace group and a common basic structure. The different stoichiometry is introduced via the modulation wave vectors and occupational modulation functions, which systematically depend on n. However, it is found that the unified description is not valid for the displacive modulations that define the precise atomic positions in the supercells. For the $n = 6$ compound, the superspace approach provides a natural explanation for the pseudo-symmetries as they were previously noticed in the supercell structure of $Ca_6(Nb,Ti)_6O_{20}$ (Guevarra et al.; 2005a).

8.2 Experimental

8.2.1 The Layer Model

As introduced by Elcoro et al. (2001), the crystal structures of the perovskite-related homologous series $A_nB_nO_{3n+2}$ can be described in terms of a stacking of two kinds of layers with composition ABO and layers of pure oxygen. The stacking sequence for $n = 5$, for instance, may be labelled as $OMONOMONOMO\oslash O'N'O'M'O'N'O'M'O'N'O'\oslash$..., where M and N denote the two kinds of ABO lay-

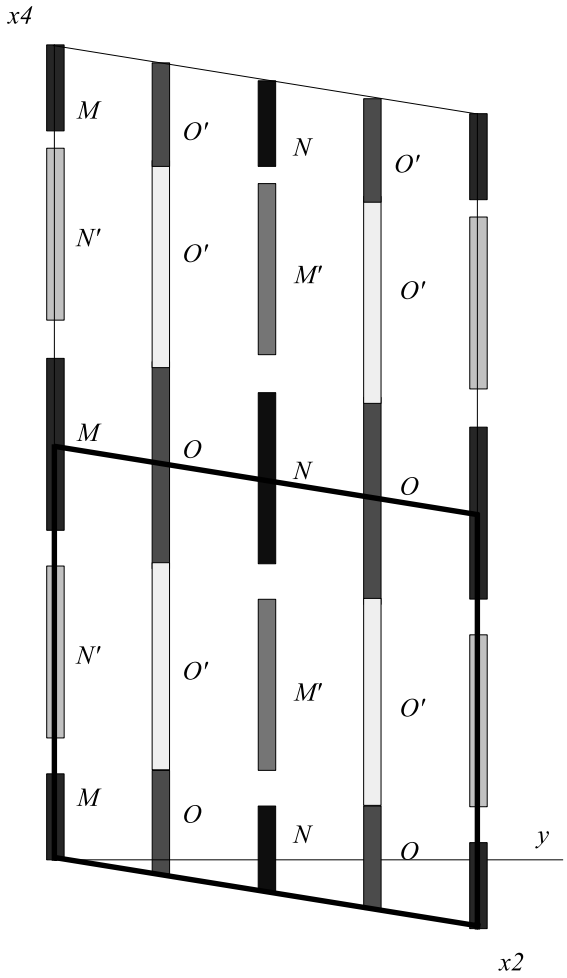

Figure 8.2: $x_2 - x_4$ section of the set of atomic domains in superspace for the $n = 5$ member of the homologous series $A_nB_nO_{3n+2}$ according to Elcoro et al. (2004). The atomic domains, represented by the rectangular strips parallel to x_4, denote occupancies 1 of the respective layer types M, M, N, N', O, and O'. Two unit cells along x_4 are shown. The superspace unit cell for the $n = 5$ member of the series $Ca_n(Nb,Ti)_nO_{3n+2}$ has been doubled with respect to the $Sr_n(Nb,Ti)_nO_{3n+2}$ series (Elcoro et al.; 2001). The modulation wave vector is $\mathbf{q} = (0\ \frac{1}{12}\ 0)$.

ers and O indicates layers of oxygen. Symbols M', N' and O' denote layers from neighboring slabs shifted by $\mathbf{a}_p/2$ with respect to the original layers ($\mathbf{a}_p$ being the edge of a cubic perovskite). The symbol $\oslash$ represents a missing ABO layer and it indicates a plane of separation between slabs (Fig. 8.1). For $n = 6$, the atomic layers follow the sequence $OMONOMONOMONO\oslash O'M'O'N'O'M'O'N'O'M'O'N'O'\oslash$... Ṅon-integral values of n are possible and correspond to the intergrowth of slabs with different number of layers. For $n = 4.5$, for instance, the stacking sequence is represented by $OMONOMONO\oslash O'M'O'N'O'M'O'N'O'M'O'\oslash ONOMONOMO \oslash O'N'O'M'O'N'O'M'O'N'O'$.

According to Elcoro et al. (2001), the layer stacking sequence can be described by a common superspace group valid for the whole homologous series $A_nB_n\mathrm{O}_{3n+2}$. The superspace unit cell contains a set of atomic domains, which is the same for the whole range of compositions. The only composition-dependent parameters are the the modulation wave vector and width of the atomic domains (Fig. 8.2). The atomic domains are described in terms of step-like atomic occupational modulations with respect to the underlying average period. The presence of either a vacant ABO layer or shifted layers along the stacking sequence is thus realized through the limitation of the corresponding atomic occupation functions along the internal subspace x_4 to discontinuous intervals as characteristic of the step-like functions (Petricek et al.; 2000).

The unique (3+1)-dimensional superspace group for the whole series can be labelled as $F'mmm(0, \sigma_2^{'}, 0)$, where $\sigma_2^{'} = 1/(n+1)$ and F' represents a set of non-standard centering translations (0000),$(\frac{1}{2}, \frac{1}{2}, 0\frac{1}{2})$, $(\frac{1}{2}, 0, \frac{1}{2}, \frac{1}{2})$, and $(0, \frac{1}{2}, \frac{1}{2}, 0)$ (Elcoro et al.; 2001). This superspace symmetry describes the parent, non-distorted structure in the average orthorhombic unit cell defined by $a \simeq a_p$ and $b \simeq c \simeq 2^{1/2}\mathrm{a}_p$, where a_p is the lattice constant of a cubic perovskite. The relevant subgroup must be selected in order to appropriately describe the structural relaxation, which exhibits double periodicity along the a axis for the case of the two compounds investigated. To do this, it is convenient to express the symmetry elements of the superspace group $F'mmm(0, \sigma_2^{'}, 0)$ in a supercell describing the superspace lattice of the distorted experimental structure. In this new setting, the a parameter of the average unit cell and the lattice parameter along the internal coordinate x_4 are doubled, and the modulation wave vector becomes $(0, \sigma_2^{'}/2, 0)$. The associated superspace group can be denoted as $Xmmm(0, \sigma_2, 0)$, where $\sigma_2 = \sigma_2^{'}/2$. The extra center-

ing contained in X compensates for the larger unit cell (Elcoro et al.; 2004). For $NaCa_4Nb_5O_{17}$ ($n = 5$) (Elcoro et al.; 2004), a systematic search of all possible subgroups of $Xmmm(0, \sigma_2, 0)$ yielded the superspace group that is appropriate to describe the observed supercell space group, $C112_1/d$. This superspace group, including its symmetry operations and centering translations, has been used in the present investigations (Table 8.2).

The crystal structures of the two compounds investigated here may be described as commensurate modulations of the underlying basic structure. Thus, the initial phase of the modulation, t_o, must be properly chosen to yield the appropriate three-dimensional structure since different values of t_o yield different structures in real space. For the two compounds investigated, $t_o = 0$ for $n = 5$ and $t_o = \frac{1}{56}$ for $n = 6$, yield the correct supercell groups as presented in Table 8.1.

8.2.2 Supercell Refinements

The crystal structures of $Ca_5Nb_4TiO_{17}$ ($n = 5$) and $Ca_6(Nb,Ti)_6O_{20}$ ($n = 6$) have been described with monoclinic unit cells with nearly equal a and b lattice parameters and long c axes of different length in a b-unique setting (Guevarra et al.; 2005a, 2006). In order to be consistent with the setting of Elcoro et al. (2004), the monoclinic unit cell of Guevarra et al. (2005a, 2006) has been transformed first to a setting with $\mathbf{c}$ as unique axis. Secondly, the primitive unit cells have been transformed to non-standard, C-centered unit cells according to $\mathbf{a}_o = \mathbf{a}_m$, $\mathbf{b}_o = \mathbf{a}_m + 2\mathbf{b}_m$, $\mathbf{c}_o = \mathbf{c}_m$ (Table 8.1). Finally, the origins of the unit cells have been shifted by $-\frac{1}{4}\mathrm{a_o} - \frac{1}{2}\mathrm{c_o}$, in order to conform to the superspace model of Elcoro et al. (2004). The C-centered settings are related to the layer model (Sec. 8.2.1) through the axes $\mathbf{b}_o$ being the stacking axes.

Structure refinements have been performed for both compounds in their C-centered settings, employing the computer program JANA2000 (Petricek et al.; 2000). Nb and Ti atoms disorderly occupy the same sites. Therefore, equal atomic coordinates and thermal parameters were assigned to Nb and Ti on each of the independent sites in agreement with the previous refinements (Guevarra et al.; 2005a, 2006). For the centrosymmetric $Ca_5Nb_4TiO_{17}$ ($n = 5$), the structural model contains six independent (Nb,Ti) atoms, five independent Ca atoms, and 17 independent O atoms, requiring a total of 84 positional parameters. The refinement, including anisotropic atomic displacement parameters (ADPs) for all atoms, the twin volume

fraction, and occupation fraction of Ti for each (Nb,Ti) site required a total of 252 parameters.

In the case of the acentric $Ca_6(Nb,Ti)_6O_{20}$ ($n = 6$), the structure model consists of 12 independent (Nb,Ti) atoms, 12 independent Ca atoms, and 40 independent O atoms resulting in a total of 192 positional parameters. Additional constraints were imposed on the ADPs and occupancies of (Nb,Ti) sites that are defined by a pseudo-inversion center. The refinement with isotropic ADPs for O atoms, the twin volume fraction, and occupation fractions required a total of 292 parameters. The structure refinements in the C-centered settings converged to identical R values and identical structures as what have been reported for refinements in the primitive settings (Table 8.1 and Guevarra *et al.*, 2005a; Guevarra *et al.*, 2006).

Table 8.1: Details of supercell refinements in the primitive and C-centered settings. Diffraction data from (Guevarra et al.; 2005a, 2006)

Compound	$Ca_5Nb_4TiO_{17}$		$Ca_6(Nb,Ti)_6O_{20}$	
	Primitive	C-centered	Primitive	C-centered
Spacegroup	$P112_1/b$	$C112_1/d$	$P112_1$	$C112_1$
a(Å)	7.6889(3)	7.6889(3)	7.681(2)	7.681(2)
b(Å)	32.253(1)	64.057(2)	37.747(6)	75.09(1)
c(Å)	5.4763(1)	5.4763(1)	5.465(1)	5.465(1)
$\gamma(^\circ)$	96.767(7)	89.921(7)	95.87(1)	90.04(1)
V(Å^3)	1348.6(1)	2697.2(2)	1576.1(1)	3152.3(2)
Z	4	8	4	8
No. of reflections	54795	54795	24459	24459
No. of unique reflections (obs[$I > 3\sigma$]/all)	2731/ 3231	2731/ 3231	5577/7800	5577/7800
	$h = -9 \rightarrow 9$	$h = -9 \rightarrow 9$	$h = -10 \rightarrow 10$	$h = -10 \rightarrow 10$
hkl range	$k = -41 \rightarrow 41$	$k = -82 \rightarrow 82$	$k = -50 \rightarrow 50$	$k = -100 \rightarrow 100$
	$l = -7 \rightarrow 7$	$l = -7 \rightarrow 7$	$l = -7 \rightarrow 7$	$l = -7 \rightarrow 7$
R_{int} (obs/all)	0.0204/0.0212	0.0204/0.0212	0.0307/0.0326	0.0307/0.0326
R (obs/all)	0.0504/ 0.0575	0.0504/ 0.0575	0.0545/ 0.0755	0.0545/ 0.0755
Rw (obs/all)	0.0582/ 0.0596	0.0582/ 0.0596	0.0605/0.0638	0.0605/0.0638
S (obs/all)	2.78/2.60	2.78/2.60	2.45/2.17	2.45/2.17
No. of parameters	254	254	292	292

8.2.3 Superspace Refinements

Structure refinements in (3+1)-dimensional superspace were carried out with JANA2000 (Petricek et al.; 2000). Reflection indices (hkl) with respect to the supercells were transformed towards four-integer indexings ($HKLM$) with respect to the basic-structure unit cells and modulation wave vectors. Main reflections correspond to the reflections (hkl) with $k = 12K$ for $n = 5$ and $k = 14K$ for $n = 6$. Satellite reflections are those reflections with $k = 12K + M$ ($M = \pm1, \pm2, \pm3, \pm4, \pm5, \pm6$) and $k = 14K + M$ ($M = \pm1, \pm2, \pm3, \pm4, \pm5, \pm6, \pm7$) for $n = 5$ and $n = 6$, respectively. The distribution of reflections among the different categories is given in Table 8.2.

The superspace model for $NaCa_4Nb_5O_{17}$ ($n = 5$) of Elcoro et al. (2004) was employed as starting model for the present refinements. Crenel functions for the occupational modulations in $Ca_5Nb_4TiO_{17}$ were identical to those in Elcoro et al. (2004) while the crenel functions for $Ca_6(Nb,Ti)_6O_{20}$ were adapted to the different composition and supercell period of this compound (Table 8.3). Displacement modulations and modulations of ADPs were described by orthogonalized functions according to the procedure by Petricek et al. (1995). Displacement parameters were determined by refinements starting with arbitrary but small values for those parameters.

Initial refinements including variations of the fraction Ti on the two crystallographically independent (Nb,Ti) sites were not entirely satisfactory, resulting in $R_F(obs) = 0.0584$ for $n = 5$ and $R_F(obs) = 0.0708$ for $n = 6$. The reason is that the two refined occupancy parameters are insufficient to describe the variations of Nb/Ti ratios as observed in the supercell refinements. Modulation functions for the Ti occupancy would be necessary, but they cannot be combined with crenel functions in the JANA2000 software. Instead, the domains of occupancy of each of the two (Nb,Ti) sites were split into five subdomains according to Fig. 8.3. Each site Nbi ($i = 1, 2$) is split into three crystallographically independent sites Nbi1, Nbi2 and Nbi3. The Nb/Ti ratio was then independently refined for each of the six independent sites. The model occupancies correspond exactly to the variations of occupancies as what have been observed in the supercell approach.

Orthogonalized functions for the displacement modulations were determined for the full domains of Nb1 and Nb2. They appeared to be well approximated by the first and sixth harmonics of the sine functions for $n = 5$, and an additional twelfth harmonic sine function for the $n = 6$ compound. This particular selection of sine

Table 8.2: Details of the superspace refinements

Compound	$Ca_5Nb_4TiO_{17}$	$Ca_6(Nb,Ti)_6O_{20}$
Superspace group	$C^{'}2_1/d\ (\sigma_1\ \sigma_2\ 0)\ \bar{1}\ 0$	$C^{'}2_1/d\ (\sigma_1\ \sigma_2\ 0)\ \bar{1}\ 0$
Superspace centering	$(0\ 0\ 0\ 0)$	$(0\ 0\ 0\ 0)$
	$(\frac{1}{2}\ 0\ 0\ \frac{1}{2})$	$(\frac{1}{2}\ 0\ 0\ \frac{1}{2})$
	$(\frac{3}{4}\ \frac{1}{2}\ 0\ \frac{1}{4})$	$(\frac{3}{4}\ \frac{1}{2}\ 0\ \frac{1}{4})$
	$(\frac{1}{4}\ \frac{1}{2}\ 0\ \frac{3}{4})$	$(\frac{1}{4}\ \frac{1}{2}\ 0\ \frac{3}{4})$
Superspace Symmetry	$(x_1\ \ x_2\ \ x_3\ \ x_4)$	$(x_1\ \ x_2\ \ x_3\ \ x_4)$
Operators	$(-x_1\ \ -x_2\ \ -x_3\ \ \frac{1}{2}-x_4)$	$(-x_1\ \ -x_2\ \ -x_3\ \ \frac{1}{2}-x_4)$
	$(\frac{1}{4}-x_1\ \ -x_2\ \ \frac{1}{2}+x_3\ \ \frac{1}{4}-x_4)$	$(\frac{1}{4}-x_1\ \ -x_2\ \ \frac{1}{2}+x_3\ \ \frac{1}{4}-x_4)$
	$(x_1\ \ \frac{1}{2}+x_2\ \ \frac{1}{2}-x_3\ \ x_4)$	$(x_1\ \ \frac{1}{2}+x_2\ \ \frac{1}{2}-x_3\ \ x_4)$
Basic Structure Unit Cell		
a(Å)	7.6889(3)	7.681(2)
b(Å)	5.338(1)	5.364(6)
c(Å)	5.4763(1)	5.465(1)
$\gamma(^\circ)$	89.921(7)	90.04(1)
V(Å^3)	224.8(1)	225.2(1)
q	(0 1/12 0)	(0 1/14 0)
No. of unique reflections (obs[$I > 3\sigma$]/all)	2731/ 3231	5186/5863
	$H = -9 \rightarrow 9$	$H = -8 \rightarrow 10$
$HKLM$ range	$K = -7 \rightarrow 7$	$K = -6 \rightarrow 7$
	$L = -7 \rightarrow 7$	$L = -7 \rightarrow 7$
	$M = -6 \rightarrow 6$	$M = -7 \rightarrow 7$
R_{int} (obs/all)	0.0205/0.0213	0.0300/0.0305
R(obs/all)	0.0512/0.0583	0.0581/0.0647
R_{w}(obs/all)	0.0600/ 0.0614	0.0652/0.0666
No. of Reflections (obs/all)		
Main reflections ($M = 0$)	212/246	262/271
Satellites $M = 1$	465/565	1012/1124
Satellites $M = 2$	463/499	539/542
Satellites $M = 3$	448/578	909/1130
Satellites $M = 4$	479/509	554/556
Satellites $M = 5$	431/578	896/1138
Satellites $M = 6$	233/256	533/538
Satellites $M = 7$	–	481/564
No. of parameters	146	162

Table 8.3: Definition of occupational modulation functions (crenel functions) of $Ca_5Nb_4TiO_{17}$ ($n = 5$) and $Ca_6(Nb,Ti)_6O_{20}$ ($n = 6$)

Atomic coordinates highlighted in bold are refinable. x_4 denotes the center of the atomic domain while Δ refers to its width. Nb domains, which have site symmetry $\bar{1}$, are described by antisymmetric displacive modulation functions. All other domains have no restriction in the type of symmetry-allowed displacive modulation functions.

	$Ca_n(Nb,Ti)_nO_{3n+2}$			$Ca_5Nb_4TiO_{17}$		$Ca_6(Nb,Ti)_6O_{20}$	
	$x1$	$x2$	$x3$	$x4$	Δ	$x4$	Δ
Nb1	1/4	0	1/2	0	5/24	0	3/14
Nb2	3/4	0	1/2	0	5/24	0	3/14
Ca1	**0**	**0**	**0**	0	1/8	0	1/7
Ca2	**0**	**1/4**	**0**	5/48	1/24	3/28	1/28
Ca3	**0**	**-1/4**	**0**	-5/48	1/24	-3/28	1/28
O1	**0**	**0**	**1/2**	0	5/24	0	3/14
O2	**1/4**	**1/4**	**1/4**	0	1/4	0	1/4
O3	**3/4**	**1/4**	**1/4**	0	1/4	0	1/4

functions was used for the displacement modulations of the (Nb,Ti) sites with split domains, because orthogonalized functions could not be generated in this approach. All six atoms Nb11, Nb12, Nb13, Ti11, Ti12 and Ti13 were constrained to have identical parameters for the basic position, ADPs, and displacement modulations, with a similar set of constraints for Nb21, Nb22, Nb23, Ti21, Ti22 and Ti23. Final refinements converged to R values almost equal to the R values of the supercell refinements, while employing about half as many parameters (Table 8.4). The atomic coordinates and ADPs and their corresponding modulation functions are provided in Appendix G.

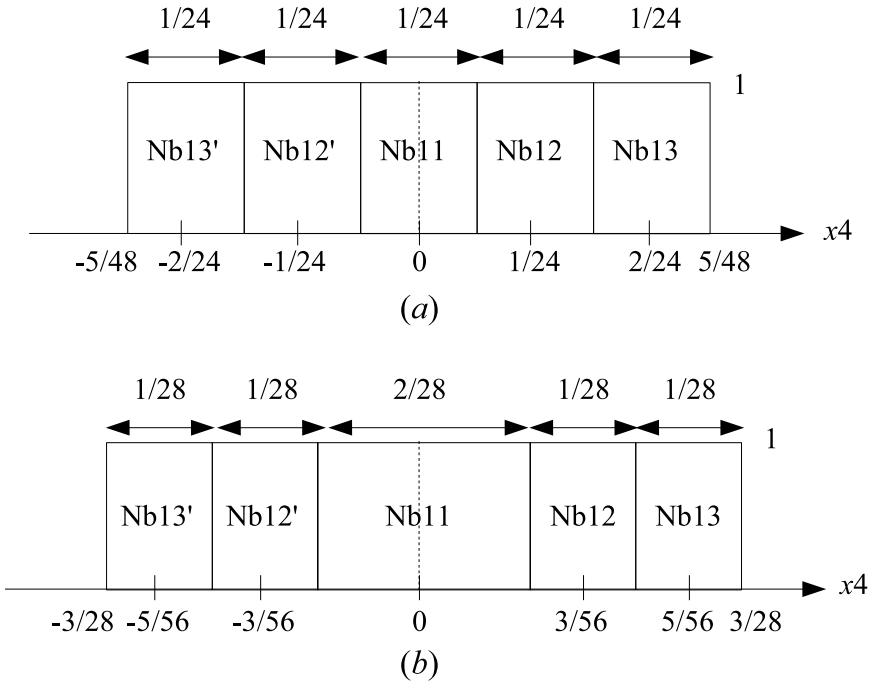

Figure 8.3: Subdomains comprising the atomic domains of Nb1 in (*a*) $Ca_5Nb_4TiO_{17}$ ($n = 5$) and (*b*) $Ca_6(Nb,Ti)_6O_{20}$ ($n = 6$). The widths and centers of the subdomains along x_4 are indicated. The occupancy probability of a sub-domain is equal to 1 within the indicated interval and zero outside this interval (and similarly for corresponding sets of sub-domains centered at $x_4 = integer$). An equivalent definition of subdomains Nb21, Nb22, and Nb23 applies to the site Nb2.

8.3 Discussion

8.3.1 Validation of the Superspace Refinements

Structure refinements applying the superspace approach have arrived at fits to the data of nearly equal quality as the supercell refinements, while employing much less parameters (Tables 8.1 and 8.2). For $Ca_5Nb_4TiO_{17}$ equal numbers of parameters have been used for the atomic positions in both supercell and superspace refinements. The slightly higher R value of the superspace refinements thus is due to a large reduction in the number of ADPs. However, introduction of additional modulated ADPs in the superspace model does not lead to significant non-zero values for them. The slightly better fit of the supercell model thus will mainly represent a fit to the

Table 8.4: Summary of the partial R values of the supercell and the superspace refinements

R factors in the fourth line refer to the complete set of reflections. The following lines correspond to the partial R factors for the main ($M = 0$) and satellite reflections of order M in the superspace refinements.

	3D	(3+1)D	3D	(3+1)D
Compound	$Ca_5Nb_4TiO_{17}$		$Ca_6(Nb,Ti)_6O_{20}$	
No. of Parameters	254	146	292	162
R(obs)/Rw(obs)	0.0504/0.0582	0.0512/0.0600	0.0545/0.0605	0.0581/0.0652
$M = 0$		0.0473/0.0589		0.0442/0.0578
$M = 1$		0.0442/0.0536		0.0713/0.0688
$M = 2$		0.0474/0.0597		0.0451/0.0551
$M = 3$		0.0464/0.0540		0.0854/0.0776
$M = 4$		0.0556/0.0655		0.0408/0.0493
$M = 5$		0.0573/0.0595		0.1097/0.0974
$M = 6$		0.0606/0.0641		0.0443/0.0566
$M = 7$		–		0.0943/0.0958

noise rather than a true structural effect.

Similar observations have been made for the refinements of $Ca_6(Nb,Ti)_6O_{20}$. Here, the atomic positions have been described by a smaller number of parameters in the superspace model than have been used in the supercell refinement. This reduction of parameters has led to less correlations between them and it has led to improved interatomic distances (see the discussion below).

The structure model of $Ca_5Nb_4TiO_{17}$ contains one additional modulation function each for the displacement modulations of O2 and O3, as compared to the structure model of $NaCa_4Nb_5O_{17}$ ($n = 5$) (Elcoro et al.; 2004). These additional functions were necessary to obtain a good fit to the data, and their values are comparable to the values of other modulation functions.

As proposed by Perez-Mato et al. (1999) and Elcoro et al. (2001), the same superspace model should apply to all members of the series $Ca_n(Nb,Ti)_nO_{3n+2}$. For $Ca_6(Nb,Ti)_6O_{20}$, we have noticed that 1937 reflections of the type ($HKLM$) :

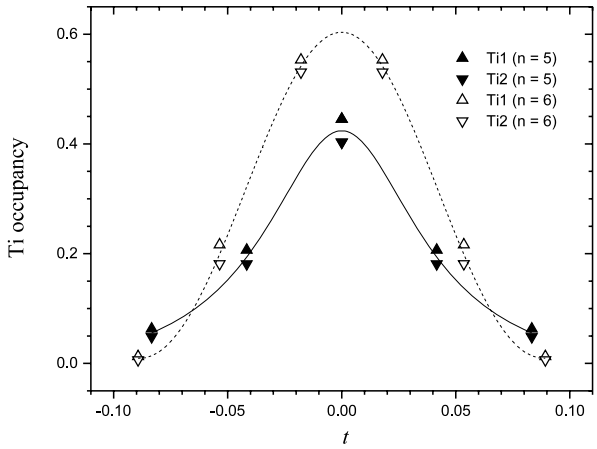

Figure 8.4: Site occupancy factors of Ti at the different Ti subdomains in $Ca_5Nb_4TiO_{17}$ ($n = 5$) and $Ca_6(Nb,Ti)_6O_{20}$ ($n = 6$). Curves are obtained by fits of Pseudo-Voigt functions centered at $t = 0$ to the data points.

$H + 2K - M \neq 4i$ (i = integer) are classified as extinct. Intensities of these reflections range up to 11σ, with 394 observed reflections and 105 reflections with $I > 5\sigma$. Obviously this class of reflections is weak, but some significant intensity has been observed. This intensity could possibly be explained if the centering translations $(\frac{1}{4}\ \frac{1}{2}\ 0\ \frac{3}{4})$ and $(\frac{3}{4}\ \frac{1}{2}\ 0\ \frac{1}{4})$ are dropped. However, refinements without this lattice centering are instable and suffer from high correlations between parameters. Alternatively, intensity at these points may be explained by stacking faults. Therefore, we conclude that the unified superspace structure model is applicable to the $n = 6$ compound in a very good approximation.

8.3.2 Modulation Functions

The supercell structures follow from the superspace structure model by the values of the modulation functions at n equidistant values of their arguments $\bar{x}_4$. For the Nb/Ti occupational modulation, a one-to-one match is thus obtained between supercell and superspace refinements (Fig. 8.4). Minor differences in occupancies between the two approaches can be explained by correlations that always exist between occupational parameters and ADPs.

It has been proposed that the superspace approach should provide a unified

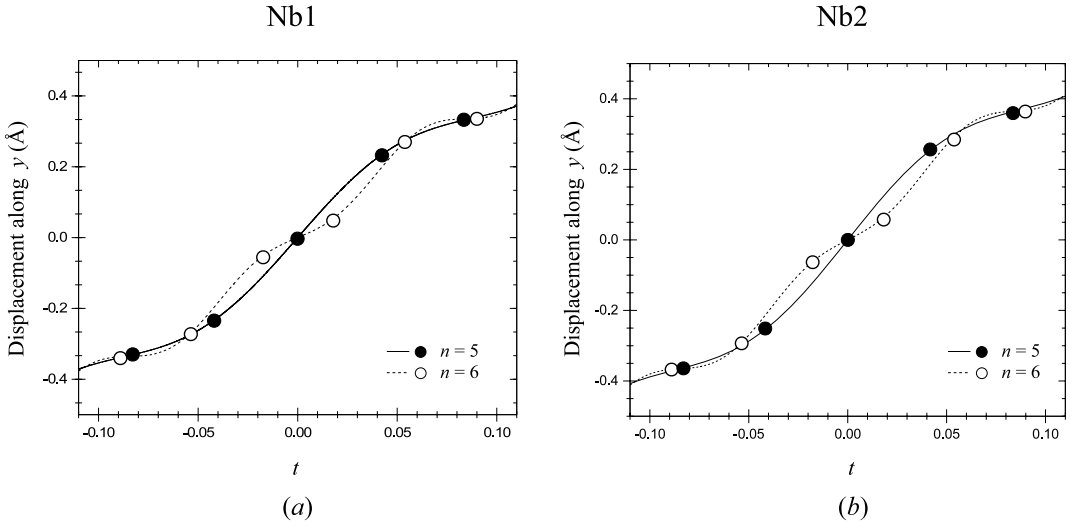

Figure 8.5: t-Plots of the y components of the displacement modulation functions of (a) Nb1 and (b) Nb2 atoms in $Ca_5Nb_4TiO_{17}$ ($n = 5$) and $Ca_6(Nb,Ti)_6O_{20}$ ($n = 6$). Filled circles and solid lines apply to $Ca_5Nb_4TiO_{17}$ ($n = 5$). Open circles and dotted lines apply to $Ca_6(Nb,Ti)_6O_{20}$ ($n = 6$). Circles correspond to atomic displacements in 3D space obtained by commensurate cuts of superspace.

model for all compounds of the homologous series $Ca_n(Nb,Ti)_nO_{3n+2}$. With accurate structure models for the two compounds this proposal can now be tested. First, it is noticed that a unified superspace model according to Table 8.3 applies in good approximation indeed. However, displacement modulation functions are not identical between the two refinements (Figs. 8.5 and 8.6). In particular, the refined functions for displacement modulations of atoms incorporate more parameters in the case of $n = 6$ than they possess for $n = 5$. Nevertheless, the refined functions of $n = 6$ do not describe exactly the positions of the atoms of $n = 5$. Although a rough match between the two modulations might be inferred from Figs. 8.5 and 8.6. It is thus concluded that the superspace models of the $n = 5$ and $n = 6$ compounds are slightly different as to accommodate the different supercell models of these two compounds.

For $Ca_6(Nb,Ti)_6O_{20}$ ($n = 6$) the superspace approach employs much less parameters than the supercell refinement, unlike in $n = 5$, for which the same number of occupational and positional parameters have been used. This difference reflects the different symmetries $P2_1$ and $P2_1/b$ of the supercell structures of both compounds.

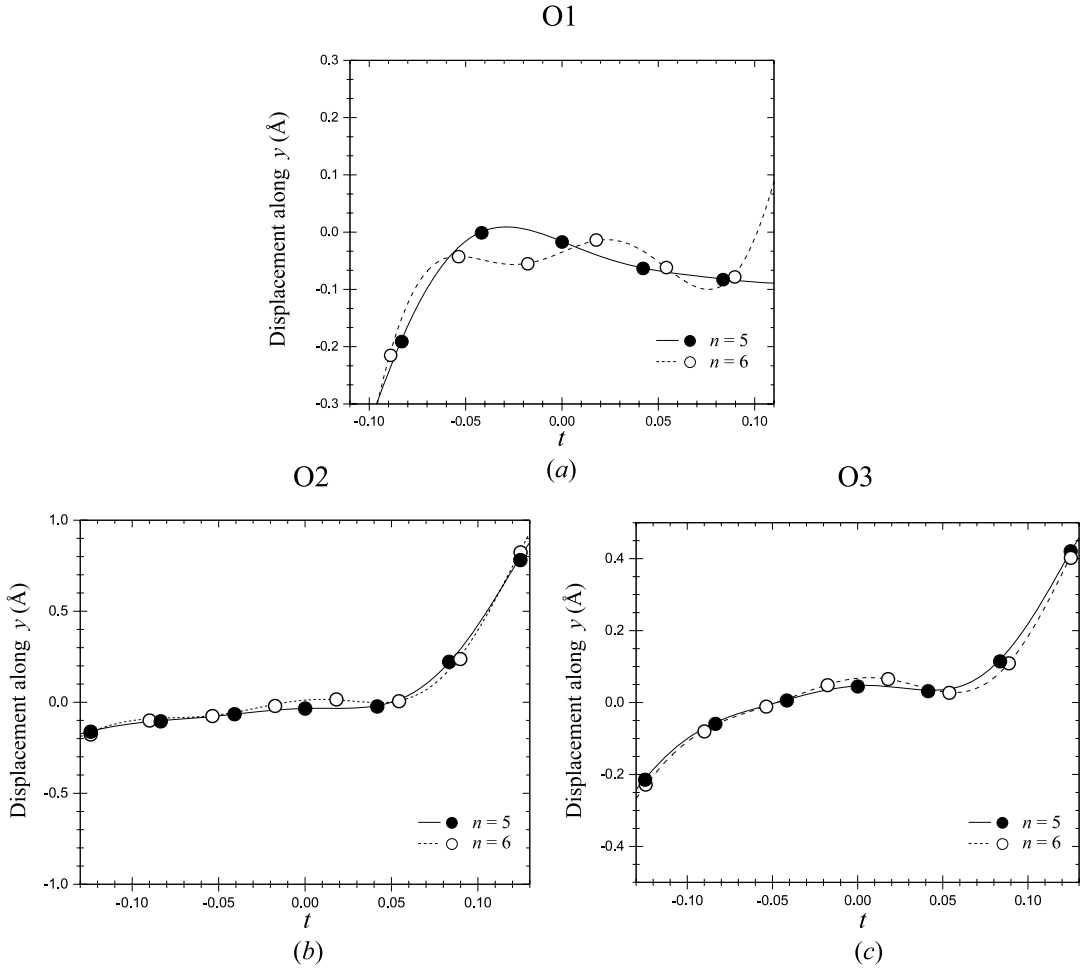

Figure 8.6: t-Plots of the y components of the displacive modulation functions of (a) O1, (b) O2 and (c) O3. Filled circles and solid lines apply to $Ca_5Nb_4TiO_{17}$ ($n = 5$). Open circles and dotted lines apply to $Ca_6(Nb,Ti)_6O_{20}$ ($n = 6$). Circles correspond to atomic displacements in 3D space obtained by commensurate cuts of superspace.

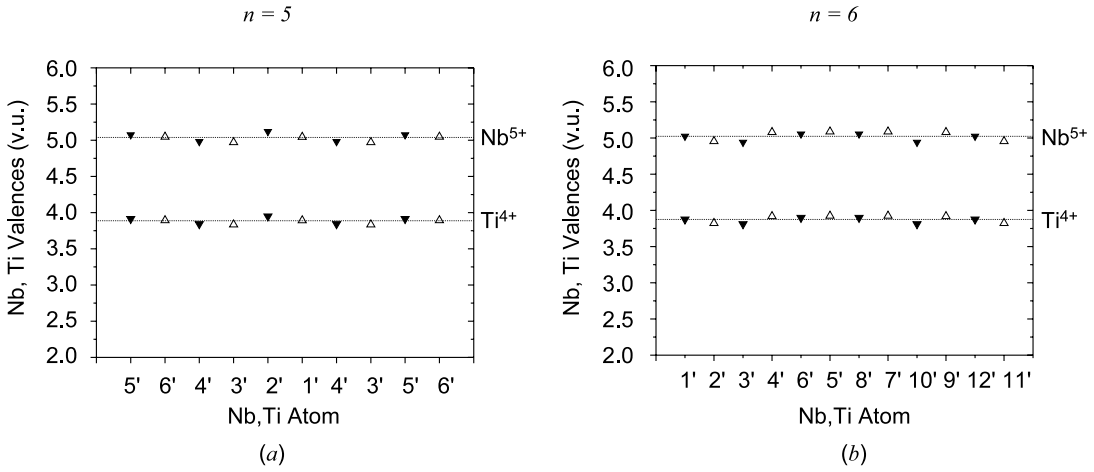

Figure 8.7: Nb and Ti valences for the different (Nb,Ti) sites in $Ca_5Nb_4TiO_{17}$ ($n = 5$) and $Ca_6(Nb,Ti)_6O_{20}$ ($n = 6$). The horizontal axis refers to the (Nb,Ti) sites in the 3D supercell as it has been obtained from the superspace structure model. The (Nb,Ti) atoms are arranged such that the center of horizontal axis corresponds to the center of the slabs in agreement with Guevarra *et al.*, 2005a and Guevarra *et al.*, 2006.

The superspace approach for $n = 6$ employs a centrosymmetric superspace group, and thus leads to equal Nb/Ti ratios on sites that are related by superspace inversion, but that are independent sites in the acentric supercell (Fig. 8.7). In this way, the superspace approach gives a natural explanation for the pseudo-symmetries as they have been observed in the supercell structure (Guevarra et al.; 2005a), while removing interdependencies between parameters.

The higher quality of the structure model obtained from the superspace refinement is illustrated by the computed valences (Fig. 8.4). Especially in the case of $n = 6$, computed valences are much closer to their formal values of 5+ for Nb and 4+ for Ti for all sites in the structure (compare Fig. 8.4 with Figs. 6.7 and 7.4)

8.4 Conclusions

The crystal structures of $Ca_5Nb_4TiO_{17}$ ($n = 5$) and $Ca_6(Nb,Ti)_6O_{20}$ ($n = 6$) have been described within the superspace approach. The structures can be interpreted as commensurately modulated structures with discontinuous atomic domains given by occupational crenel functions. The modulation wave vector and the width of

the atomic domains systematically depend on n. Refinements in superspace demonstrate the efficiency of the superspace approach. The economy of parameters used in the refinements and application of a unified superspace model to both $n = 5$ and 6 compounds show that the superspace approach is indeed effective in the structural description of these perovskite-related compounds. While a unified superspace model is valid for $n = 5$ and 6, the displacement modulations of (Nb,Ti) and O atoms are described by different functions in the two compounds, thus a unified superspace model does not extend towards the fine details of the structure models.

For $Ca_6(Nb,Ti)_6O_{20}$ ($n = 6$) the superspace model offers a natural explanation for the pseudo-inversion symmetry, as it has been previously noticed in the supercell structure (Guevarra et al.; 2005a).

Chapter 9

Conclusions

In this thesis, the crystal structures at room temperature of perovskite-related materials belonging to the homologous series $A_nB_nO_{3n+2}$ where A = Ca and B = Nb or Ti with $n = 5$ and 6 have been determined. The general features of the crystal structures of these compounds are the same for all n. The crystal structures can be described as slabs of corner-shared BO_6 octahedra stacked along the [110] direction of the cubic perovskite-type structure. The slabs are separated by additional layers of oxygen atoms. Neighboring slabs are shifted with respect to each other by half the body diagonal of an octahedron along the **a** direction. The number of layers of octahedra in a slab determines the structure type which is composition-dependent, and is given by the parameter n.

Three compounds have been investigated in this thesis: $Ca_5Nb_5O_{17}$ ($n = 5$), $Ca_5Nb_4TiO_{17}$ ($n = 5$) and $Ca_6(Nb,Ti)_6O_{20}$ ($n = 6$). The crystal structures of these compounds have been accurately determined using single-crystal X-ray diffraction. Owing to the characteristic long unit cell parameters along the stacking direction of layers of octahedra, area detectors (Image Plate and CCD) have been utilized to obtain within reasonable time sufficient data for accurate structure determination. With the use of synchrotron radiation (or Mo-Kα radiation from a rotating-anode generator), the weak superlattice reflections have been accurately detected.

Previous structural studies of these compounds have mainly reported the building principles without atomic positions or the tilting of the octahedra (Nanot et al.; 1979, 1983). Accurate crystal structure provides precise atomic coordinates and atomic displacements which are necessary in predicting the physical and chemical properties of these compounds. These are what this thesis has contributed. In

this thesis, bond distances and bond angles computed for the (Nb,Ti)O_6 octahedra have provided meaningful insights about the tilting and distortion of the octahedra found at the different sites in the slabs. Computed bond valence sums (Brese and O'Keeffe; 1991) for the different (Nb,Ti) as they are found in the slabs have given useful information about the crystal chemistry and electrical properties of these compounds.

The crystal structure of $Ca_5Nb_5O_{17}$ ($n = 5$), which is a diamagnetic, electrically conducting compound, has been successfully determined using synchrotron radiation with a CCD detector. The crystal structure has a monoclinic lattice with $P2_1/c$ symmetry. The displacement of consecutive slabs with respect to each other results in a highly distorted coordination of the Ca atoms located near the borders of the slabs. The Ca atoms near the borders of the slabs have irregular coordination geometry with 7 coordinating O atoms, while the coordination of Ca atoms within the slabs can be described by a distorted cuboctahedron (12-fold coordination). The distorted coordination of the Ca atoms results in a local strain in the slabs which is relieved by a commensurate modulation of the structure leading to a twofold superstructure along [100]. The doubling of the periodicity along the **a** direction can be interpreted as due to the tilt system of consecutive octahedra along the a axis, which have antiphase tilting about the c axis. The NbO_6 octahedra also show distorted environments. The degree of distortion of the octahedra varies with position in the slabs. As evidenced by the bond distances and bond angles, the NbO_6 octahedra located at the center of the slabs are less distorted than those at the borders of the slabs. Bond valence sums have been calculated for Nb located at the different sites in the slabs. The valence of Nb found at the borders of the slabs is close to its formal valence of 5.0 v.u., and is found to decrease towards the center of the slabs. The smaller fractional valence at the center of the slabs indicates that the extra electrons in the 4d orbitals of Nb are most probably accommodated at Nb sites in the middle of the slabs. This implies that the electrical conduction in this compound most likely takes place in the middle of the slab where the NbO_6 octahedra are least distorted. For a related compound ($Sr_5Nb_5O_{17}$, $n = 5$), angle-resolved photoemission studies (ARPES) and band-structure calculations have indicated that the predominant contribution to the occupied electron density of states at the Fermi energy in this compound comes from the least distorted octahedra (Kuntscher et al.; 2000, 2002, 2004).

Several single-crystals have been prepared from crystals with nominal composition $Ca_5Nb_4TiO_{17}$ ($n = 5$). The material, which is an insulator, was found to be multi-phase consisting also of the $n = 6$ type. A good single crystal of this $n = 6$ type was found, and its crystal structure at room temperature was determined using synchrotron radiation with a CCD detector. The crystal structure is monoclinic, $P2_1$, and consists of slabs which are six layers of octahedra wide. Ca atoms within the slabs show a distorted cuboctahedron coordination whereas those at the borders show irregular coordination geometries. The distorted Ca environments results to a twofold superstructure found along [100]. The crystal is pseudo-merohedrally twinned, and the twin domains are related by a twin law given by a twofold axis about the **a** direction. The (Nb,Ti)O_6 octahedra show different degrees of distortions with the octahedra located at the center of the slabs having the least distortion in terms of bond distances and angles. This distortion grows towards the borders of the slabs. Partial ordering of Nb^{5+} and Ti^{4+} has been observed over the twelve octahedral coordinated (Nb,Ti) atomic sites, with the middle of the slab as the most preferred site for Ti^{4+}, while sites at the borders of the slabs have zero Ti occupancy. This preferential occupancy of Ti^{4+} has been found to be correlated with the distortion of the (Nb,Ti)O_6 octahedra with Ti^{4+} preferring the least distorted octahedral environment (Kunz and Brown; 1995). Valence computations for the different (Nb,Ti) sites in the slabs assumed occupied by either Nb or Ti have yielded valences for Nb and Ti close to their formal valences of 5.0 and 4.0 v.u., respectively. The good agreement suggests that Nb^{5+} and Ti^{4+} are equally well accommodated by all of the different oxygen environments and the different occupancies can only be the result of more or less distorted octahedral environments. Structure refinements indicate a composition of $Ca_6(Nb_{0.76}Ti_{0.24})_6O_{20}$. The non-stoichiometry in the refined composition and the insulating character of the material may be explained in terms of extra oxygen, vacancies on the cation sites, or by localization of the extra electrons in the partially filled $4d$ orbitals of Nb at the borders of slabs.

A good single crystal of $n = 5$ phase has also been found from the batch of crystals with nominal composition $Ca_5Nb_4TiO_{17}$ ($n = 5$), and its crystal structure has been successfully determined using Mo-K_α radiation of a rotating anode generator with an image plate detector. As in the of $Ca_5Nb_5O_{17}$ ($n = 5$) case, the crystal structure is monoclinic, $P2_1/c$, and comprises of slabs of corner-shared (Nb,Ti)O_6 octahedra that are five layers wide. Bond distance computations have shown that

the distortion of the (Nb,Ti)O_6 octahedra is minimal in the middle of the slabs and increases towards the borders of the slabs. Partial ordering has also been found for Ti ions as in the $n = 6$ case, with Ti ions preferentially occupying the sites in the middle of the slabs. This preferential occupation of Ti ions is consistent with local charge neutrality within the $Ca_5Nb_4TiO_{17}$ substructure. Nb^{5+} tends to be more concentrated at the borders of the slabs where there are unshared bonds of O^{2-} while the presence of Ti^{4+} favors electroneutrality of the $CaTiO_3$ subunit within the slabs. This result is in agreement with the study of Kunz and Brown (1995) which has shown that Nb^{5+} is associated with more highly distorted environment than Ti^{4+}. Computed valences for Nb ions and Ti ions are in good agreement with their formal valences of 5.0 and 4.0 v.u., respectively. This indicates that both Nb and Ti ions are equally well accommodated by the different oxygen environments at different (Nb,Ti) sites of the slabs, and that the observed partial ordering of Nb and Ti over the six crystallographically independent sites can only be the result of the different distortions of the octahedral environment as what has been found for the $n = 6$ case.

The similarity in the general features of these perovskite-related compounds suggests the idea that a common structural model may be used to describe all the crystal structures within a particular homologous series. Recently, it has been proposed that the different compounds within a homologous series can be described by a unified structure model employing the superspace approach (Perez-Mato et al.; 1999). The superspace approach treats the slabs of octahedra as stacking of atomic layers separated by a spacer where there is a vacant atomic layer. The similarity and the regularity between the stacking sequences for different composition supports this idea (Elcoro et al.; 2001). The crystal structures of different compounds, i.e. different n, are obtained from a systematic variation of the modulation wave vectors and of the widths of the discontinuous step-like functions that are used to describe the occupational modulations of the atoms. The basic structure and the symmetry — as specified by a superspace group — are common to all compounds of a homologous series. The last part of this thesis has contributed to examine the validity of this superspace approach.

The superspace approach has been applied to provide an alternative description of the crystal structures of $Ca_5Nb_4TiO_{17}$ ($n = 5$) and $Ca_6(Nb,Ti)_6O_{20}$ ($n = 6$). The same superspace model has been used as starting model for the structure refinements

in (3+1) dimensions for the two compounds. The superspace refinements assume that the crystal structures of the two compounds can be characterized as commensurately modulated structures consisting of discontinuous atomic domains described by occupational crenel functions and by harmonic displacive functions. Structure refinements in superspace have demonstrated the validity as well as the efficiency of the superspace approach as much smaller number of parameters are required to get similar fits to the data as compared to the three-dimensional refinements. The displacive modulation functions for the two compounds exhibit similarities, but in general are not identical for the two compounds. In particular, the refined functions for the atomic displacement modulations possess more parameters in the case of $n = 6$ than in $n = 5$. The slight difference in the superspace models arises so as to accommodate the different supercell models of these two compounds in three-dimensional space. Thus, it indicates that the idea of a unified superspace model does not extend towards the precise atomic positions for different compounds within the homologous series $Ca_n(Nb,Ti)_nO_{3n+2}$. For the Nb/Ti occupation, the partial ordering of (Nb,Ti) for the different sites in the slabs as observed in the supercell refinements have been reproduced in the superspace refinements. The higher quality of the superspace refinement is illustrated by the computed valences for (Nb,Ti) at the different sites where the obtained valences for Nb and Ti for all the different sites in the slabs are much closer to their formal valences. For $Ca_6(Nb,Ti)_6O_{20}$ ($n = 6$) the superspace model offers a natural explanation for the pseudo inversion symmetry, as it has been previously noticed in the supercell structure.

This thesis has described the crystal structures of the homologous series $Ca_n(Nb,Ti)_nO_{3n+2}$ with $n = 5$ and 6 using two different approaches. On one hand, using the conventional three-dimensional crystallographic approach, the cell parameters and the space group for each compound have been specified separately for each composition. On the other hand, using the superspace approach alternative descriptions of the crystal structures of these compounds have been obtained employing the same superspace model with the same superspace group as starting model for the the two compounds. Comparison of structure refinements between the two approaches clearly favors the superspace approach. This is confirmed by its efficiency and its flexibility to represent in a simple manner the symmetry-allowed atomic deviations from the ideal model. The idea of a unified model, however, does not extend towards displacive modulation functions. Thus, it can be expected that for other compo-

sitions within this homologous series, e.g. $n = 4$, 4.5, or 7, the same superspace model can be applied as starting model in the superspace refinement, but that the relevant harmonics for the description of the atomic displacement modulations will be different.

Kapitel 10

Zusammenfassung

In dieser Arbeit werden die Kristallstrukturen bei Raumtemperatur der Perovskit-artigen Materialien der homologen Serie $A_nB_nO_{3n+2}$ behandelt, wobei A = Ca, B = Nb oder Ti und $n = 5$ bzw. 6 sind. Das Bauprinzip der Kristallstrukturen dieser Verbindungen ist für alle n gleich: Die Kristallstrukturen können als Stapelung von Schichten eckenverknüpfter BO_6-Oktaeder entlang der [110]-Richtung der kubischen Perowskitstruktur beschrieben werden. Diese Schichten werden durch zusätzliche Sauerstoffschichten voneinander getrennt, wobei benachbarte Schichten gegenseitig entlang der **a**-Richtung um die Hälfte der Raumdiagonalen eines Oktaeders verschoben sind. Die einzelnen Schichten wiederum sind aus Oktaederschichten aufgebaut. Die Anzahl der Oktaederschichten n in einer Schicht (die Schichtdicke) bestimmt den Strukturtyp, der somit abhängig von der Zusammensetzung ist.

Drei Verbindungen wurden untersucht, d.h. ihre genauen Kristallstrukturen unter Anwendung der Röntgenstrahl-Einkristallbeugung ermittelt: $Ca_5Nb_5O_{17}$ ($n = 5$), $Ca_5Nb_4TiO_{17}$ ($n = 5$) und $Ca_6(Nb,Ti)_6O_{20}$ ($n = 6$). Da die Gitterparameter entlang der Stapelrichtung der Oktaederschichten typischerweise sehr groß sind, wurden Flächendetektoren (Bildplatte und CCD) eingesetzt, um innerhalb eines angemessenen Zeitraums (mehrere Tage) einen guten Datensatz für die Strukturanalyse zu bekommen. Der Einzatz von Synchrotronstrahlung (bzw. Mo-Kα-Strahlung eines Drehanodengenerators) ermöglichte auch die Datensammlung der schwachen Überstrukturreflexe.

Die bisherigen Strukturanalysen dieser Verbindungen haben hauptsächlich das Bauprinzip als Stapelung von Oktaederschichten bestimmt, ohne die Atomlagen oder die Verkippungen der Oktaeder zu geben (Nanot et al.; 1979, 1983). Die Kenntnis

der exakten Kristallstruktur liefert aber genaue Daten über die Atomlagen und thermische Parameter (ADP), welche für eine Vorhersage der physikalischen und chemischen Eigenschaften dieser Verbindungen unabdingbar sind. Diese Daten wurden in der vorliegenden Arbeit erstellt. Die daraus ermittelten Bindungsabstände und Bindungswinkel liefern einen wichtigen Einblick über Verkippung und Verzerrung der Oktaeder an den verschiedenen Positionen innerhalb der Schichten. Die berechneten Bond Valence Sums (Brese and O'Keeffe; 1991) für die einzelnen (Nb,Ti) Atome in den Schichten liefern nützliche Informationen über Kristallchemie und elektrische Eigenschaften dieser Verbindungen.

Die Kristallstruktur von $Ca_5Nb_5O_{17}$ ($n = 5$), das eine diamagnetische, elektrisch leitende Verbindung ist, wurde mittels Synchrotronstrahlung und CCD-Detektor erfolgreich bestimmt und beschrieben. Das Gitter ist monoklin, die Raumgruppe $P2_1/c$. Die Schichten bestehen aus jeweils fünf Oktaederschichten. Die Verschiebung der Schichten zueinander ergibt eine stark verzerrte Koordination der Ca-Atome, die sich am Rand der Schichten befinden. Diese werden in unregelmäßiger Geometrie von sieben O-Atomen koordiniert, während die Koordination der Ca-Atome im Innern der Schicht mit einem verzerrten Kuboktaeder (zwölf-fache Koordination) beschrieben werden kann. Die verzerrte Koordination der Ca-Atome resultiert in einer lokalen Spannung in den Schichten, die durch eine kommensurable Modulation der Struktur gelöst wird. Die dadurch entstehende zweifache Überstruktur entlang [100], d.h. die Verdopplung der Periodizität in der **a**-Richtung, kann durch die Verkippung der Oktaeder entlang der *a*-Achse erklärt werden, wobei diese Verkippung in Antiphase zu der entlang der *c*-Achse steht. Auch die NbO_6-Oktaeder haben eine verzerrte Umgebung, wobei die Verzerrung der Oktaeder mit der Position in den Schichten variiert. Die Berechnung der Bindungslängen und Bindungswinkel ergab, dass die NbO_6-Oktaeder im Inneren der Schichten weniger und die am Rand der Schichten mehr verzerrt sind. Die berrechnete Wertigkeit der Nb-Atome am Rand der Schichten liegt nahe der formalen Wertigkeit von 5.0 v.u., während sie zur Mitte der Schichten hin abnimmt. Dies zeigt an, dass die zusätzlichen Elektronen in den 4*d*-Orbitalen der Nb-Atome hauptsächlich in den Nb-Lagen im Inneren der Schichten eingebaut sind. Die elektrische Leitung in diesen Verbindungen findet daher hauptsächlich im Inneren der Schichten, in der die NbO_6-Oktaeder am wenigsten verzerrt sind statt. Für die verwandte Verbindung $Sr_5Nb_5O_{17}$ ($n = 5$) haben Winkel-aufgelöste Photoemission (angle-resolved photoemission studies, ARPES)

und Bandstrukturberechnungen gezeigt, dass der größte Beitrag zur Zustandsdichte der besetzten Zustände an der Fermikante in dieser Verbindung von den am wenigsten verzerrten Oktaedern kommt (Kuntscher et al.; 2000, 2002, 2004).

Für die Verbindung mit der nominellen Zusammensetzung $Ca_5Nb_4TiO_{17}$ ($n = 5$) wurden mehrere Einkristalle präpariert. Es hat sich aber gezeigt, dass die Synthese dieses Materials, das ein Isolator ist, ein Phasengemisch ergab und auch Kristalle der Zusammensetzung $n = 6$ enthielt, die eine gute Qualität hatten. Einer dieser Kristalle mit $n = 6$ wurde mit Synchrotronstrahlung und CCD-Detektor vermessen und seine Kristallstruktur bestimmt. Das Gitter ist monoklin die Raungruppe $P2_1$. Die Struktur besteht aus Schichten, die aus jeweils sechs Oktaederschichten zusammengesetzt sind. Ca-Atome im Inneren der Schichten besitzen eine verzerrte kuboktaedrische Koordination, während Ca-Atome am Rand der Schicht eine unregelmäßige Koordination aufweisen. Diese Verzerrung der Ca-Umgebung ergibt eine zweifache Überstruktur entlang [100]. Der Kristall ist pseudo-merohedrisch verzwillingt, die Zwillingsdomänen sind mit einer zweizähligen Drehachse entlang der **a**-Richtung verknüpft. Die (Nb,Ti)O_6-Oktaeder zeigen einen unterschiedlichen Grad an Verzerung, wobei die Oktaeder im Schichtinneren die kleinste Verzerrung in Hinblick auf Bindungslängen und Bindungswinkel haben. In Richtung Schichtrand wird dann die Verzerrung größer. Es wurde eine partielle Ordnung der Nb^{5+}- und Ti^{4+}-Ionen über die zwölf oktaedrisch-koordinierten (Nb,Ti)-Lagen beobachtet, die Ti^{4+}-Ionen bevorzugen die Lagen im Inneren der Schicht, an den Rändern ist die Besetzung der (Nb,Ti)-Lagen mit Ti gleich null. Diese Besetzung der Ti^{4+}-Ionen hängt mit der Verzerrung der (Nb,Ti)O_6-Oktaeder zusammen, Ti^{4+}-Ionen bevorzugen eine unverzerrte Oktaedergeometrie (Kunz and Brown; 1995). Die Berechnung der Valenz der verschiedenen (Nb,Ti)-Plätze in den Schichten ergibt Valenzen für Nb und Ti nahe an ihren formalen Wertigkeiten von 5.0 bzw. 4.0 v.u., wobei davon ausgegangen wurde, dass die Plätze entweder von Nb oder von Ti belegt sind. Diese gute Übereinstimmung legt nahe, dass sowohl die Nb^{5+}- als auch die Ti^{4+}-Ionen in gleicher Weise in den mehr oder weniger verzerrten Sauerstoffoktaedern untergebracht werden können, die unterschiedliche Besetzung also ein Ergebnis der verschiedenen Umgebungen sein muss. Die Strukturanalyse ergab, dass die genaue Zusammensetzung $Ca(Nb_{0.76}Ti_{0.24})O_{3.33}$ ist. Die Nicht-Stoichiometrie in der verfeinerten Zusammensetzung und der isolierende Charakter des Materials kann mit zusätzlichen O-Atomen, Leerstellen auf den Kationenplätzen oder durch den Ein-

bau der zusätzlichen Elektronen in die teilweise gefüllten 4*d*-Orbitale der Nb-Atome an den Rändern der Schichten erklärt werden.

Aus dem Ansatz mit der nominellen Zusammensetzung $Ca_5Nb_4TiO_{17}$ konnte auch ein Kristall guter Qualität mit $n = 5$ gefunden werden, die Struktur wurde unter Verwendung von Mo-Kα-Strahlung eines Drehanodengenerators und eines Bildplattendetektors gelöst. Wie im Falle $Ca_5Nb_5O_{17}$ ($n = 5$) ist das Gitter monoklin, die Raumgruppe $P2_1/c$. Die Struktur besteht aus Schichten eckenverknüpfter (Nb,Ti)O_6-Oktaeder, jede Schicht ist wiederum aus fünf Oktaederschichten aufgebaut. Die Berechnung der Bindungslängen und Bindungswinkel zeigt, dass die Verzerrung der (Nb,Ti)O_6 Oktaeder im Inneren der Schichten minimal ist und zum Rand hin zunimmt. Wie bei $n = 6$ ist eine partielle Ordnung der Ti-Ionen vorhanden, die bevorzugt die Plätze im Schichtinneren einnehmen. Diese Ordnung ist im Einvernehmen mit lokaler Ladungsneutralität in der $Ca_5Nb_4TiO_{17}$-Untertruktur. Die Nb^{5+}-Ionen konzentrieren sich mehr an den Rändern der Schichten, an denen sich auch die ungesättigten Bindungen der O^{2-}-Ionen befinden, während die Anwesenheit der Ti^{4+}-Ionen die Elektroneutralität der $CaTiO_3$-Untereinheit im Inneren der Schichten begünstigt. Dies ist in Übereinstimmung mit den Untersuchungen von Kunz and Brown (1995), die zeigten, dass die Nb^{5+}-Ionen mit einer stärker verzerrten Umgebung asoziiert sind, als die Ti^{4+}-Ionen. Die Berrechnung der Valenz für die Nb- und Ti-Ionen zeigt eine gute Übereinstimmung mit den formalen Valenzen von 5.0 bzw. 4.0 v.u. Dies lässt vermuten, dass die Nb^{5+}- und Ti^{4+}-Ionen gleichermaßen in den verschiedenen verzerrten Sauerstoffumgebungen der (Nb,Ti)-Lagen eingebaut werden können und die partielle Ordnung auf den sechs kristallographisch-unabhängigen Plätzen in den Verzerrungen der Oktaederumgebungen begründet sein muss.

Die Ähnlichkeit der allgemeinen Bauprinzipien dieser Perowskit-artigen Verbindungen unterstützt die Idee, ein gemeinsames Strukturmodell aufzustellen, das dann alle Strukturen innerhalb einer homologen Serie beschreiben kann. Kürzlich wurde vorgeschlagen, dass so ein gemeinsames Strukturmodell unter Anwendung der Superraum-Methode aufgestellt werden kann (Perez-Mato et al.; 1999). In der Superraum-Methode werden die Schichten nicht mehr als Stapelung von Oktaederschichten, sondern als Stapelung atomarer Schichten aufgefasst, die durch eine leere Schicht, d.h. eine fehlende Schicht, voneinander getrennt sind. Die Ähnlichkeit und Regelmäßigkeit zwischen den Stapelfolgen der unterschiedlichen Zusammensetzungen unterstützt diese Idee (Elcoro et al.; 2001). Die Kristallstrukturen der verschie-

den Verbindungen, d.h. unterschiedliches n, werden dann durch eine systematische Änderung des Modulationswellenvektors und der Breite der diskontinuierlichen, stufenartigen Funktionen, der Besetzungsmodulationen der Atomen beschrieben. Die Referenzstruktur und die Symmetrie - im vorliegenden Fall beschrieben durch eine Superraumgruppe - ist die Gleiche für alle Verbindungen der homologen Serie. Der letzte Teil der vorliegenden Arbeit untersucht die Gültigkeit dieses Modells mit der Superraummethode.

Die Superraummethode wurde angewandt, um ein alternatives Strukturmodell der kristallstrukturen $Ca_5Nb_4TiO_{17}$ ($n = 5$) und $Ca_6(Nb,Ti)_6O_{20}$ ($n = 6$) aufzustellen. In beiden Fällen wurde das gleiche Startmodell für die Verfeinerung der Struktur im (3+1)-dimensionalen Superraum verwendet. Die Strukturen werden als kommensurabel modulierte Strukturen angenommen, bestehend aus diskontinuierlichen atomaren Domänen, die mit Crenel-Funktionen (Stufenfunktionen) als Besetzungsmodulationen und displaziven harmonischen Funktionen beschrieben werden können. Das Ergebnis der Strukturverfeinerung bestätigte sowohl die Gültigkeit, als auch die Effizienz der Superraum-Methode, da wesentlich weniger Parameter notwendig sind, um eine Anpassung an der gemessenen Daten mit gleicher Güte zu bekommen. Die Funktionen der displaziven Modulationen zeigen große Ähnlichkeiten für beide Verbindungen, sind aber nicht identisch. Für die Verbindung $n = 6$ werden mehr Parameter benötigt als für $n = 5$, womit die unterschiedlichen drei-dimensionalen Überstrukturen dieser beiden Verbindungen angepasst würden. Dies zeigt, dass ein gemeinsames, allgemein gültiges Superraummodell, das genaue Atompositionen liefert, nicht möglich ist für die homologe Verbindung $Ca_n(Nb,Ti)_nO_{3n+2}$. Die partielle Ordnung von (Nb,Ti) auf den unterschiedlichen Plätzen in den Schichten, wie sie in den Überstrukturen beobachtet wurden, konnten mit der Superraummethode reproduziert werden. Die bessere Qualität der Verfeinerung im Superraum ist dadurch gezeigt, dass die berechneten Valenzen für (Nb,Ti) auf allen unterschiedlichen (Nb,Ti)-Lagen in den Schichten näher an den formalen Valenzen liegen. Für $Ca_6(Nb,Ti)_6O_{20}$ ($n = 6$) bietet das Superraum-Modell eine natürliche Erklärung für die Pseudo-Inversionssymmetrie, wie sie für die Überstruktur im drei-dimensionalen Raum beobachtet wurde.

In dieser Arbeit wurden die Kristallstrukturen der homologen Serie $Ca_n(Nb,Ti)_nO_{3n+2}$ mit $n = 5$ und 6 beschrieben, unter Anwendung zweier verschiedener Ansätze. Zum einen wurden die Strukturen mit der klassischen kristallogra-

phischen Methode im drei-dimensionalen Raum beschrieben, wobei für jede Struktur jeweils Gitterparameter und Raumgruppe bestimmt werden mussten. Zum anderen wurden die Strukturen mit der Superraummethode beschrieben, bei der ein einheitliches Startmodell für die Verfeinerung beider Verbindungen benutzt werden konnte. Der Vergleich beider Methoden favorisiert die Superraum-Methode, was sich in der Effizienz und der Flexibilität niederschlägt, auf einfache Weise die Abweichungen der Atome von den Idealpositionen zu beschreiben. Jedoch ist es aufgrund der displaziven Modulationsfunktionen nicht möglich, ein gemeinsames Strukturmodell zu erstellen. Es kann erwartet werden, dass für andere Zusammensetzungen innerhalb der homologen Serie, z.B. $n = 4$, 4,5 oder 7, das gleiche Startmodell zur Strukturverfeinerung verwendet werden kann, sich aber die relevanten harmonischen Funktionen zur Beschreibung der displaziven Modulationen unterscheiden.

Appendix A

Sample Output of SMART

Results of the least-squares refinement performed by SMART for Run # 00A of the compound $Ca_5Nb_5O_{17}$ ($n = 5$) measured at beamline F1 of Hasylab

−0.12852930	−0.02425236	−0.00610414
−0.01394619	0.17367242	−0.00910631
0.01430773	−0.04899127	−0.02925792

Lattice parameters & Standard deviations:

7.7452	5.4923	32.2438	90.001	96.967	89.986	1361.49
0.0019	0.0009	0.0059	0.007	0.010	0.013	0.73

Standard deviations corrected for GOF:

0.0014	0.0007	0.0044	0.005	0.007	0.010	0.55

Histograms:

	.00	.05	.10	.15	.20	.25	.30	.35	.40	.45	+Inf
H	189	0	0	0	0	0	0	0	0	0	0
K	189	0	0	0	0	0	0	0	0	0	0
L	189	0	0	0	0	0	0	0	0	0	0
Omega	189	0	0	0	0	0	0	0	0	0	0

	.00	.25	.50	.75	1.00	1.25	1.50	1.75	2.00	2.25	+Inf
X	189	0	0	0	0	0	0	0	0	0	0
Y	187	2	0	0	0	0	0	0	0	0	0

	H	K	L	Omega	X	Y
AVG	0.000	0.000	0.000	0.000	0.000	0.000
RMS	0.001	0.001	0.004	0.012	0.063	0.081

Worst Agreements (worst RLV error):

#	H	K	L	dRLV	dOMEGA
61	2.00	1.00	-29.00	0.0010	0.035
188	2.00	2.00	-18.99	0.0009	-0.035
1	2.00	4.00	-13.99	0.0008	0.011
34	2.00	0.00	-23.99	0.0006	0.021
17	2.00	3.00	-21.00	0.0006	-0.012
10	2.00	4.00	-16.00	0.0006	0.006
165	3.00	3.00	-19.00	0.0005	-0.007
111	0.00	3.00	-20.00	0.0005	-0.026
68	1.00	4.00	-18.00	0.0005	0.010
7	3.00	2.00	-26.00	0.0005	-0.012

Detector corrections:	X-Cen	Y-Cen	Dist	Pitch	Roll	Yaw
(additive)	-0.645	1.768	0.057	0.176	-0.559	0.057

Eulerian angles:	164.828	163.102	22.237
Omega, Chi zeros (deg):	-0.0289	0.0070	
Crystal XYZ:	0.0000	0.0000	0.0000

Nonlinear refinement:	StartingRes	FinalRes	GOF	#Cycles	Code
	2.30137E+02	1.57203E+00	0.57	4	0

#	Flags	H	K	L	Swing	Omega	Phi	Chi	X	Y	Inorm	I/Sig
1	ACHS	2	4	-14	20.000	0.138	0.000	54.000	137.03	17.11	3846.9	35
		+.00	+.00	-.01		0.011			0.25	0.21		
2	ACHS	2	2	-20	20.000	0.953	0.000	54.000	133.81	191.66	13851	67
		+.00	+.00	+.00		-0.004			-0.03	-0.05		
3	ACHS	2	-2	-14	20.000	1.185	0.000	54.000	306.48	458.23	20492	81
		+.00	+.00	+.01		-0.013			-0.15	0.00		
4	ACHS	2	0	-20	20.000	1.311	0.000	54.000	186.82	329.81	15517	70
		+.00	+.00	+.00		0.002			0.06	0.04		
5	ACHS	1	1	-14	20.000	1.599	0.000	54.000	240.56	229.62	2565.8	28
		+.00	+.00	+.00		-0.011			0.03	-0.03		
.												
.												
.												
189	ACHS	3	1	-25	20.000	359.888	0.000	54.000	87.39	289.05	9402.6	55
		+.00	+.00	+.00		-0.006			-0.03	-0.06		

lines # 6–188 have been omitted for clarity.

Appendix B

Sample Output of SAINT

Excerpts from the results of data reduction by SAINT for Run # 04 of the compound $Ca_5Nb_5O_{17}$ ($n = 5$) measured at beamline F1 of Hasylab

Overall Integration Statistics	
Total HKLs predicted:	1867
# Outside active pixel mask or	
within 5 pixels of frame edge:	282
# Outside frame limits:	22
# Outside resolution limit:	0
# with absolute HKL > 511:	0
# Below worst I/sigma threshold:	0
# Exceeding dynamic range:	0
# Exceeding frame queue size:	0
# with too many components:	0
# Good reflections written:	1563
Twin overlaps written:	0
Twin partial overlaps written:	0
Number excl. partial overlaps	
(these are the reflections	
used in the stats below):	1563
# From write-behind cache (WBC):	0
# Partial overlaps from WBC:	0
# Exceeding queue size from WBC:	0
# with > 4 components from WBC:	0
Average Intensity:	4.766E+03
Average I/sigma:	31.174
% over "strong"threshold:	10.04
% less than 2 sigma:	21.05
% which spanned more than 1 frame:	76.58

Average X,Y,Z positional errors:	-0.05	0.01	-0.02
RMS X,Y,Z positional errors:	0.26	0.25	0.17
% X,Y,Z more than 0.5 pixel:	4.80	4.48	1.47
% X,Y,Z more than 1 pixel:	0.58	0.64	0.06

Avg % profile volume populated:	100.00
Avg % profile volume integrated:	9.57
X fraction of prof. volume used:	88.89
Y fraction of prof. volume used:	88.89
Z fraction of prof. volume used:	88.89
Max profile % on X boundaries:	0.25
Max profile % on Y boundaries:	0.26
Max profile % on Z boundaries:	1.04
Number of filled spots:	0
Average fraction filled:	0.0000
Average spot shape correlation:	0.825
RMS spot shape correlation:	0.880

Profile Shape Correlation

I/sigma from	to	Correl	+/-	#
0.00	1.00	0.33	0.276	208
1.00	2.00	0.60	0.226	121
2.00	4.00	0.81	0.134	149
4.00	8.00	0.95	0.079	185
8.00	16.00	0.98	0.012	267
16.00	32.00	0.99	0.005	410
32.00	64.00	0.99	0.004	223
64.00	128.00	0.00	0.000	0
128.00	256.00	0.00	0.000	0

Total integration time (sec):	68.813
Total time in cell LS (sec):	0.703
Per-frame integration time (sec):	0.095

Integration completed normally ========== 01/13/05 17:46:08

Applying profile correlation filter from unsorted.raw to corrfilt.raw
Scale of 1.000 will be applied to LS-fit intensities

Number of reflections read =	1563	
# Rejected due to poor spot shape; # written:	8	1555
Number of LS-fit intensities scaled:	0	

Sorting Reflections File ==========01/13/05 17:46:08
canbo04

Sorting input files: corrfilt.raw

Sorting to output file canbo04.raw
Point group sequence #, name: 3, "2/m(B-unique)"
Number of symmetry operators: 4

$$\begin{matrix}1&0&0\\0&1&0\\0&0&1\end{matrix}\qquad\begin{matrix}-1&0&0\\0&1&0\\0&0&-1\end{matrix}\qquad\begin{matrix}-1&0&0\\0&-1&0\\0&0&-1\end{matrix}\qquad\begin{matrix}1&0&0\\0&-1&0\\0&0&1\end{matrix}$$

Computing Reflection File Statistics ========== 01/13/05 17:46:08
canbo04

1555 reflections read from corrfilt.raw
1555 reflections written to canbo04.raw

Orientation read from canbo04.p4p:
Cell constants computed from input file:

7.746	5.490	32.233	90.014	96.965	89.985

Coverage Statistics for canbo04.raw

Angstrms	#Obs	Theory	%Compl	Redund	Rsym	Pairs	%Pairs	Rshell	#Sigma	%<2s
to 1.270	153	828	18.48	1.29	0.010	45	5.43	0.010	36.65	18.2
to 1.068	313	1339	23.38	1.31	0.016	96	7.17	0.027	34.17	21.8
to 0.954	453	1843	24.58	1.30	0.017	134	7.27	0.020	31.40	19.1
to 0.877	596	2378	25.06	1.28	0.018	166	6.98	0.027	32.01	16.6
to 0.820	722	2901	24.89	1.27	0.019	192	6.62	0.025	30.35	17.1
to 0.775	850	3378	25.16	1.25	0.019	209	6.19	0.034	28.53	22.1
to 0.739	966	3906	24.73	1.23	0.019	224	5.73	0.021	28.22	22.9
to 0.708	1087	4399	24.71	1.21	0.019	233	5.30	0.013	22.30	30.0
to 0.683	1199	4886	24.54	1.20	0.019	242	4.95	0.052	22.12	24.0
to 0.660	1303	5420	24.04	1.19	0.019	252	4.65	0.038	24.56	24.6

Averaged "local"cell least squares refinement ========== 01/13/05 17:46:13
Local refinement results for component 1
Number of local refinements averaged: 3

Averaged orientation ("UB") matrix:

$$\begin{matrix}-0.1285254 & -0.0240812 & -0.0059955\\ -0.0138914 & 0.1736868 & -0.0091162\\ 0.0138443 & -0.0491406 & -0.0292733\end{matrix}$$

Weighted average cell constants:

A	B	C	Alpha	Beta	Gamma	Vol
7.7484	5.4914	32.2463	89.999	96.959	89.999	1361.96
0.0006	0.0006	0.0023	0.003	0.004	0.004	0.32

Std deviations of the 3 input local LS results:

0.0004	0.0001	0.0017	0.008	0.006	0.012	0.13

Range of reflections used:

Worst res	Best res	Min 2Theta	Max 2Theta
1.8194	0.6624	22.504	64.811

Crystal system constraint: 0(Unconstrained)
Parameter constraint mask: 512

Detector corrections:	X-Cen	Y-Cen	Dist	Pitch	Roll	Yaw
	-0.174	3.392	0.048	0.191	-0.542	0.007

Unconstrained global unit cell refinement ========== 01/13/05 17:46:13

Performing final unit cell least squares on file canbo04._ma
Input file contains 157 reflections

Processing component 1 of 1 Input file contains 157 reflections for this component
Maximum allowed reflections = 8192
One reflection will be stored in memory per 1 reflections read

Orientation least squares, component 1 (157 reflections)...
Orientation ("UB") matrix:

−0.1285376	−0.0241204	−0.0060009
−0.0139550	0.1737114	−0.0091026
0.0138421	−0.0490517	−0.0292830

A	B	C	Alpha	Beta	Gamma	Vol
7.7477	5.4912	32.2415	90.000	96.970	89.993	1361.56
0.0014	0.0013	0.0053	0.008	0.010	0.008	0.69

Corrected for goodness of fit:

0.0007	0.0007	0.0028	0.004	0.005	0.004	0.37

Range of reflections used:

Worst res	Best res	Min 2Theta	Max 2Theta
1.8193	0.6624	22.505	64.815

Crystal system constraint: 0(Unconstrained)

Parameter constraint mask: 512

Eulerian angles:	165.475	163.165	21.565	
Goniometer zeros (deg):	0.0000	-0.0429	0.0000	0.1104
Crystal translations (pixels):		0.0000	0.0000	0.0000

Detector corrections:	X-Cen	Y-Cen	Dist	Pitch	Roll	Yaw
	-0.160	3.408	0.047	0.206	-0.534	0.015

Refinement statistics:	StartingRes	FinalRes	GOF	#Cycles	Code
	1.94182E+04	1.29722E+02	0.29	2	0

New orientation is in canbo0m.p4p
End global unit cell refinement ==================== 01/13/05 17:46:13

Appendix C

Sample Output of SADABS

Summary of the results of absorption correction by SADABS for the compound $Ca_5Nb_5O_{17}$ ($n = 5$) measured at beamline F1 of Hasylab

SADABS - Bruker/Siemens area detector absorption and other corrections - V2.03

Equivalent reflections defined according to point group 2/m
Reading batch 1 from file canbo00A.raw
Reading batch 2 from file canbo00B.raw
Reading batch 3 from file canbo01.raw
Reading batch 4 from file canbo02.raw
Reading batch 5 from file canbo03A.raw
Reading batch 6 from file canbo03B.raw
Reading batch 7 from file canbo04.raw
Reading batch 8 from file canbo94.raw
Reading batch 9 from file canbo05.raw
Reading batch 10 from file canbo06.raw
Reading batch 11 from file canbo07A.raw
Reading batch 12 from file canbo07B.raw
Reading batch 13 from file canbo08A.raw
Reading batch 14 from file canbo08B.raw
Reading batch 15 from file canbo09.raw
Reading batch 16 from file canbo10.raw
Reading batch 17 from file canbo18.raw
Reading batch 18 from file canbo19.raw
Reading batch 19 from file canbo20.raw
Reading batch 20 from file canbo21.raw
Reading batch 21 from file canbo22A.raw
Reading batch 22 from file canbo22B.raw

Mean and maximum errors in direction cosine check function = 0.000 0.001

The mean error should not exceed 0.005, and is usually caused by matrix changes during data processing.

Maximum 2-theta = 71.05 deg. Approximate wavelength = 0.71008 Angstroms

PART 1 - Refinement of parameters to model systematic errors

Thresholds should now be specified for excluding reflections from the parameter refinement; these reflections may still be corrected and included in the final output .hkl file

32652 Reflections of which 5663 unique; 2.08 data per frame

Redundancy:	1	2	3	4	5	6	7	8	9+
Number of groups:	295	529	893	825	727	490	351	311	1242

Mean(I/sigma):	-inf	0	1	2	3	5	10	15	20	+inf
Number of groups:	698	453	312	200	181	712	496	389	2222	

Settings for parameter refinement:

Maximum resolution = 0.1000 A
(Intensity/sigma) threshold = 3.000
Restraint esd for equal adjacent scale factors = 0.0020
Maximum odd and even orders for spherical harmonics = 3 6

25210 Reflections employed for parameter determination
Effective data to parameter ratio = 1.34

R(int) = 0.0773 (selected reflections only, before parameter refinement)

Cycle	R(incid)	R(diffr)	Mean wt.
1	0.0584	0.0522	0.9289
2	0.0456	0.0440	0.9424
3	0.0427	0.0418	0.9446
4	0.0414	0.0408	0.9455
5	0.0406	0.0401	0.9460
.			
.			
.			
100	0.0364	0.0364	0.9490

R(int) = 0.0364 (selected reflections only, after parameter refinement)

PART 2 - Reject outliers and establish error model

Rejected reflections are ignored in the statistics and Postscript plots (except the detector diagnostics) and in the output .hkl file Before applying rejections there are:
32652 total and 5663 unique reflections assuming Friedel's law.

32528 total and 5660 unique reflections left after $|\ I- < I >|/su$ test

g = 0.0464 gave best error model; g set to 0.0464 for statistics and data output

Run	2-theta	R(int)	Incid.factors	Diffr.factors	K	Total	I>2sig(I)
1	20	0.0448	0.867-1.081	0.889-1.352	1.015	585	456
2	20	0.0487	1.189-1.472	0.885-1.115	1.098	316	243
3	20	0.0358	0.924-1.321	0.997-1.643	0.834	929	798
4	20	0.0337	0.861-1.476	0.909-1.342	0.907	910	680
5	45	0.0287	0.391-0.431	0.998-1.464	0.858	534	411
6	45	0.0294	0.784-1.085	0.885-1.274	0.923	2034	1667
7	45	0.0356	0.514-0.657	0.946-1.450	0.876	1553	1244
8	45	0.0335	0.824-1.070	0.947-1.193	0.912	1031	895
9	45	0.0339	0.716-1.073	0.936-1.428	0.910	2574	2233
10	45	0.0316	0.478-1.186	0.885-1.480	0.887	2587	2192
11	45	0.0406	0.677-0.785	1.098-1.443	0.983	1051	921
12	45	0.0329	0.632-1.014	1.080-1.671	0.974	3227	2799
13	30	0.0365	1.046-1.323	1.011-1.494	0.866	1007	851
14	30	0.0507	0.813-1.127	0.994-1.286	0.960	633	504
15	30	0.0376	0.848-1.239	1.030-1.629	0.904	1677	1420
16	30	0.0384	0.938-1.617	1.002-1.471	0.829	1649	1305
17	50	0.0295	0.633-0.734	0.887-1.501	0.864	1328	1064
18	30	0.0438	0.772-1.137	0.976-1.596	0.849	1755	1508
19	45	0.0319	0.777-0.897	0.998-1.488	0.848	2171	1941
20	45	0.0346	0.744-0.982	1.051-1.428	1.001	2515	2276
21	45	0.0348	0.848-1.115	0.982-1.522	0.922	1870	1516
22	45	0.0297	0.582-0.773	0.966-1.416	0.873	592	536

su = K * Sqrt[sigmaˆ2(I) + (g<I>)ˆ2] where sigma(I) is estimated by SAINT

The above statistics are based on all non-rejected data, ignoring reflections without equivalents when estimating R(int) and K.

PART 3 - Output Postscript diagnostics and corrected data

Diagnostic plots written to Postscript file canbort.eps
32528 Corrected reflections written to file canbort.hkl
Ratio of minimum to maximum apparent transmission: 0.529464
Lambda/2 correction factor = 0.0000

Appendix D

Sample Output of CRYSALIS RED

Summary of the data reduction by CrysAlis Red on Run #10 for the compound $Ca_5Nb_4TiO_{17}$ ($n = 5$) measured using MAR345 IP diffractometer at the Laboratory of Bayreuth

CRYSALIS DATA REDUCTION
(Version 1.171.27p5 beta (release 01-04-2005 CrysAlis171 .NET))

COMMAND LINE: dc red

TIME OF DATA REDUCTION FINALISING: Tue Jul 05 17:36:55 2005
CRYSTAL INFORMATION

UB - MATRIX:

−0.043988	−0.004193	−0.020539	(0.000004	0.000005	0.000001)
0.068240	−0.072727	−0.006301	(0.000003	0.000004	0.000001)
−0.044763	−0.106764	0.005089	(0.000003	0.000005	0.000001)

7.70637	(0.00028)	5.48786	(0.00020)	32.36053	(0.00125)
90.01997	(0.00303)	96.89380	(0.00308)	90.00082	(0.00292)

V = 1358.68

CELL: 7.70637 5.48786 32.36053 90.01997 96.89380 90.00082

RUN	Type of Scan	Start(deg)	End(deg)	# Frames
Run 1	Phi scan:	(0.000 - 180.000,600 frames, 45.000 sec)		
1	PHI	0.00000	180.00000	600
		at th=0.000, ka=0.000, om=0.000		
	Exp (s)	Omega(deg)	Theta(deg)	Kappa(deg)	Phi(deg)
	45.00000	56.50878	0.07711	-134.00000	n/a

I/Sigma	< 0	1	2	3	4	8	16	32	64	128	max
N(Refl)	314	470	676	915	1177	2286	3821	5616	7452	9009	11170
Percent	2.8	4.2	6.1	8.2	10.5	20.5	34.2	50.3	66.7	80.7	100.0

All reflections intensity statistics

intensity	#	mean F2	mean F2/sig(F2)	% >3*F2/sig(F2)
85867 - 2238	1595	11147.88	407.94	100.00
2238 - 781	1595	1313.84	118.25	100.00
781 - 372	1595	552.83	60.79	100.00
371 - 194	1595	275.29	34.58	100.00
194 - 100	1595	142.78	19.46	100.00
100 - 41	1595	67.63	9.73	100.00
41 - -36	1595	15.93	2.67	42.95
-37 - -47	5	-41.75	-4.25	0.00
85867 - -47	11170	1930.00	93.30	91.81

All reflections resolution statistics

resolution	#	mean F2	mean F2/sig(F2)	% >3*F2/sig(F2)
7.25 - 1.48	1595	2186.52	155.57	96.61
1.48 - 1.18	1595	2597.62	123.56	94.67
1.18 - 1.03	1595	2332.33	106.28	95.55
1.03 - 0.94	1595	1852.15	76.09	92.48
0.94 - 0.87	1595	2045.65	84.82	92.16
0.87 - 0.82	1595	1403.46	58.75	87.65
0.82 - 0.77	1595	1090.82	48.13	83.64
0.77 - 0.77	5	2395.68	66.74	60.00
7.25 - 0.77	11170	1930.00	93.30	91.81

All reflections cumulative resolution statistics

resolution	#	mean F2	mean F2/sig(F2)	% >3*F2/sig(F2)
7.25 - 1.48	1595	2186.52	155.57	96.61
1.48 - 1.18	3190	2392.07	139.56	95.64
1.18 - 1.03	4785	2372.16	128.47	95.61
1.03 - 0.94	6380	2242.16	115.38	94.83
0.94 - 0.87	7975	2202.85	109.26	94.29
0.87 - 0.82	9570	2069.62	100.85	93.19
0.82 - 0.77	11170	1929.79	93.31	91.82
0.77 - 0.77	5	1930.00	93.30	91.81
7.25 - 0.77	11170	1930.00	93.30	91.81

Scale applied to data: s = 1.000 (maximum obs: 85866.852)!

Without outlier rejection... Rint = 0.060; Rsigma = 0.006: data 11170 → merged 3382
With outlier rejection... Rint = 0.039; Rsigma = 0.006: data 10484 → merged 3382
With outlier rejection... Rejected total: 686, method kkm 667, method Blessing 19

Note: The Rint and Rsigma values are computed for redundant data only! Mean F2 and F2/sig(F2) are given for all measured values!

intensity		# measured	# kept	# unique	average redundancy	mean F2	mean F2/sig(F2)	Rint	Rsigma
77547 -	3691	1089	958	338	2.8	14793.11	499.97	0.028	0.002
3686 -	1342	1139	1045	338	3.1	2220.78	174.87	0.044	0.006
1340 -	704	1167	1098	338	3.2	973.99	93.48	0.059	0.012
703 -	406	1174	1104	338	3.3	545.65	60.14	0.076	0.019
406 -	256	1179	1118	338	3.3	326.30	39.56	0.089	0.028
159 -	98	1117	1062	338	3.1	126.47	16.84	0.157	0.067
98 -	55	1058	1008	338	3.0	74.51	10.66	0.229	0.107
55 -	28	1066	1014	338	3.0	40.42	5.76	0.373	0.192
28 -	-29	1017	978	338	2.9	14.05	2.12	0.674	0.389
77547 -	-29	11167	10481	3380	3.1	1908.46	93.01	0.039	0.006

Note: The Rint and Rsigma values are computed for redundant data only! Mean F2 and F2/sig(F2) are given for all measured values!

resolution (A)	# measured	# kept	# unique	average redundancy	mean F2	mean F2/sig(F2)	Rint	Rsigma
inf - 1.70	1054	1022	338	3.0	1605.88	147.74	0.029	0.004
1.70 - 1.34	1126	1094	338	3.2	2444.59	128.88	0.042	0.004
1.34 - 1.17	1133	1075	338	3.2	2968.11	137.41	0.028	0.004
1.17 - 1.06	1143	1081	338	3.2	2384.81	104.92	0.030	0.005
1.06 - 0.98	1158	1092	338	3.2	1942.30	88.06	0.027	0.006
0.98 - 0.92	1125	1054	338	3.1	2083.15	80.81	0.033	0.006
0.92 - 0.87	1155	1072	338	3.2	2091.69	86.12	0.039	0.006
0.87 - 0.83	1116	1034	338	3.1	1500.28	61.67	0.043	0.009
0.83 - 0.80	1101	1011	338	3.0	1073.29	48.30	0.051	0.012
0.80 - 0.77	1057	947	338	2.8	1097.02	48.62	0.119	0.013
inf - 0.77	11168	10482	3380	3.1	1930.34	93.32	0.039	0.006

Appendix E

Supplementary Materials for $\mathbf{Ca(Nb,Ti)O_{3.33}}$ ($n = 6$)

Table E.1: Fractional Atomic Coordinates, Occupancies, and Equivalent Isotropic Displacement Parameters (Å^2) of Nb and Ca Atoms in Ca(Nb,Ti)$O_{3.33}$

Atomic Site[a]	***x***	***y***	***z***	**Occupancy**[b]	$\mathbf{U}_{iso}$[c]
Nb1	0.40048(16)	0.2819(3)	0.06174(3)	0.980(6)	0.00629(16)
Nb2	0.90661(16)	0.2764(4)	0.06256(3)	0.995(7)	0.00775(16)
Nb3	0.44057(18)	0.754	0.13485(4)	0.837(7)	0.00716(18)
Nb4	0.94282(18)	0.7606(4)	0.13617(4)	0.791(7)	0.00743(18)
Nb5	0.9871(2)	0.2589(4)	0.21280(5)	0.470(7)	0.0078(2)
Nb6	0.4809(2)	0.2603(4)	0.21237(5)	0.493(7)	0.0081(2)
Nb7	0.0232(2)	0.7610(4)	0.28714(5)	0.470	0.0078
Nb8	0.5215(2)	0.7589(4)	0.28704(5)	0.493	0.0081
Nb9	0.06100(18)	0.2572(3)	0.36473(4)	0.791	0.00743
Nb10	0.55244(18)	0.2616(4)	0.36467(4)	0.837	0.00716
Nb11	0.09135(16)	0.7840(3)	0.43760(3)	0.995	0.00775
Nb12	0.60289(16)	0.7856(4)	0.43846(3)	0.980	0.00629
Ca1	0.1360(4)	0.8391(6)	0.02379(7)	1	0.0085(3)
Ca2	0.6332(4)	0.7696(6)	0.03489(8)	1	0.0145(3)
Ca3	0.6890(4)	0.2475(6)	0.13222(7)	1	0.0085(3)
Ca4	0.1952(4)	0.2544(7)	0.14357(8)	1	0.0181(4)
Ca5	0.7284(4)	0.7669(6)	0.20774(7)	1	0.0110(3)
Ca6	0.2330(4)	0.7484(7)	0.21727(8)	1	0.0156(4)
Ca7	0.7651(4)	0.2534(6)	0.28214(8)	1	0.0156
Ca8	0.2723(4)	0.2590(6)	0.29287(7)	1	0.0110
Ca9	0.8044(4)	0.7619(7)	0.35640(8)	1	0.0181
Ca10	0.3092(4)	0.7566(6)	0.36536(7)	1	0.0085
Ca11	0.3635(4)	0.2727(6)	0.46345(8)	1	0.0145
Ca12	0.8645(4)	0.3421(6)	0.47570(7)	1	0.0085

[a]Each Nb site was constrained to be fully occupied by a mixture of Nb and Ti with equal thermal parameters. Parameters restricted by pseudo-inversion symmetry to other parameters are given without standard uncertainty.

[b]Nb & Ti occupancies for each site sum up to 1.

[c]U_{iso} represents the isotropic displacement parameters for O-atoms and the equivalent isotropic displacement parameters for Nb/Ti and Ca which were anisotropically refined.

Table E.2: Fractional Atomic Coordinates, Occupancies, and Equivalent Isotropic Displacement Parameters (Å^2) of O Atoms in Ca(Nb,Ti)$O_{3.33}$

Atomic Site	***x***	***y***	***z***	**Occupancy**	$\mathbf{U}_{iso}$ [a]
O1	0.4148(12)	0.0811(18)	0.0214(2)	1	0.0098(10)
O2	0.8577(13)	0.0620(18)	0.0271(2)	1	0.0074(10)
O3	0.9226(11)	0.5391(16)	0.0315(2)	1	0.0036(9)
O4	0.3594(13)	0.5714(18)	0.0382(2)	1	0.0108(11)
O5	0.1602(12)	0.1822(18)	0.0689(2)	1	0.0090(9)
O6	0.6512(12)	0.3361(17)	0.0697(2)	1	0.0069(9)
O7	0.8699(12)	0.9691(18)	0.0991(2)	1	0.0090(10)
O8	0.4869(11)	0.9513(16)	0.0958(2)	1	0.0054(10)
O9	0.4119(12)	0.4555(17)	0.1118(2)	1	0.0049(10)
O10	0.9564(13)	0.4551(19)	0.1126(2)	1	0.0087(10)
O11	0.1913(12)	0.835(2)	0.1397(2)	1	0.0131(9)
O12	0.7041(12)	0.6702(17)	0.1454(2)	1	0.0081(9)
O13	0.9194(12)	0.0504(18)	0.1695(2)	1	0.0064(10)
O14	0.5055(12)	0.0432(19)	0.1714(2)	1	0.0083(10)
O15	0.0026(13)	0.5392(19)	0.1840(3)	1	0.0113(10)
O16	0.4353(13)	0.5424(19)	0.1857(2)	1	0.0099(11)
O17	0.2282(12)	0.1734(19)	0.2113(2)	1	0.0112(9)
O18	0.7323(12)	0.3239(19)	0.2156(2)	1	0.0093(9)
O19	0.5385(11)	0.9438(16)	0.2425(2)	1	0.0044(10)
O20	0.9481(12)	0.9565(18)	0.2445(2)	1	0.0100(11)
O21	0.4668(11)	0.4673(16)	0.2551(2)	1	0.0044
O22	0.0296(13)	0.4582(17)	0.2559(2)	1	0.0100
O23	0.2617(12)	0.8363(18)	0.2811(2)	1	0.0093
O24	0.7666(13)	0.6734(19)	0.2899(2)	1	0.0112
O25	0.9949(13)	0.040(2)	0.3160(3)	1	0.0113
O26	0.5750(13)	0.0382(19)	0.3177(2)	1	0.0099
O27	0.5015(12)	0.5467(18)	0.3291(2)	1	0.0083
O28	0.0810(12)	0.5368(17)	0.3272(2)	1	0.0064
O29	0.3069(12)	0.1832(17)	0.3533(2)	1	0.0081
O30	0.8000(12)	0.3255(19)	0.3592(2)	1	0.0131
O31	0.5997(11)	0.9415(16)	0.3845(2)	1	0.0049
O32	0.0400(13)	0.9506(18)	0.3876(2)	1	0.0087
O33	0.1231(12)	0.4654(19)	0.4005(2)	1	0.0090
O34	0.5280(11)	0.4712(16)	0.4008(2)	1	0.0054
O35	0.3369(12)	0.8593(17)	0.4293(2)	1	0.0069
O36	0.8436(13)	0.6829(18)	0.4300(2)	1	0.0090
O37	0.0822(12)	0.0538(16)	0.4639(2)	1	0.0036
O38	0.6354(12)	0.0801(18)	0.4574(2)	1	0.0108
O39	0.1395(13)	0.5550(17)	0.4749(2)	1	0.0074
O40	0.6028(13)	0.5787(18)	0.4770(2)	1	0.0098

[a] U_{iso} represents the isotropic displacement parameters.

Table E.3: Anisotropic Displacement Parameters (Å^2) of Nb/Ti and Ca Atoms in Ca(Nb,Ti)$O_{3.33}$

Atomic Site[a]	U_{11}	U_{22}	U_{33}	U_{12}	U_{13}	U_{23}
Nb1	0.0027(3)	0.0075(3)	0.0077(3)	-0.0004(6)	-0.0039(3)	-0.0005(5)
Nb2	0.0059(3)	0.0090(3)	0.0077(3)	0.0002(6)	-0.0025(3)	-0.0028(5)
Nb3	0.0055(3)	0.0072(3)	0.0080(3)	0.0015(7)	-0.0033(4)	0.0003(5)
Nb4	0.0055(3)	0.0075(3)	0.0084(3)	-0.0017(7)	-0.0040(4)	0.0005(5)
Nb5	0.0049(4)	0.0081(4)	0.0097(4)	0.0003(8)	-0.0023(5)	-0.0008(6)
Nb6	0.0067(4)	0.0075(4)	0.0095(4)	-0.0022(8)	-0.0021(5)	-0.0049(6)
Nb7	0.0049	0.0081	0.0097	0.0003	-0.0023	-0.0008
Nb8	0.0067	0.0075	0.0095	-0.0022	-0.0021	-0.0049
Nb9	0.0055	0.0075	0.0084	-0.0017	-0.0040	0.0005
Nb10	0.0055	0.0072	0.0080	0.0015	-0.0033	0.0003
Nb11	0.0059	0.0090	0.0077	0.0002	-0.0025	-0.0028
Nb12	0.0027	0.0075	0.0077	-0.0004	-0.0039	-0.0005
Ca1	0.0067(5)	0.0083(6)	0.0101(5)	-0.0004(11)	-0.0006(5)	0.0024(10)
Ca2	0.0088(6)	0.0092(6)	0.0258(6)	-0.0051(14)	0.0031(6)	0.0036(10)
Ca3	0.0061(5)	0.0102(6)	0.0092(5)	-0.0002(13)	0.0005(6)	-0.0083(9)
Ca4	0.0126(6)	0.0192(7)	0.0222(6)	-0.0094(15)	0.0000(7)	-0.0154(11)
Ca5	0.0099(6)	0.0129(6)	0.0099(5)	0.0015(14)	-0.0011(6)	0.0073(10)
Ca6	0.0146(7)	0.0146(7)	0.0178(5)	-0.0073(15)	0.0026(7)	-0.0069(11)
Ca7	0.0146	0.0146	0.0178	-0.0073	0.0026	-0.0069
Ca8	0.0099	0.0129	0.0099	0.0015	-0.0011	0.0073
Ca9	0.0126	0.0192	0.0222	-0.0094	0.0000	-0.0154
Ca10	0.0061	0.0102	0.0092	-0.0002	0.0005	-0.0083
Ca11	0.0088	0.0092	0.0258	-0.0051	0.0031	0.0036
Ca12	0.0067	0.0083	0.0101	-0.0004	-0.0006	0.0024

[a]Each Nb site was constrained to be fully occupied by a mixture of Nb and Ti with equal thermal parameters. Parameters restricted by pseudo-inversion symmetry to other parameters are given without standard uncertainty.

Appendix F

Supplementary Materials for $\mathbf{Ca_5Nb_4TiO_{17}}$ ($n = 5$)

Table F.1: Fractional atomic coordinates and equivalent isotropic displacement parameters (Å^2) for $Ca_5Nb_4TiO_{17}$

Atom[a]	Occupancy[b]	x	y	z	U_{eq}[c]
Ca1	1	0.2534(1)	0.5059(2)	0.00569(4)	0.0089(4)
Ca2	1	0.2982(1)	0.9971(2)	0.09399(4)	0.0073(4)
Ca3	1	0.7918(1)	0.0058(3)	0.08151(5)	0.0143(4)
Ca4	1	0.3615(1)	0.5137(3)	0.20841(5)	0.0157(4)
Ca5	1	0.1372(1)	0.0818(2)	0.27823(4)	0.0086(4)
Nb1	0.577(10)	1/2	0	0	0.0029(3)
Nb2	0.535(10)	0	0	0	0.0028(3)
Nb3	0.811(8)	0.54456(8)	0.5019(1)	0.09119(1)	0.0035(2)
Nb4	0.791(8)	0.04677(8)	0.5033(1)	0.09052(1)	0.0037(2)
Nb5	0.939(8)	0.08661(7)	0.0221(1)	0.17691(1)	0.0039(1)
Nb6	0.959(8)	0.59443(7)	0.0253(1)	0.17792(1)	0.0041(1)
O1	1	0.5546(5)	0.2913(8)	0.0346(1)	0.007(1)
O2	1	0.9796(5)	0.2896(8)	0.0347(1)	0.006(1)
O3	1	0.4835(5)	0.7932(8)	0.0499(1)	0.008(1)
O4	1	0.0678(5)	0.7924(8)	0.0496(1)	0.007(1)
O5	1	0.0787(5)	0.2919(8)	0.2105(1)	0.008(1)
O6	1	0.6347(5)	0.3139(8)	0.2035(1)	0.009(1)
O7	1	0.1383(5)	0.8011(8)	0.2190(1)	0.009(1)
O8	1	0.5912(6)	0.8205(8)	0.2234(1)	0.008(1)
O9	1	0.0326(5)	0.2001(8)	0.1188(1)	0.007(1)
O10	1	0.5861(5)	0.1939(8)	0.1176(1)	0.005(1)
O11	1	0.3344(5)	0.0909(8)	0.1682(1)	0.008(1)
O12	1	0.1650(5)	0.4254(8)	0.3314(1)	0.008(1)
O13	1	0.1202(5)	0.7114(8)	0.1340(1)	0.008(1)
O14	1	0.5144(5)	0.7070(8)	0.1353(1)	0.009(1)
O15	1	0.7919(6)	0.5747(8)	0.0861(1)	0.009(1)
O16	1	0.2892(5)	0.4230(7)	0.0787(1)	0.004(1)
O17	1	0.7523(5)	0.9219(9)	0.0041(1)	0.006(1)

[a]Each Nb site was constrained to be fully occupied by a mixture of Nb and Ti with equal thermal parameters.

[b]Nb & Ti occupancies for each site sum up to 1.

[c]$U_{eq} = (1/3)\sum_i \sum_j U^{ij} a^i a^j \mathbf{a}_i \cdot \mathbf{a}_j$

Appendix G

Supplementary Materials for the Superspace Refinements

Table G.1: Atomic positions and displacement modulation parameters of $Ca_5Nb_4TiO_{17}$ ($n = 5$). For each crystallographically independent atom in the superspace approach are given the basic structure coordinates (A^0) as well as up to five modulation parameters: A^1, A^2, and A^3 refer to the parameters for sine functions, while B^1 and B^2 refer to the parameters for cosine functions.

Modulation functions for Nb are defined as: $u(\bar{x}_4) = A^1 \sin(2\pi\bar{x}_4) + A^2 \sin(12\pi\bar{x}_4) + A^3 \sin(24\pi\bar{x}_4)$. For Ca and O orthogonalized functions have been used as defined in Table G.3.

Atom	A^0	A^1	B^1	A^2	B^2	A^3
Nb1						
x	1/4	-0.0036(1)	0	0.00244(8)	0	0
y	0	0.1229(1)	0	0.0112(1)	0	0
z	1/2	-0.0440(2)	0	0.0147(1)	0	0
Nb2						
x	3/4	0.0110(1)	0	-0.00387(8)	0	0
y	0	0.1348(1)	0	0.0122(1)	0	0
z	1/2	-0.0506(2)	0	0.0150(1)	0	0
Ca1						
x	-0.00010(9)	0.0009(1)	-0.0002(1)	0	0	0
y	-0.0345(1)	0.0223(1)	0.0021(1)	0	0	0
z	0.0049(1)	0.0011(1)	0.0009(2)	0	0	0
Ca2						
x	0.0018(1)	0	0	0	0	0
y	0.3304(2)	0	0	0	0	0
z	-0.0817(2)	0	0	0	0	0
Ca3						
x	-0.0072(1)	0	0	0	0	0
y	-0.2503(2)	0	0	0	0	0
z	0.0136(2)	0	0	0	0	0
O1						
x	-0.0000(2)	0.0003(2)	-0.0001(2)	-0.0005(3)	0.0003(3)	0
y	0.0137(3)	0.0051(3)	0.0115(3)	-0.0077(4)	-0.0027(5)	0
z	0.5793(4)	-0.0052(3)	-0.0037(4)	0.0019(4)	0.0025(5)	0
O2						
x	0.2145(2)	0.0029(2)	-0.0069(2)	0.0084(2)	0.0028(2)	-0.0045(3)
y	0.2117(3)	0.0229(3)	-0.0099(3)	-0.0103(4)	0.0050(4)	0.0032(5)
z	0.2059(3)	0.0022(3)	0.0021(3)	-0.0059(4)	0.0008(4)	0.0047(6)
O3						
x	0.7864(2)	0.0000(2)	0.0037(2)	-0.0107(3)	-0.0019(2)	0.0055(3)
y	0.1989(3)	0.0188(3)	0.0037(3)	-0.0076(4)	0.0018(4)	0.0029(5)
z	0.1976(3)	0.0000(3)	0.0093(4)	-0.0057(4)	0.0000(4)	0.0042(6)

Table G.2: Anisotropic atomic displacement parameters (ADPs) and their modulation parameters for $Ca_5Nb_4TiO_{17}$ ($n = 5$). Values of U_{ij} are given in Å^2. ADPs in the basic structure are denoted by A^0. A^1 refers to the parameter for sine functions, while B^1 refers to the parameters for cosine functions. Modulation functions for Ca1 are defined in Table G.3.

Atom	U_{11}	U_{22}	U_{33}	U_{12}	U_{13}	U_{23}
Nb1						
A^0	0.0031(2)	0.0041(2)	0.0041(2)	0.0001(2)	-0.0001(1)	0.0005(1)
Nb2						
A^0	0.0031(2)	0.0043(2)	0.0041(2)	-0.0004(2)	-0.0000(1)	0.0002(1)
Ca1						
A^0	0.0094(4)	0.0122(4)	0.0105(4)	0.0000(3)	-0.0003(3)	-0.0032(3)
A^1	0.0024(3)	0.0042(4)	0.0031(3)	-0.0000(3)	-0.0002(3)	-0.0014(3)
B^1	-0.0000(3)	-0.0022(4)	-0.0011(4)	-0.0003(3)	0.0003(4)	0.0013(4)
Ca2						
A^0	0.0057(5)	0.0117(6)	0.0088(6)	-0.0006(4)	-0.0002(5)	-0.0013(5)
Ca3						
A^0	0.0080(6)	0.0280(8)	0.0114(6)	0.0003(5)	-0.0002(5)	-0.0044(6)
O1						
A^0	0.0045(9)	0.009(1)	0.006(1)	-0.0000(8)	0.0003(7)	0.0009(7)
O2						
A^0	0.0077(9)	0.0071(8)	0.0070(8)	-0.0005(6)	-0.0010(6)	0.0020(7)
O3						
A^0	0.0088(9)	0.0062(9)	0.0080(8)	0.0001(6)	0.0008(7)	0.0019(7)

Table G.3: Definitions of orthogonalized functions for $Ca_5Nb_4TiO_{17}$ ($n = 5$)

The modulation functions for the atomic positions and atomic displacements are obtained as the sum of the orthogonalized functions multiplied by the corresponding modulation parameters.

Atom	Modulation Parameter	Orthogonalized Function
Ca1	A^1	4.479sin $(2\pi\bar{x}_4)$
	B^1	-2.069 + 3.249cos $(8\pi\bar{x}_4)$
O1	A^1	2.762sin $(2\pi\bar{x}_4)$
	B^1	-1.084 + 2.303cos $(6\pi\bar{x}_4)$
	A^2	-6.653sin $(2\pi\bar{x}_4)$ + 3.416sin $(8\pi\bar{x}_4)$
	B^2	2.945 - 5.002cos $(6\pi\bar{x}_4)$ + 3.281cos $(12\pi\bar{x}_4)$
O2/O3	A^1	2.346sin $(2\pi\bar{x}_4)$
	B^1	-2.069 + 3.249cos $(4\pi\bar{x}_4)$
	A^2	-3.091sin $(2\pi\bar{x}_4)$ + 2.339sin $(8\pi\bar{x}_4)$
	B^2	4.661 - 6.458cos $(4\pi\bar{x}_4)$ + 3.052cos $(10\pi\bar{x}_4)$
	A^3	6.304sin $(2\pi\bar{x}_4)$ - 3.604sin $(8\pi\bar{x}_4)$ + 2.641sin $(14\pi\bar{x}_4)$

Table G.4: Atomic positions and displacement modulation parameters of $Ca_6(Nb,Ti)_6O_{20}$ ($n = 6$). For each crystallographically independent atom in the superspace approach are given the basic structure coordinates (A^0) as well as up to five modulation parameters: A^1, A^2, and A^3 refer to the parameters for sine functions, while B^1 and B^2 refer to the parameters for cosine functions.

Modulation functions for Nb are defined as: $u(\bar{x}_4) = A^1 \sin(2\pi\bar{x}_4) + A^2 \sin(12\pi\bar{x}_4) + A^3 \sin(24\pi\bar{x}_4)$. For Ca and O orthogonalized functions have been used as defined in Table G.6.

Atom	A^0	A^1	B^1	A^2	B^2	A^3
Nb1						
x	1/4	-0.0015(2)	0	0.0014(1)	0	-0.0018(1)
y	0	0.1249(1)	0	0.0039(1)	0	-0.00666(9)
z	1/2	-0.0375(2)	0	0.0115(1)	0	-0.0088(2)
Nb2						
x	3/4	0.0098(2)	0	-0.0032(1)	0	0.0018(1)
y	0	0.1360(1)	0	0.0046(1)	0	-0.00663(9)
z	1/2	-0.0433(2)	0	0.0125(1)	0	-0.0090(2)
Ca1						
x	-0.00001(8)	0.0007(1)	0.0000(1)	0	0	0
y	-0.0344(1)	0.0241(1)	0.0001(1)	0	0	0
z	0.0045(1)	-0.0008(1)	0.0019(1)	0	0	0
Ca2						
x	0.0016(2)	0	0	0	0	0
y	0.3319(2)	0	0	0	0	0
z	-0.0872(3)	0	0	0	0	0
Ca3						
x	-0.0084(2)	0	0	0	0	0
y	-0.2495(2)	0	0	0	0	0
z	0.0171(3)	0	0	0	0	0
O1						
x	-0.0001(2)	-0.0005(3)	0.0010(2)	-0.0019(5)	-0.0003(3)	-0.0026(6)
y	0.0147(2)	0.0087(4)	0.0097(3)	-0.0080(5)	-0.0030(4)	0.0065(7)
z	0.5798(4)	-0.0053(5)	-0.0027(4)	0.0039(7)	0.0024(4)	0.0006(9)
O2						
x	0.2139(2)	0.0029(2)	-0.0054(2)	0.0052(2)	0.0030(2)	-0.0039(3)
y	0.2112(3)	0.0228(3)	-0.0074(3)	-0.0099(3)	0.0059(3)	0.0057(4)
z	0.2056(3)	0.0019(3)	0.0036(3)	-0.0050(4)	-0.0020(4)	0.0047(4)
O3						
x	0.7869(2)	-0.0006(2)	0.0023(2)	-0.0105(3)	-0.0015(2)	0.0084(3)
y	0.1981(3)	0.0183(3)	0.0058(3)	-0.0072(4)	0.0026(4)	0.0039(5)
z	0.1964(3)	-0.0022(3)	0.0133(3)	-0.0023(4)	-0.0049(4)	0.0049(4)

Table G.5: Anisotropic atomic displacement parameters (ADPs) and their modulation parameters for $Ca_6(Nb,Ti)_6O_{20}$ ($n = 6$). Values of U_{ij} are given in Å^2. ADPs in the basic structure are denoted by A^0. A^1 and A^2 refer to the parameters for sine functions, while B^1 refers to the parameters for cosine functions. Modulation functions for Ca1 are defined in Table G.6.

Atom	U_{11}	U_{22}	U_{33}	U_{12}	U_{13}	U_{23}
Nb1						
A^0	0.0057(2)	0.0080(2)	0.0085(2)	-0.0037(3)	-0.0001(2)	0.0000(1)
Nb2						
A^0	0.0052(2)	0.0080(2)	0.0079(2)	-0.0041(3)	-0.0005(2)	0.0004(1)
Ca1						
A^0	0.0106(3)	0.0144(3)	0.0133(4)	-0.0004(3)	0.0002(4)	-0.0027(2)
A^1	0.0034(3)	0.0035(3)	0.0035(3)	-0.0008(4)	-0.0001(4)	-0.0015(4)
B^1	0.0012(3)	-0.0001(3)	-0.0010(4)	-0.0003(3)	-0.0000(6)	0.0007(3)
A^2	0.0004(4)	0.0017(4)	-0.0020(4)	0.0008(4)	-0.0009(6)	0.0001(6)
Ca2						
A^0	0.0067(5)	0.0084(5)	0.0059(5)	-0.0021(6)	0.0003(7)	0.0016(4)
Ca3						
A^0	0.0077(6)	0.0250(6)	0.0073(6)	0.0026(5)	-0.0022(7)	-0.0001(6)
O1						
A^0	0.0040(8)	0.0116(8)	0.0121(9)	-0.0020(8)	-0.0000(7)	0.0002(6)
O2						
A^0	0.0040(9)	0.0094(7)	0.0105(7)	-0.0019(6)	-0.0024(6)	0.0001(6)
O3						
A^0	0.009(1)	0.0098(8)	0.0101(8)	-0.0010(6)	-0.0002(7)	0.0026(6)

Table G.6: Definitions of orthogonalized functions for $Ca_6(Nb,Ti)_6O_{20}$ ($n = 6$).

The modulation functions for the atomic positions and atomic displacements are obtained as the sum of the orthogonalized functions multiplied by the corresponding modulation parameters.

Atom	Modulation Parameter	Orthogonalized Function
Ca1	A^1	3.938sin $(2\pi\bar{x}_4)$
	B^1	-1.428 + 2.629cos $(8\pi\bar{x}_4)$
	A^2	-8.459sin $(2\pi\bar{x}_4)$+ 3.131sin $(12\pi\bar{x}_4)$
O1	A^1	2.692sin $(2\pi\bar{x}_4)$
	B^1	-0.987 + 2.213cos $(6\pi\bar{x}_4)$
	A^2	-5.958sin $(2\pi\bar{x}_4)$ + 3.209sin $(8\pi\bar{x}_4)$
	B^2	2.523 - 4.336cos $(6\pi\bar{x}_4)$ + 3.042cos $(12\pi\bar{x}_4)$
	A^3	17.821sin $(2\pi\bar{x}_4)$ - 9.192sin $(8\pi\bar{x}_4)$ + 4.309sin $(14\pi\bar{x}_4)$
O2/O3	A^1	2.346sin $(2\pi\bar{x}_4)$
	B^1	-2.069 + 3.249cos $(4\pi\bar{x}_4)$
	A^2	-3.091sin $(2\pi\bar{x}_4)$ + 2.339sin $(8\pi\bar{x}_4)$
	B^2	4.661 - 6.458cos $(4\pi\bar{x}_4)$ + 3.052cos $(10\pi\bar{x}_4)$
	A^3	6.304sin $(2\pi\bar{x}_4)$ - 3.604sin $(8\pi\bar{x}_4)$ + 2.641sin $(14\pi\bar{x}_4)$

Table G.7: Number of refined parameters in various refinements of $Ca_5Nb_4TiO_{17}$ ($n = 5$) and $Ca_6(Nb,Ti)_6O_{20}$ ($n = 6$).

	$n = 5$		$n = 6$	
Parameter	Supercell	Superspace	Supercell	Superspace
Occupation	6	6	6	6
Position	78	78	191	87
ADP	168	60	92	66
Scale factor	1	1	1	1
Twin Vol.	1	1	1	1
Extinction	–	–	1	1
Total	254	146	292	162

Table G.8: Reflections of $Ca_6(Nb,Ti)_6O_{20}$ ($n = 6$) rejected by the superspace centerings ($\frac{1}{4}$ $\frac{1}{2}$ 0 $\frac{3}{4}$) and ($\frac{3}{4}$ $\frac{1}{2}$ 0 $\frac{1}{4}$). Reflection condition is $(HKLM) : H + 2K - M = 4i$ (i = integer). Notice $I < 11\sigma$ for all reflections of this class.

	Supercell	Superspace
Independent reflections rejected		
All	–	1937
Observed		
$I > 3\sigma$	–	394
$I > 5\sigma$	–	105
$I > 7\sigma$	–	35

Bibliography

Abrahams, S. C., Schmalle, H. W., Williams, T., Reller, A., Lichtenberg, F., Widmer, D., Berdnorz, J., Spreiter, R., Bosshard, C. and Günter, P. (1998). Centrosymmetric or noncentrosymmetric? case study, generalization and structural redetermination of $Sr_5Nb_5O_{17}$, *Acta Crystallographica B* **54**: 399–416.

Becker, P. and Coppens, P. (1974). Extinction within limit of validity of darwin transfer equations. 1. general formalisms for primary and secondary extinction and their application to spherical crystals, 2. refinement of extinction in spherical crystal of SrF_2 and LiF, *Acta Crystallographica A* **30**: 129–153.

Bobnar, V., Lunkenheimer, P., Hemberger, J., Loidl, A., Lichtenberg, F. and Mannhart, J. (2002). Dielectric properties and charge transport in the (Sr,La)$NbO_{3.5-x}$ system, *Physical Review B* **65**: 155115.

Boullay, P., Trolliard, G., Mercurio, D., Perez-Mato, J. and Elcoro, L. (2002). Towards a unified approach to the crystal chemistry of aurivillius-type compounds. II. $Bi_7Tl_4NbO_{21}$, a case study, *Journal of Solid Stae Chemistry* **164**: 261–271.

Brandenburg, K. (2005). *DIAMOND. Version 3.0c.*, Crystal Impact GbR, Bonn, Germany.

Brese, N. and O'Keeffe, M. (1991). Bond-valence parameters for solids, *Acta Crystallographica B* **47**: 192–197.

Bruker (1998a). *ASTRO for Windows NT Software Reference Manual, v.5.0.07*, Bruker AXS, Madison,USA.

Bruker (1998b). *SMART for Windows NT and IRIX Software Reference Manual v.5.0*, Bruker AXS, Madison,USA.

Bruker (2000). *SAINT. Program for the Integration of Intensities from Diffraction Images*, Bruker AXS GmbH, Karlsruhe, Germany.

Burla, M., Camalli, M., Carrozzini, B., Cascarano, G., Giacovazzo, C., G., P. and Spagna, R. (2003). SIR2002: the program, *Jornal of Applied Crystallography* **36**: 1103.

Carpy, A., Amestoy, P. and Galy, J. (1972). Study on calcium pyroniobate $Ca_2Nb_2O_7$, *Comptes Rendus Hebdomadaires des Seances del Academie des Sciences Serie C* **275**(15): 833.

Clegg, W., Blake, A., Gould, R. and Main, P. (2001). *Crystal Structure Analysis: Principles and Practice, IUCr Texts on Crystallography - 6*, Oxford University Press, Inc., New York, USA.

Daniels, P., Tamazyan, R., Kuntscher, C. A., Dressel, M., Lichtenberg, F. and Van Smaalen, S. (2002). The incommensurate modulation of the structure of $Sr_2Nb_2O_7$, *Acta Crystallographica B* **58**: 970–976.

Daniels, P., Van Smaalen, S. and Lichtenberg, F. (2003). Perovskite-related $LaTiO_{3.41}$, *Acta Crystallographica C* **59**: i15–i17.

Dariet, J., Elcoro, L., El Abed, A., Gaudin, E. and Perez-Mato, J. (2002). Crystal structure of $Ba_{12}Co_{11}O_{33}$. reinvestigation using the superspace group approach of orthorhombic oxides $A_{1+x}(A'B_{1-x})O_3$ based on (A_8O_{24}) and $(A_8A'_2O_{18})$, *Chemistry of Materials* **14**: 3349–3363.

de Wolff, P. (1974). The pseudo-symmetry of modulated crystal structures, *Acta Crystallographica A* **30**: 777–785.

Del Rio, M. and Dejus, R. (1998). *XOP 2.0 Software Online Reference Manual*, 2nd edn, European Synchrotron Radiation Facility (ESRF), Grenoble, France.

Drews, A., Wong-Ng, W., Roth, R. and Vanderah, T. (1996). Preparation and crystal structure of $Sr_5TiNb_4O_{17}$, *Materials Research Bulletin* **31**: 153–162.

Elcoro, L., Perez-Mato, J. and Withers, R. (2000). Intergrowth polytypoids as modulated structures: the example of the cation deficient oxides $LaTi_{1-x}O_3$, *Zeitschrift für Kristallographie* **215**: 727–739.

Elcoro, L., Perez-Mato, J. and Withers, R. (2001). Intergrowth polytypoids as modulated structures: a superspace description of the $Sr_n(Nb,Ti)_nO_{3n+2}$, *Acta Crystallographica B* **57**: 471–484.

Elcoro, L., Zuniga, F. J. and Perez-Mato, J. M. (2004). Superspace description of $NaCa_4Nb_5O_{17}$ (a perovskite-related compound of the type $A_nB_nO_{3n+2}$) as a modulated layered structure, *Acta Crystallographica B* **60**: 21–31.

Enraf-Nonius (1989). *CAD-4 Software v.5.0 Reference Manual*, Enraf-Nonius, Delft, The Netherlands.

Galy, J. and Carpy, A. (1974). Defects and diffusion paths in perovskite-like structures ABO_{3+x}, *Philosophical Magazine* **29**(5): 1207–1211.

Giacovazzo, C., Monaco, H., Artioli, G., Viterbo, D., Ferraris, G., Gilli, G., Zanotti, G. and Catti, M. (2002). *Fundamentals of Crystallography, IUCr Texts on Crystallography - 7*, 2nd edn, Oxford University Press, Inc., New York, USA.

Glazer, A. (1975). Simple ways of determining perovskite structures, *Acta Crystallographica A* **31**: 756–762.

Guevarra, J., van Smaalen, S., Daniels, P., Rotiroti, N. and Lichtenberg, F. (2005a). Perovskite-related $Ca(Nb,Ti)O_{3.33}$, *Zeitschrift für Kristallographie* **220**: 19–24.

Guevarra, J., van Smaalen, S. and Lichtenberg, F. (2006). Crystal structure of perovskite-related $Ca_5Nb_4TiO_{17}$. *Submitted to Acta Crystallographica C*.

Guevarra, J., van Smaalen, S., Rotiroti, N., Paulmann, C. and Lichtenberg, F. (2005b). Crystal structure of $Ca_5Nb_5O_{17}$, *Journal of Solid State Chemistry* **178**: 2934–2941.

Janner, A. and Janseen, T. (1977). Symmetry of periodically distorted crystals, *Phsical Review B* **15**(2): 643–658.

Kinase, W., Nanamatsu, S., N., I., Ishihara, N., Hasegawa, K. and Yano, K. (1981). On ferroelectricity of $Sr_2Nb_2O_7$ and other $A_2B_2O_7$-type layer-structure crystals, *Ferroelectrics* **38**: 849–851.

Klein, C. (2004). *The Mar345 dtb User's Guide - online manual*, Marresearch GmbH, Norderstedt, Germany.

Kuntscher, C. A., Schuppler, S., Haas, P., Gorshunov, B., Dressel, M., Grioni, M. and Lichtenberg, F. (2004). Electronic and vibrational properties of low-dimensional perovskites $Sr_{1-y}La_yNbO_{3.5-x}$, *Physical Review B* **70**: 245123.

Kuntscher, C. A., Schuppler, S., Haas, P., Gorshunov, B., Dressel, M., Grioni, M., Lichtenberg, F., Herrnberger, A., Mayr, F. and Mannhart, J. (2002). Extremely small energy gap in the quasi-one-dimensional conducting chain compound $SrNbO_{3.41}$, *Physical Review Letters* **89**(23): 236403.

Kuntscher, C., Gerhold, S., Nucker, N., Cummins, T., Lu, D., Schuppler, S., Gopinath, C., Lichtenberg, F., Mannhart, J. and Bohnen, K. (2000). Electronic structure of layered perovskite-related $Sr_{1-y}La_yNbO_{3.5-x}$, *Physical Review B* **61**(3): 1876–1883.

Kunz, M. and Brown, I. (1995). Out-of-center distortions around octahedrally coordinated d^0 transition metals, *Journal of Solid State Chemistry* **115**: 395–406.

Levin, I. and Bendersky, L. (1999). Symmetry classification of the layered perovskite-derived $A_nB_nX_{3n+2}$ structures, *Acta Crystallographica B* **55**: 853–866.

Levin, I., Bendersky, L. and Vanderah, T. A. (2000). A structural study of the layered perovskite-derived $Sr_n(Ti,Nb)_nO_{3n+2}$ compounds by transmission electron microscopy, *Philosophical Magazine A* **80**: 411–445.

Lichtenberg, F., Herrnberger, A., Wiedenmann, K. and Mannhart, J. (2001). Synthesis of perovskite-related layered $A_nB_nO_{3n+2} = ABO_x$ type niobates and ti-

tanates and study of their structural, electric and magnetic properties, *Progress of Solid State Chemistry* **29**: 1–70.

Oxford Diffraction (2004). *User Manual (v.1.5): Xcalibur series - Single-crystal diffractometers*, Oxford Diffraction Limited, Oxford, United Kingdom.

Microcal Software, I. (1997). *Microcal Origin Software Reference Manual v.5.0*, Northampton, MA, USA.

Nanamatsu, S., Kimura, D., Mashushita, S. and Yamada, N. (1974). New ferroelectric - $La_2Ti_2O_7$, *Ferrolelectrics* **8**: 511–515.

Nanamatsu, S. and Kimura, M. (1974). Ferroelectric properties of $Ca_2Nb_2O_7$ single -crystal, *Journal of the Physical Society of Japan* **36**: 1495.

Nanot, M., Queyroux, F. and Gilles, J. (1979). Etude cristallographique des termes $n = 4$,5, 5 et 6 des séries $(La,Ca)_nTi_nO_{3n+2}$, $(Nd,Ca)_nTi_nO_{3n+2}$ et $Ca_n(Ti,Nb)_nO_{3n+2}$, *Journal of Solid State Chemistry* **28**: 137–147.

Nanot, M., Queyroux, F. and Gilles, J. (1981). $A_nB_nO_{3n+2}$ phases of the systems $La_2Ti_2O_7$-$CaTiO_3$, $Nd_2Ti_2O_7$-$CaTiO_3$, and $Ca_2Nb_2O_7$-$CaTiO_3$ -new crystallographic characteristics and an interpretation of the twinning revealed by the electron microscope, *Journal of Solid State Chemistry* **38**: 74–81.

Nanot, M., Queyroux, F. and Gilles, J. (1983). Crystallochemistry of new ferroelectric compounds, *in* R. Metselaar, H. Heijligers and J. Schonman (eds), *Studies in Inorganic Chemistry*, Vol. 3, Elsevier Scientific Publishing Company, Amsterdam, The Netherlands, pp. 623–626.

Nanot, M., Queyroux, F., Gilles, J. and Capponi, J. (1986). Study of the incommensurability of $La_4Ca_2Ti_6O_{20}$ and $(Nd_4Ca_2)Ti_6O_{20}$, members n=6 of the $A_nB_nO_{3n+2}$ family - interpretation of the lattice modulation using a 4-dimensional space, *Journal of Solid State Chemistry* **61**: 315–323.

Nanot, M., Queyroux, F., Gilles, J., Carpy, A. and Galy, J. (1974). Multiple phases in systems $Ca_2Nb_2O_7$-$NaNbO_3$ and $La_2Ti_2O_7$-$CaTiO_3$-homologons series into formula $A_nB_nO_{3n+2}$, *Journal of Solid State Chemistry* **11**: 272–284.

Paulmann, C. (2002). *SAPRO for Windows NT Software, v.1.5.50*, University of Hamburg, Hamburg, Germany.

Perez-Mato, J., Zakhour-Nakhl, M., Weill, F. and Darriet, J. (1999). Structure of composites $A_{1+x}(A'B_{1-x})O_3$ related to 2H hexagonal perovskite: relation between composition and modulation, *Journal of Materials Chemistry* **9**: 2795–2808.

Petricek, V., Dusek, M. and Palatinus, L. (2000). *The Crystallographic Computing System JANA2000*, Institute of Physics, Praha, Czech Republic.

Petricek, V., van der Lee, A. and Evain, M. (1995). On the use of crenel functions for occupationally modulated structures, *Acta Crystallographica A* **51**: 529–535.

Schönleber, A. (2002). *The Superspace Approach Applied to Modulated Crystals*, PhD thesis, University of Lausanne, Lausanne, Switzerland.

Shannon, R. (1976). Revised effective ionic radii and systematic studies of interatomic distances in halides and chalcogenides, *Acta Crystallographica A* **32**: 751–767.

Sheldrick, G. M. (2002). *SADABS v.2.03, Bruker area detector absorption and other corrections*, University of Göttingen, Göttingen, Germany.

STOE and Cie (1999). *X-SHAPE: Crystal Optimization for Numerical Absorption Correction*, Darmstadt, Germany.

Stout, G. and Jensen, L. (1989). *X-ray Structure Determination: A Practical Guide*, 2nd edn, John Wiley & Sons, Inc., New York, USA.

van Smaalen, S. (2004). An elementary introduction to superspace crystallography, *Zeitschrift für Kristallographie* **219**: 681–691.

Weber, J., Kegler, C., Büttgen, N., Krug von Nidda, H., Loidl, A. and Lichtenberg, F. (2001). NMR, EPR, and Bulk susceptibility measurements of one-dimensional $SrNbO_{3.41}$, *Physical Review B* **64**: 235414.

Zakhour-Nakhl, M., Weill, F., Darriet, J. and Perez-Mato, J. (2000). A new exmple of a composite composition flexible phase structure of $Ba_{1+x}A'B_{1-x}O_3$ ($x = 0.2124$, $A' = Ni$, $B = 0.51Ni + 0.49Pt$), *International Journal of Inorganic Materials* **2**: 71–79.

Zuniga, F. and Darriet, J. (2003). $NaCa_4Nb_5O_{17}$: a layered perovskite $A_nB_nO_{3n+2}$ compound, *Acta Crystallographica C* **59**: i18–i20.

List of Figures

1.1 Sketch of the idealized, non-distorted crystal structures of the $n = 2, 3, 4$ and 4.33 members of the perovskite-related layers $A_nB_nO_{3n+2}$ projected along the **a**-axis. 8

2.1 Sketch of a mounted single crystal 16

2.2 Nonius Kappa MACH3 single-crystal diffractometer at the Laboratory of Crystallography, Bayreuth, Germany 17

2.3 Omega scans onf the reflection (2 0 0) of $Ca_5Nb_4TiO_{17}$ ($n = 5$) for two different ψ-values 19

2.4 Huber Kappa-diffractometer at beamline F1 of Hasylab in DESY, Hamburg, Germany 21

2.5 X-ray diffraction data on $Ca_5Nb_5O_{17}$ ($n = 5$) recorded using synchrotron radiation ($\lambda = 0.7100(2)$ Å) with a SMART CCD detector . 22

2.6 Mar345 IP desktop beam line single-crystal diffractometer at the Laboratory of Bayreuth, Bayreuth, Germany 25

2.7 X-ray diffraction data on $Ca_5Nb_4TiO_{17}$ ($n = 5$) recorded using Mo-Kα radiation with MAR345 Image Plate Detector 26

3.1 Projection of the idealized, non-distorted crystal structures of the $n = 5$, 6 and ∞ members $A_nB_nO_{3n+2}$. 28

3.2 Schematic projections of non-distorted $A_5B_5O_{17}$ 29

3.3 Embedding of the diffraction pattern along the reciprocal lattice line $\mathbf{R}^*$ of a modulated crystal in a (1+1)D superspace. 32

3.4 Atomic structure in direct superspace of an incommensurately modulated crystal 34

4.1 Vector plot of the intensity and rocking curve of the reflection (4 0 8) of $Ca(Nb,Ti)O_{3.33}$ 38
4.2 Predicted positions of the reflections of $Ca_5Nb_5O_{17}$ overlayed on a measured diffraction frame. 41
4.3 Spot profile of $Ca_5Nb_5O_{17}$ averaged over nine detector regions shown as nine 9×9 XY-sections. 45
4.4 Plots of χ^2 versus resolution and intensity of $Ca_5Nb_5O_{17}$ using SADABS 48
4.5 Predicted positions of the reflections of $Ca_5Nb_4TiO_{17}$ overlayed on a measured diffraction frame. 50
4.6 Crystal shape of $Ca_5Nb_4TiO_{17}$ refined using STOE X-SHAPE 53

5.1 Sample rocking curve for the 2 0 0 reflection of the compound $Ca_5Nb_5O_{17}$ 58
5.2 Orientation of the two twin domains in reciprocal space in the case of pseudo-merohedral twinning of the crystal in $Ca_5Nb_5O_{17}$ ($n = 5$) . 62
5.3 Projections of the structure of $Ca_5Nb_5O_{17}$ ($n = 5$) 64
5.4 Tilting of NbO_6 octahedra in $Ca_5Nb_5O_{17}$ 65
5.5 Different coordination environments of Ca atoms in $Ca_5Nb_5O_{17}$ . . . 66
5.6 Nb–O bond distances at the different Nb sites in $Ca_5Nb_5O_{17}$ 67
5.7 Distortion of NbO_6 octahedra at the different Nb sites in $Ca_5Nb_5O_{17}$ 68
5.8 Valences of Nb at the different sites in $Ca_5Nb_5O_{17}$ 70
5.9 Coordination of Ca2 in $Ca_5Nb_5O_{17}$ viewed along $\mathbf{c}^*$, and Sr3 in $Sr_5Nb_5O_{17}$ viewed along $\mathbf{a}^*$ 71

6.1 Projections of the structure of $Ca(Nb,Ti)O_{3.33}$ ($n = 6$). 75
6.2 Orientation of the two twin domains in reciprocal space in the case of pseudo-merohedral twinning of the crystal in $Ca(Nb,Ti)O_{3.33}$ ($n = 6$) 78
6.3 Different coordination environments of Ca atoms in $Ca(Nb,Ti)O_{3.33}$. 80
6.4 Nb–O bond distances at the different (Nb,Ti) sites in $Ca(Nb,Ti)O_{3.33}$ 81
6.5 Distortion of $(Nb,Ti)O_6$ octahedra at the different (Nb,Ti) sites in $Ca(Nb,Ti)O_{3.33}$ 82

6.6 Atomic site occupancy of at the different (Nb,Ti) sites in $Ca(Nb,Ti)O_{3.33}$ 83
6.7 Valences of Nb and Ti at the different (Nb,Ti) sites in $Ca(Nb,Ti)O_{3.33}$ 84

7.1 Projections of the crystal structure of $Ca_5Nb_4TiO_{17}$ ($n = 5$) 88
7.2 Nb–O bond distances at the different (Nb,Ti) sites in $Ca_5Nb_4TiO_{17}$. 89
7.3 Atomic site occupancy of Ti at the different (Nb,Ti) sites in $Ca_5Nb_4TiO_{17}$ 90
7.4 Valences of Nb and Ti at the different (Nb,Ti) sites in $Ca_5Nb_4TiO_{17}$. 92

8.1 Projections of the crystal structures along **c** of $Ca_5Nb_4TiO_{17}$ ($n = 5$) and $Ca_6(Nb,Ti)_6O_{20}$ ($n = 6$) along the **c**- direction 96
8.2 Atomic domains in superspace for the $n = 5$ member of the general homologous series $A_nB_nO_{3n+2}$ compound series 98
8.3 Sub-domains comprising the atomic domains of Nb1 in $Ca_5Nb_4TiO_{17}$ ($n = 5$) and $Ca_6(Nb,Ti)_6O_{20}$ ($n = 6$) 105
8.4 Site occupancy factors of Ti at the different Ti subdomains 107
8.5 t-Plots of the displacement along y of Nb1 and Nb2 in $Ca_5Nb_4TiO_{17}$ ($n = 5$) and $Ca_6(Nb,Ti)_6O_{20}$ ($n = 6$). 108
8.6 t-Plots of the y components of the displacive modulation of the O atoms in $Ca_5Nb_4TiO_{17}$ ($n = 5$) and $Ca_6(Nb,Ti)_6O_{20}$ ($n = 6$). 109
8.7 Nb and Ti valences for the different (Nb,Ti) sites 110

List of Tables

5.1 Experimental details on $Ca_5Nb_5O_{17}$ ($n = 5$) 60
5.2 Fractional atomic coordinates and equivalent isotropic atomic displacement parameters of $Ca_5Nb_5O_{17}$ ($n = 5$) 63
5.3 Mean O–Nb–O bond angles in $Ca_5Nb_5O_{17}$ ($n = 5$) 69
5.4 Range of Nb–O bond distances and mean O–Nb–O bond angles in $Sr_5Nb_5O_{17}$ (n= 5) 69

6.1 Experimental details on $Ca(Nb_{0.76}Ti_{0.24})O_{3.33}$ ($n = 6$) 77

7.1 Experimental details on $Ca_5Nb_4TiO_{17}$ ($n = 5$) 91

8.1 Details of supercell refinements in the primitive and C-centered settings 101
8.2 Details of superspace refinements 103
8.3 Definition of occupational modulation functions (crenel functions) of $Ca_5Nb_4TiO_{17}$ and $Ca_6(Nb,Ti)_6O_{20}$ 104
8.4 Summary of partial R values of the supercell and the superspace refinements 106

E.1 Fractional atomic coordinates, occupancies, and U_{eq} of Nb and Ca atoms in $Ca(Nb,Ti)O_{3.33}$ 142
E.2 Fractional atomic coordinates, occupancies, and U_{eq} of O atoms in $Ca(Nb,Ti)O_{3.33}$ 143
E.3 Anisotropic displacement parameters (Å^2) of Nb/Ti and Ca atoms in $Ca(Nb,Ti)O_{3.33}$ 144

F.1 Fractional atomic coordinates, occupancies, and U_{eq} in $Ca_5Nb_4TiO_{17}$. 146

G.1 Positions and displacement modulation parameters of $Ca_5Nb_4TiO_{17}$ ($n = 5$) from superspace refinement 148
G.2 Anisotropic displacement parameters and their modulation parameters for $Ca_5Nb_4TiO_{17}$ ($n = 5$) from superspace refinement 149
G.3 Definitions of orthogonalized functions for $Ca_5Nb_4TiO_{17}$ ($n = 5$) used in superspace refinement. 150
G.4 Positions and displacement modulation parameters of $Ca_6(Nb,Ti)_6O_{20}$ ($n = 6$) from superspace refinement 151
G.5 Anisotropic displacement parameters and their modulation parameters for $Ca_6(Nb,Ti)_6O_{20}$ ($n = 6$) from superspace refinement 152
G.6 Definitions of orthogonalized functions for $Ca_6(Nb,Ti)_6O_{20}$ ($n = 6$) used in superspace refinement 153
G.7 Number of refined parameters in various refinements of $Ca_5Nb_4TiO_{17}$ ($n = 5$) and $Ca_6(Nb,Ti)_6O_{20}$ ($n = 6$) 154
G.8 Rejected reflections in $Ca_6(Nb,Ti)_6O_{20}$ ($n = 6$) 154

Acknowledgements

I would like to sincerely thank my PhD supervisor Prof. Dr. Sander van Smaalen who has given me the opportunity to work at the Laboratory of Crystallography in Bayreuth. I am grateful to him for supporting me in my studies and for the many scientific advices he has given from which I have greatly profitted. I am much indebted to him for my foundations in crystallography and my gained experience with X-ray diffraction. I would like to thank also my colleagues who have helped me in one way or another during my stay in the department. I would like to give my special thanks to: Nicola Rotiroti for his help in the experiments and for patiently discussing with me about crystallography, Dr. Andreas Schönleber for the many insightful discussions about superspace crystallography and for his numerous help including the translation of the German summary of the thesis, Dr. Peter Daniels for helping me with the X-ray diffraction experiments during my early days in the laboratory, Dr. Lukas Palatinus for his scientific advices on my project and on the administration of computers in the laboratory even after he has left, and Dipl. Ing. (FH) Franz Fischer for his help with technical and administrative problems concerning the computers in the laboratory. I would also like to thank Dr. Carsten Paulmann of Hasylab in DESY for his support during our experiments at beamline F1. The accomplishment of this thesis would not have been possible without the support of my family and friends. I would like to express my greatest thank to my loving wife, Anne, for her many sacrifices and invaluable support during my studies, and to my two lovely children, J.A. and Jules, for being my inspiration, comfort, and reward. I thank our parents for providing us moral and financial assistance during our stay in Germany. I am grateful also to the Filipino community in Bayreuth and in the nearby towns for sharing us their lives especially to the Weick family who

have become our second family in Bayreuth. Finally, I would like to express my gratitude to the Deutscher Akademischer Austausch Dienst (DAAD) for awarding me the scholarship which has allowed me to pursue my doctoral studies in Germany. Above all, praise and honor belong to my Lord and Savior Jesus Christ who has made all these things possible. Glory to Him for being ever faithful and true!

Erklärung

Dieses Dokument wurde vom Autor selbständig und nur mit den angegebenen Quellen und Hilfsmitteln erstellt. Der Autor hat bisher keine Promotionsversuche unternommen.

Bayreuth, 3. Februar 2006

Jonathan S. Guevarra